Design, Processing, and Failure Analysis of Open-Architecture Composite Structures
by

Yang Shen

A dissertation submitted to the Graduate Faculty of
Auburn University
in partial fulfillment of the
requirements for the Degree of
Doctor of Philosophy

Auburn, Alabama
December 12, 2015

Approved by

Sabit Adanur, Chair, Professor of Mechanical Engineering
Royall Broughton, Jr., Professor Emeritus of Polymer and Fiber Engineering
David Beale, Professor of Mechanical Engineering
Winfred Foster, Professor of Aerospace Engineering
David Branscomb, R&D Specialist, Takata Highland Composites

Abstract

The Open-Architecture Composite Structures (O-ACS) are composed of tow-pregs and cord-pregs. This research conducts a full spectrum analysis from tow-preg to cord-preg and O-ACS. The final goal is to propose an integrated design tool which consists of two parts: cord-preg module and O-ACS module. The cord-preg module uses information from tow-pregs and architecture of jacket as input to output the desired geometry, stiffness and strength of cord-preg. The O-ACS module takes output data from the cord-preg module as input to similarly generate the geometry, stiffness and strength of O-ACS. Mechanical properties at cord-preg level are calculated using micromechanical models, whereas the failure analysis of O-ACS is performed using finite element method. Moreover, composite beam design with optimal bending stiffness is studied using this design tool.

Acknowledgement

I would like to thank Dr. Sabit Adanur, my major advisor, who introduced me to this amazing research group and guided me over my Ph.D. study. He is a great professor who encourages me to do anything and gives me freedom to solve problems.

I must thank Dr. Roy Broughton, Dr. David Beale, and Dr. Winfred Foster. They can always propose a decent solution for me every time when I have a problem. They have provided me countless valuable suggestions so that I can rapidly grow and learn. I still remember the moment that I knew nothing about the research when I first joined this research group. It is Dr. Roy Broughton, Dr. David Beale, and Dr. Winfred Foster who corrected my mistakes, trained me about the manufacture, taught me about the knowledge, and guided me to the right direction.

I must thank Dr. David Branscomb for his encouragement and mentoring. He is a smart engineer who has considerable experience and innovative thoughts. He has inspired me and mentored me a lot for which I am very grateful. He also offered me an internship from which I gained valuable working experiences and trainings.

I also want to give my thanks to other students in this research group: Austin Gurley, Nakul Kothari, Sanyam Shirgaonkar, Shiv Mysore, and Uday Sangars. I have not only received great assistance from them, but learned a lot from them.

Finally, I express my gratitude to my wife, Zi Yan, who supports me unconditionally during difficult times and helps me to get through problems. I would never finish my Ph.D. in time without her support and understanding.

Table of Contents

Abstract ii

Acknowledgement iii

Table of Contents iv

List of Tables ix

List of Figures xi

List of Abbreviations xv

Chapter 1 Introduction 1

Chapter 2 Literature Review 3

Mechanics of Composites Material 3

Stiffness of Composites 3

Strength of Composites 8

Mechanics of Grid Structures 14

Chapter 3 Design and Analysis of Hybrid Cord-Preg Yarn for Braided Composite Structures 15

Abstract 15

Introduction 16

Visualization of Cord-preg 17

Kinematic Equations of Braiding 17

Artificial Tension and Relaxing 21

Mechanical Properties of the cord-preg 24

Transversely Isotropy of the Cord-preg 26
Effective Moduli of the Core 26
Validation of Chamis Model 27
Effective Diameter of the Core 28
Flexural Modulus of the Core 31
Strength of the Core 33
Conclusions 45
Chapter 4 Cord-Preg Design with Optimal Bending Stiffness 46
Abstract 46
Introduction 47
Material Preparation 48
Results and Discussions 52
Conclusions 59
Chapter 5 Stiffness Characterization of Open-Architecture Composite Structures 60
Abstract 60
Introduction 61
Mathematical Elaboration 62
Vectorial Transformation 62
Free Body Diagram of Representative Volume of O-ACS 67
Energy Method and Equivalent Stiffness 68
Tension Scenario 70
Torsion Scenario 72
Bending Scenario 73

Results and Discussions 74
Conclusions 83
Chapter 6 Failure Analysis of Micro-joints In Open Braided Composite Structures 84
Abstract 84
Introduction 84
The Finite Element Model of the Joint 85
Geometry 86
Material Properties 86
Element and Mesh 87
Boundary Conditions 88
Cohesive Zone Model 89
Physical Test of the Strength of the Joint 89
Results and Verification 90
Conclusions 93
Chapter 7 Failure Analysis of O-ACS using FEA 94
Abstract 94
Introduction 94
Failure Mode Analysis 96
Joint De-bonding 97
Yarn Failure 98
Buckling 98
Finite Element Model 99
Axial Compression 102

Buckling Failure under Compression 102
Yarn Failure under Compression 105
Joint De-bonding under Compression 108
Overall Failure Mode under Axial Compression 109
Axial Tension 112
Buckling Failure under Axial Tension 112
Yarn Failure under Tension 113
Joint De-bonding under Tension 116
Overall Failure Mode under Axial Tension 116
Pure Bending 117
Buckling Failure under Pure Bending 117
Yarn Failure under Pure Bending 120
Joint De-bonding under Pure Bending 123
Overall Failure Mode under Pure Bending 123
Torsion 124
Buckling Failure under Torsion 124
Yarn Failure under Torsion 127
Joint De-bonding under Torsion 130
Overall Failure Mode under Torsion 131
Validation by Compression Tests of O-ACS 132
Global Buckling of O-ACS 135
Conclusions 139
References 139

Appendices 143

Generation of the geometry of the cord-preg in Vpython 143

Diameter and flexural modulus of the core 160

An example of the shell program in Matlab for generating the finite element code 162

An example of a finite element code in APDL for eigenvalue buckling analysis 168

List of Tables Page

Table 1 Data of tensile modulus 27

Table 2 Diameter of the core 30

Table 3 Data of flexural bending stiffness of 36K core 33

Table 4 Data for constituents in the core 43

Table 5 Maximum tensile force of 36K core with and without jacket 44

Table 6 Bending stiffness data of cord-pregs 53

Table 7 Area moment of inertia comparison between experimental data and parallel axis theorem 55

Table 8 Manufacture parameter data for O-ACS (Gurley, 2014) 75

Table 9 Comparison of the experimental data and analytical solution 76

Table 10 Average deviation between the experimental data and analytical solution 81

Table 11 Contribution of axial and helical yarns on stiffness 81

Table 12 Material properties and geometry of the helical yarn 82

Table 13 Material properties of composite yarn and epoxy resin 87

Table 14 Failure modes for O-ACS 96

Table 15 O-ACS models in FEA 101

Table 16 Material properties of the yarn and joint 102

Table 17 Eigenvalue and nonlinear solution for various braiding angles 103

Table 18 Eigenvalue and nonlinear solution for various mandrel diameters 104

Table 19 Maximum compressive force for the yarn failure criterion for O-ACS with different braiding angles 106

Table 20 Maximum compressive force for the yarn failure criterion for O-ACS with different mandrel diameters 107

Table 21 Maximum compressive force for the joint de-bonding failure criterion for O-ACS with different braiding angles 108

Table 22 Maximum compressive for the joint de-bonding failure criterion for O-ACS with different mandrel diameters 109

Table 23 Summary of failure modes under compression for different braiding angles 110

Table 24 Summary of failure modes under compression for different mandrel diameters 110

Table 25 Deformed shape of O-ACS under tension 113

Table 26 Maximum tensile force for the on yarn failure for different braiding angles 114

Table 27 Maximum tensile force for the on yarn failure for different mandrel diameter 115

Table 28 Summary of failure modes of O-ACS under axial tension 117

Table 29 Critical buckling moment under pure bending for different braiding angles 118

Table 30 Critical buckling moment under pure bending for different mandrel diameter 119

Table 31 Maximum bending moment for the yarn failure for different braiding angles 121

Table 32 Maximum bending moment for the yarn failure for different mandrel diameters 122

Table 33 Summary of failure modes of O-ACS under pure bending 124

Table 34 Critical buckling torque under torsion for different braiding angles 125

Table 35 Critical buckling torque under torsion for different mandrel diameters 126

Table 36 Maximum torque based on the yarn failure for different braiding angles 128

Table 37 Maximum torque based on the yarn failure for different mandrel diameters 129

Table 38 Maximum torque at joint de-bonding 131

Table 39 Summary of failure modes of O-ACS under pure bending 131

Table 40 Experimental data for compression tests 133

List of Figures Page

Figure 1 Representation of track-plate equations on braid geometry (Gurley, 2014) 18

Figure 2 Four different oscillations with the diameter of 0.5, 1, 2, 3 and core diameter of 4.45 . 20

Figure 3 Four braids with different size of axial yarns 21

Figure 4 Illustration of geodesic path by longitudinal tension 22

Figure 5 Iteration of relaxing and tension 23

Figure 6 4x4x4 true triaxial jacket cord-preg with different axial yarn 24

Figure 7 4x4x4 true triaxial jacket cord-preg with fully stretched axial yarn 24

Figure 8 4x4x4 true triaxial jacket cord-preg with fully crimped axial yarn 24

Figure 9 Hexagonal packing of the core 30

Figure 10 Fiber arrangement of inertia of the core based on hexagonal packing 32

Figure 11 Fiber failure mode (Gibson, 2011) 35

Figure 12 Matrix failure mode (Gibson, 2011) 35

Figure 13 Transverse tensile rupture (left) and shear failure mode (right) (Gibson, 2011) 38

Figure 14 Free body diagram of helical yarn under longitudinal compression 39

Figure 15 Failure envelope of the core based on quadratic interaction theory 44

Figure 16 Illustration of cord-preg's side view 49

Figure 17 Labelling system of cord-preg 50

Figure 18 Cord-preg (0) (4x4 330D Nylon) BI 45 (8) 50

Figure 19 Cord-preg (3x1) (2x2 330D Nylon) TT 45 (5) 50

Figure 20 Cord-preg (3x2) (2x2 330D Nylon) TT 45 (2) 51

Figure 21 Cord-preg (4x1) (2x2 330D Nylon) TT 45 (4) 51

Figure 22 Cord-preg (4x2) (2x2 330D Nylon) TT 45 (0) 51

Figure 23 Cord-preg (8x1) (2x2 330D Nylon) TT 45 (0) 52

Figure 24 Simplified label 53

Figure 25 Bending stiffness comparison of the cord-pregs 54

Figure 26 Area moment of inertia vs. number of tow-pregs in each axial 56

Figure 27 Compression test of cord-pregs 57

Figure 28 Compressive force vs. sample length 57

Figure 29 Failure due to the buckling under compression 58

Figure 30 Failure due to the composite broken under compression 58

Figure 31 Compressive strength prediction using quadratic interaction failure criterion with the effect of braider 59

Figure 32 Local coordinate system of helical yarn 62

Figure 33 Zig-zag representation of axial yarn 63

Figure 34 Free body diagram of zigzag axial yarn in O-ACS with 8 braiders 67

Figure 35 Free body diagram of helical yarn 68

Figure 36 Illustration of the section between joints within a helical yarn 74

Figure 37 Axial stiffness (EA) vs. t 83

Figure 38 Torsional stiffness (GJ) vs. t 83

Figure 39 Mode 1, Mode 2, and mixed mode de-bonding modes (Kothari, 2014) 85

Figure 40 Geometry of the joint 86

Figure 41 Axial symmetrical mesh 88

Figure 42 Boundary conditions for radial separation test and tangential slip test 88

Figure 43 Constitutive equation plot for cohesive zone model 89

Figure 44 Joint samples for test 90

Figure 45 Test configuration..... 90

Figure 46 Stress distribution and de-bonding initiation..... 91

Figure 47 Study of element size for radial separation 92

Figure 48 Comparison between FEA and experimental data for radial separation 92

Figure 49 Comparison between FEA and experimental data for tangential slip 92

Figure 50 Equivalent beam for modeling joint..... 98

Figure 51 Standard chart flow for failure analysis of O-ACS 100

Figure 52 Critical buckling load from eigenvalue solution vs. braiding angle..... 104

Figure 53 Critical buckling load vs. mandrel diameter..... 105

Figure 54 Maximum compressive force for the yarn failure criterion vs. braiding angle 107

Figure 55 Maximum compressive force for the yarn failure criterion vs. mandrel diameter..... 108

Figure 56 Illustration of buckling failure over axial yarn..... 111

Figure 57 Illustration of yarn failure over axial yarn..... 111

Figure 58 Illustration of combination of joint de-bonding and buckling failure over axial yarn 112

Figure 59 Maximum tensile force for the on yarn failure vs. braiding angle 115

Figure 60 Maximum tensile force for the on yarn failure vs. mandrel diameter 116

Figure 61 Critical buckling moment vs. braiding angle under pure bending 119

Figure 62 Critical buckling moment vs. mandrel diameter under pure bending 120

Figure 63 Maximum bending moment for the yarn failure vs. braiding angle under pure bending..... 122

Figure 64 Maximum bending moment based on yarn failure vs. mandrel diameter under pure bending..... 123

Figure 65 Different orientations of O-ACS under bending tests 123

Figure 66 Critical buckling torque vs. braiding angle under torsion 126

Figure 67 Critical buckling torque vs. mandrel diameter under torsion 127

Figure 68 Maximum torque based on yarn failure vs. braiding angle under torsion..... 129

Figure 69 Maximum torque based on yarn failure vs. mandrel diameter under torsion..... 130

Figure 70 O-ACS samples for compression tests 133

Figure 71 Comparison between experimental data and model data 134

Figure 72 Compressive force per weight unit length vs. braiding angle 135

Figure 73 Buckling failure triggered by joint de-bonding (left) and yarn failure (right) 135

Figure 74 Critical buckling load vs. total length for O-ACS with various braiding angles 136

Figure 75 Illustration of local buckling and global buckling..... 137

Figure 76 Design chart on critical buckling load of the O-ACS with different braiding angles and diameters 138

List of Abbreviations

E_{11}	Tensile modulus of the composite in the fiber direction (longitudinal direction)
E_{22}	Tensile modulus of the composite in the transverse direction
G_{12}	In plane shear modulus of the composite
G_{23}	Out of plane shear modulus of the composite
v_{12}	Major Poisson's Ratio of the composite
V^f	Volume fraction of the fiber
V^m	Volume fraction of the matrix
${E_{11}}^f$	Tensile modulus of the fiber in fiber direction (longitudinal direction)
${E_{22}}^f$	Tensile modulus of the fiber in transverse direction
${G_{12}}^f$	In plane shear modulus of the fiber
${G_{23}}^f$	Out of pane shear modulus of the fiber
${v_{11}}^f$	Poisson's Ratio of the fiber
E^m	Tensile modulus of the matrix
G^m	Shear of the matrix
v^m	Poisson's Ratio of the matrix
C_{MT}	Stiffness matrices of the composite by Mori-Tanaka theory
C_m	Stiffness matrices of the medium in Mori-Tanaka theory
C_f	Stiffness matrices of the fiber inclusion in Mori-Tanaka theory
E	Eshelby tensor in Mori-Tanaka theory
I	Unit matrix
C_{sc}	Stiffness matrices of the composite by the self-consistent model
${S_{ij}}^f, {S_{ij}}^m$	Components in the compliance matrices of the fiber and matrix

a_{ij}	Components in the bridging matrix
${S_L}^{(-)}$	Compressive strength in longitudinal direction
${S_L}^{(+)}$	Tensile strength in longitudinal direction
${S_T}^{(-)}$	Compressive strength in transverse direction
${S_T}^{(+)}$	Tensile strength in transverse direction
${S_m}^{(-)}$	Compressive strength of the matrix
${S_{LT}}^{m}$	In plane shear strength of the matrix
S_{LT}	In plane shear strength
σ_1	Stress in longitudinal direction
σ_2	Stress in transverse direction
τ_{12}	In plane shear stress
${e_L}^{(-)}$	Max compressive strain in longitudinal direction
${e_L}^{(+)}$	Max tensile strain in longitudinal direction
${e_T}^{(-)}$	Max compressive strain in transverse direction
${e_T}^{(+)}$	Max tensile strain in transverse direction
e_{LT}	Max in plane shear strain
ε_1	Strain in longitudinal direction
ε_2	Strain in transverse direction
γ_{12}	In plane shear strain
σ_i	Stress component indicating the i direction
${e_m}^{(+)}$	Max tensile strain of the matrix
S_{f12}	In plane shear strength of the fiber

S_{m12}	In plane shear strength of the matrix
$\emptyset$	Radius of horn gear
D	Major diameter
n	Number of carriers being used
g	Total number of carrier
f	Number of forks in each horn gear
R_{axial}	An array of axial yarns' radius
X_{new}, Y_{new}	Node coordinate after tension or compression
X_{old}, Y_{old}	Node coordinate before tension or compression
dr	A small increment in radial direction
$X_{axial}(i), Y_{axial}(i)$	Node Coordinate on the axial yarn
$R_{mandrel}$	Radius of the mandrel
X_1, Y_1, Z_1	Node coordinate which is next to the node of interest
X_0, Y_0, Z_0	Node coordinate which is before the node of interest
N_i	Number of fibers at the i-th level
N_t	Total number of fibers in the core
x	Number of layers
d	Diameter of the monofilament
D_{core}	Area of a monofilament
E_f	Equivalent flexural modulus
ρ	Bending curvature
M	Bending moment

E_l Tensile modulus (modulus in longitudinal direction)

ε Strain

z Distance to the neutral plane

L Total thickness of the beam

$I_{i\_fiber\_yy}$ Moment of inertia of the fibers at the i-th layer

I_{mono_yy} Moment of inertia of a monofilament

A_{mono} Area of a monofilament

I_{c_yy} Moment of the core

$I_{t\_matrix\_yy}$ Total moment of inertia of the matrix in the core

E_{flex} Equivalent flexural modulus of the core

$S_{f1}{}^{(+)}$ Tensile strength of the fiber in longitudinal direction

$S_{mf1}{}^{(+)}$ Tensile stress of matrix at the max strain of the fiber in longitudinal direction

P Imaginary pressure applied on a thin-walled tube

Z Length of a thin-walled tube

F_x Force component in hoop direction

N Force component in longitudinal direction

α Braiding angle (the angle between helical yarn and mandrel axis direction)

F_r Force in radial direction

σ_r Stress in radial direction

E_j, A_j Modulus of the jacket, area of the jacket

E_c, A_c Modulus of the core, area of the core

F_{jacket} Longitudinal compression or tension transferred on the jacket

F_{core} Longitudinal compression or tension transferred on the core

F Total longitudinal compression or tension

${\sigma_{core}}^{L}$ Longitudinal stress on the core

${\sigma_{core}}^{T}$ Radial stress applied on the core

$(\overrightarrow{e_x}, \overrightarrow{e_y}, \overrightarrow{e_z})$ Unit vector of the global Cartesian coordinate system

$(\overrightarrow{e_r}, \overrightarrow{e_v}, \overrightarrow{e_{zr}})$ Unit vector of the global cylindrical coordinate system

$(\overrightarrow{e_{x\prime}}, \overrightarrow{e_{y\prime}}, \overrightarrow{e_{z\prime}})$ Local coordinate system of a helical yarn

$(\overrightarrow{e_{x\prime\prime}}, \overrightarrow{e_{y\prime\prime}}, \overrightarrow{e_{z\prime\prime}})$ Local coordinate system of an axial yarn

θ Crimp angle in the axial yarn

L Area of a monofilament

$\hat{F}_{braider}$ Force vector applied on the braider

$\hat{M}_{braider}$ Moment vector applied on the braider

$\hat{F}_{axial}$ Force vector applied on the axial yarn

$\hat{M}_{axial}$ Moment vector applied on the axial yarn

$U_{braider}$ Total strain energy in the braider

U_{axial} Total strain enery in the axial yarn

I_{xx}, I_{yy} Moment of inertia with respect to different plane

J Polar moment of inertia of the cord-preg

E_f Tensile modulus of the cord-preg

G_t Torsional shear modulus of the cord-preg

G_s Short beam shear modulus of the cord-preg

γ Cross-sectional shape coefficient for shear stiffness

$\hat{F}_{B\_tension}$ Force vector applied on the braider due to axial tension

$\hat{F}_{A\_tension}$ Force vector applied on the axial yarn due to axial tension

$\hat{M}_{B\_tension}$ Moment vector applied on the braider due to axial tension

$\hat{M}_{A\_tension}$ Moment vector applied on the axial yarn due to axial tension

$U_{B\_tension}$ Total strain energy of the braider under tension

$U_{A\_tension}$ Total strain energy of the axial yarn under tension

EA_b Equivalent axial stiffness of the braider

EA_a Equivalent axial stiffness of the axial yarn

EA_{total} Total equivalent axial stiffness

$\hat{F}_{B\_torque}$ Force vector applied on the braider due to torque

$\hat{F}_{A\_torque}$ Force vector applied on the axial yarn due to torque

GJ_b Equivalent torsional stiffness of the braider

GJ_a Equivalent torsional stiffness of the axial yarn

GJ_{total} Total equivalent torsional stiffness

$(E_{ef}I)_{axial}$ Equivalent bending stiffness of the axial yarn

$(E_{ef}I)_{helical}$ Equivalent bending stiffness of the braider

h Distance from the mid node on the braider interval to the neutral plane

Chapter 1 Introduction

This research is an extended study of Open-Architecture Composite Structures (O-ACS). The first study of O-ACS originated with Dr. David Branscomb, who proposed the concept of O-ACS for minimum weight composite design. This technology is patented by US 20150056449 A1 (Broughton, Branscomb and Beale, 2015) and US20130302604 A1 (Branscomb, Broughton and Beale, 2013). More details about manufacturing of O-ACS and its significance as an innovative superlight composite structure has been discussed in *Minimal Weight Composites Utilizing Advanced Manufacturing Techniques* (Branscomb, 2012). The previous research focused on:

1. Fabrication of O-ACS using braiding technology
2. Computer aided engineering for guiding design and manufacturing of O-ACS (Branscomb, 2007)
3. Design and manufacture of the pre-impregnated hybrid yarn which is referred to as the cord-preg specifically for making O-ACS
4. Experimental characterization of the cord-preg for measuring its mechanical properties
5. Experimental characterization of the O-ACS for measuring its mechanical properties
6. Experimental characterization of micro-joints on O-ACS
7. The design tool called 'Fellpoint' which not only outputs geometry of O-ACS and loading pattern on the braiding machine, but computes the stiffness of O-ACS and optimal structure given constraints (Gurley, 2015)

A full scope of O-ACS design involves the design of the cord-preg using tow-pregs and design the architecture of O-ACS. The properties of the cord-preg directly determine the properties of O-

ACS since they are the fundamental components forming the O-ACS. Therefore, the hierarchy with three different levels are established to analyze the properties of O-ACS: the tow-pregs which are pre-impregnated fibers, cord-pregs which consist of a braided jacket and the tow-pregs as the core, and the O-ACS.

The aim of this research is to develop a multi-level design tool based on this hierarchy. At the cord-preg level, the size of the cord-preg can be calculated by hexagonal packing model; The stiffness and strength of the cord-preg which is modelled by the transversely isotropic properties will be predicted using micromechanical models which consider the mechanical properties of tow-preg as input. Similarly, at the O-ACS level, the stiffness and strength of O-ACS will be predicted using finite element method which takes output data from cord-preg module as input. A finite element code generator is developed in Matlab® to automatically create APDL code for Ansys. In the failure analysis of O-ACS, the joint de-bonding, the cord-preg yielding, and buckling are considered to be possible failure modes. The buckling analysis is performed in both eigenvalue solution and nonlinear solution. The joint is simulated by the beam element with equivalent properties of the cord-preg in transverse direction. The geometry model of the cord-preg and O-ACS is also proposed based on kinematic equations with a permutation term representing for different axial yarn diameter. This multi-level design tool can potentially cover all major aspects of manufacturing O-ACS and predicting its properties.

Chapter 2 Literature Review

Mechanics of Composites Material

Stiffness of Composites

Since this research utilizes micromechanical models to calculate the properties of the cord-pregs from properties of fiber and matrix, a review of micromechanical models of composites will be introduced in this chapter.

The term 'micromechanics', in material science, usually refers to the mechanical properties at the level of molecular scale or lattice structure. When the term micromechanics is used in the field of fiber reinforced composites, it is considered to be the study of effective composite properties in terms of constitutive materials such as fibers and matrix. The micromechanical models use properties of fiber and matrix to compute the overall properties of the composites which is referred to as macromechanics.

There has been numerous micromechanical models proposed for predicting composite properties. The first one is believed to be well-known 'Rule of Mixture (ROM)' which was proposed by Voigt (Voigt, 1889) and 'Inverse Rule of Mixture (IROM)' which was proposed by Reuss (Reuss, 1929). The ROM model assumes an iso-strain condition, whereas IROM makes an iso-stress assumption. The equations are given as follows:

$$E_{11} = V^f {E_{11}}^f + V^m E^m$$

$$v_{12} = V^f {v_{11}}^f + V^m v^m$$

$$\frac{1}{E_{22}} = \frac{V^f}{{E_{22}}^f} + \frac{V^m}{E^m}$$

$$\frac{1}{G_{12}} = \frac{V^f}{{G_{12}}^f} + \frac{V^m}{G^m}$$

where

E_{11} Tensile modulus of the composite in the fiber direction (longitudinal direction)

E_{22} Tensile modulus of the composite in the transverse direction

G_{12} In plane shear modulus of the composite

G_{23} Out of plane shear modulus of the composite

v_{12} Major Poisson's Ratio of the composite

V^f Volume fraction of the fiber

V^m Volume fraction of the matrix

${E_{11}}^f$ Tensile modulus of the fiber in fiber direction (longitudinal direction)

${E_{22}}^f$ Tensile modulus of the fiber in transverse direction

${G_{12}}^f$ In plane shear modulus of the fiber

${G_{23}}^f$ Out of pane shear modulus of the fiber

${v_{11}}^f$ Poisson's Ratio of the fiber

It has been demonstrated that longitudinal modulus E_{11} and Poisson's ratio v_{12} obtained by ROM model shows good agreement with experimental results, while transverse modulus E_{22} and in plane shear modulus G_{12} do not agree well with experimental data. Later on, some semi-empirical models were established to correct the ROM by introducing some correcting factors. Halpin-Tsai proposed a semi-empirical model which corrects the transverse modulus and in plane shear modulus (Halpin and Kardos, 1976). The equations are given by:

$$E_{22} = E^m(\frac{1 + \delta\mu V^f}{1 - \mu V^f})$$

$$G_{12} = G^m(\frac{1+\delta\mu V^f}{1-\mu V^f})$$

$$\mu = \frac{\frac{M_f}{M_m} - 1}{\frac{M_f}{M_m} + \delta}$$

where $\delta = 1\ and\ 2$, and $M = E\ or\ G$ for E_{22} and G_{12}, respectively.

The Chamis model is considered to be the most reliable model (Ning Hu, 2012). The Chamis model gives the formula for all five independent elastic properties (Chamis, 1989).

$$E_{11} = V^f {E_{11}}^f + V^m E^m$$

$$E_{22} = \frac{E^m}{1-\sqrt{V^f}(1-\frac{E_m}{{E_{22}}^f})}$$

$$v_{12} = V^f {v_{11}}^f + V^m v^m$$

$$G_{12} = \frac{G^m}{1-\sqrt{V^f}(1-\frac{G_m}{{G_{12}}^f})}$$

$$G_{23} = \frac{G^m}{1-\sqrt{V^f}(1-\frac{G_m}{{G_{23}}^f})}$$

Hashin and Rosen made some modifications to longitudinal modulus, longitudinal Poisson's ratio and in plane shear modulus using a composite cylinder assemblage model (CCA) (Hashin and Rosen, 1964):

$$E_{11} = V^f {E_{11}}^f + V^m E^m + \frac{4V^f V^m ({v_{12}}^f - v^m)^2}{\frac{V^f}{K^m} + \frac{1}{G^m} + \frac{V^m}{K^f}}$$

$$v_{12} = V^f {v_{12}}^f + V^m v^m + \frac{V^f V^m ({v_{12}}^f - v^m)(\frac{1}{K^m} - \frac{1}{K^f})}{\frac{V^f}{K^m} + \frac{1}{G^m} + \frac{V^m}{K^f}}$$

$$G_{12} = G^m \frac{G^f(1 + V^f) + G^m V^m}{G^f V^m + G^m(1 + V^f)}$$

where K^f and K^m are determined by:

$$K^f = \frac{E_f}{2(1 - 2{v_{12}}^f)(1 + {v_{12}}^f)}$$

$$K^m = \frac{E_m}{2(1 - 2v^m)(1 + v^m)}$$

The Mori-Tanaka model is a well-known model for modeling various composite materials (Mori and Tanaka, 1973). The model takes into account an inclusion model in which fibers are modelled by the inclusions embedded in a homogeneous medium. Benveniste proposed a new approach for Mori-Tanaka application (Benveniste, 1987):

$$C_{MT} = C_m + \left[V_f * \left(C_f - C_m\right) * A_{Eshelby}\right] * \left[V_m * I + V_f * A_{Eshelby}\right]^{-1}$$

$$A_{Eshelby} = \left[I + E * {C_m}^{-1} * \left(C_f - C_m\right)\right]^{-1}$$

where $C_m \; and \; C_f$ are stiffness matrices of medium and inclusion. $A_{Eshelby}$ is the strain concentration tensor of the dilute solution. E is the Eshelby tensor which depends on the shape of the inclusion and the Poisson's ratio of matrix. This model actually considers the structure of fibers and matrix at the micro level.

Hill proposed the self-consistent model (S-C) which takes two iterations of Mori-Tanaka model by replacing medium stiffness matrices with composite stiffness matrices (Hill, 1965).

At first iteration:

$$A_{Eshelby} = \left[I + E * {C_m}^{-1} * \left(C_f - C_m\right)\right]^{-1}$$

$$C_{sc} = C_m + \left[V_f * \left(C_f - C_m\right) * A_{Eshelby}\right]$$

At second iteration:

$$A_{Eshelby} = \left[I + E * {C_{sc}}^{-1} * \left(C_f - C_{sc}\right)\right]^{-1}$$

$$C_{sc} = C_m + \left[V_f * \left(C_f - C_m\right) * A_{Eshelby}\right]$$

Another popular micromechanical model called 'Bridging model' was proposed by Huang et al. (Huang, Z.M., 2001). The bridging method is able to predict the inelasticity and strength of composites.

$$E_{11} = V^f {E_{11}}^f + V^m E^m$$

$$E_{22} = \frac{(V^f + V^m a_{11})(V^f + V^m a_{22})}{(V^f + V^m a_{11})\left(V^f {S_{11}}^f + V^m a_{22} {S_{22}}^m\right) + V^f V^m ({S_{21}}^m - {S_{21}}^f) a_{12}}$$

$$v_{12} = V^f {v_{11}}^f + V^m v^m$$

$$G_{12} = \frac{(V^f + V^m a_{66}) {G_{12}}^f G_m}{V^f G_m + V^m a_{66} {G_{12}}^f}$$

$$G_{23} = \frac{0.5(V^f + V^m a_{44})}{V^f\left({S_{22}}^f - {S_{23}}^f\right) + V^m a_{44}({S_{22}}^m - {S_{23}}^m)}$$

where a_{ij} is the component of the bridging matrix, ${S_{ij}}^f, {S_{ij}}^m$ are components in compliance matrices of the fiber and matrix, respectively.

Li studied the appropriate boundary, symmetric and periodic conditions required to predict the elastic properties of composites using finite element mode (Li, S., 2008). The arrangement of fibers such as square array, diamond array and hexagonal array can be included in the finite element mode. The employment of finite element model for predicting elastic constants of composite material usually requires more computational time and complexity for better accuracy. However, it has been demonstrated that finite element (FE) modelling does not necessarily produce better results than analytical solutions. Considering the simplicity and accuracy, Chamis model is chosen as the micromechanical model to calculate the five independent elastic constants for the cord-preg.

Strength of Composites

With respect to the failure analysis, the prediction of strength is more difficult to achieve. The failure criteria for highly anisotropic composites are derived from previously developed failure criteria for predicting elastic to plastic transition in isotropic metallic materials. The failure criteria plots a failure envelope. The failure only occurs when the stress component is out of the failure envelope. The coordinate axes for failure envelope are chosen to be along the principal axes of the composite material. The procedure of the failure criteria application requires transformation of state of stresses to the principal axes using transformation matrices.

The Maximum Stress Criterion for orthotropic lamina was first proposed by Jenkins (Jenkins, 1920). Based on the Maximum Stress Criterion, failure occurs when the principle stress exceeds its corresponding strength value. The plot according to the Maximum Stress Criterion is a rectangle. It must be pointed out that the failure envelope is independent of shear stress and does not account for possible interaction between stress components. Its mathematical representation:

$$-S_L{}^{(-)} \leq \sigma_1 \leq S_L{}^{(+)}$$

$$-{S_T}^{(-)} \leq \sigma_2 \leq {S_T}^{(+)}$$

$$|\tau_{12}| \leq S_{LT}$$

${S_L}^{(-)}$ Compressive strength in longitudinal direction

${S_L}^{(+)}$ Tensile strength in longitudinal direction

${S_T}^{(-)}$ Compressive strength in transverse direction

${S_T}^{(+)}$ Tensile strength in transverse direction

S_{LT} In plane shear strength

Waddoups suggested a similar failure criterion which is called Maximum Strain Criterion for orthotropic lamina (Waddoups, 1967). This failure criterion predicts failure when principle strain component exceeds the corresponding ultimate strain. Maximum Strain Criterion does not include possible interaction between stress components either. They can be expressed by the following equations:

$$-{e_L}^{(-)} \leq \varepsilon_1 \leq {e_L}^{(+)}$$

$$-{e_T}^{(-)} \leq \varepsilon_2 \leq {e_T}^{(+)}$$

$$|\gamma_{12}| \leq e_{LT}$$

${e_L}^{(-)}$ Max compressive strain in longitudinal direction

${e_L}^{(+)}$ Max tensile strain in longitudinal direction

${e_T}^{(-)}$ Max compressive strain in transverse direction

${e_T}^{(+)}$ Max tensile strain in transverse direction

e_{LT} Max in plane shear strain

The Maximum Stress Criterion and Maximum Strain Criterion do not yield good agreement with experimental data for biaxial failure test. Thus, a more robust failure criterion with stress component interaction taken into consideration has been developed. The maximum distortional energy criterion or von Mises Criterion is the most widely used quadratic interaction criteria for predicting the onset of yielding in isotropic metals (Higdon et al., 1976). Hill modified the maximum distortional energy criterion so that it can applied to anisotropic materials (Hill, 1948). The failure surface of Hill Criterion is described by:

$$A(\sigma_2-\sigma_3)^2 + B(\sigma_3-\sigma_1)^2 + C(\sigma_1-\sigma_2)^2 + 2D{\tau_{23}}^2 + 2E{\tau_{31}}^2 + 2F{\tau_{12}}^2 = 1$$

where A, B, C, D, E, F are coefficients to be determined from uniaxial and shear strength tests. The failure occurs when the left hand side is greater than 1. Azzi and Tsai extended Hill Criterion for predicting failure of transversely isotropic lamina (Azzi and Tsai, 1965). The Hill Criterion is simplified into:

$$\frac{{\sigma_1}^2}{{S_L}^2} - \frac{\sigma_1\sigma_2}{{S_L}^2} + \frac{{\sigma_2}^2}{{S_T}^2} + \frac{{\tau_{12}}^2}{{S_{LT}}^2} = 1$$

Compressive strength and tensile strength can be applied to strength term individually depending on whether the principle stress is compression or tension.

Tsai and Wu proposed a more general version of a tensor polynomial failure theory for anisotropic materials (Tsai and Wu, 1971). The failure surface of Tsai-Wu's criterion is described by the tensor polynomial:

$$F_i\sigma_i + F_{ij}\sigma_i\sigma_j = 1$$

where $i, j = 1, 2, 3$ represent the principal stresses, $i, j = 4, 5, 6$ represent the shear stresses. The coefficients $F_i \; and \; F_{ij}$ are to be determined by experimentally measuring the strength in each direction.

The failure criterions introduced above are the primary and most widely used criterions upon which further investigations and improvement are conducted. Zinoviev et al., used the Maximum Stress Criterion to predict the failure of a single lamina under the assumption of linear elastic behavior (Zinoviev et al., 1998 and 2002). Bogetti et al., extended the Maximum Strain Criterion to three dimension for studying the failure behavior of lamina (Bogetti et al., 2004). Tsai et al., employed the Tsai–Wu Criterion based on linear elastic assumption (Liu and Tsai, 1998). In addition, a progressive failure analysis feature was also included for failure prediction in lamina. Among all the failure criteria, considering its accuracy and simplicity, Tsai-Wu's quadratic interaction criterion is used in this research to examine the failure in composite yarns.

All the failure criterions introduced above are considered as a macromechanical failure behavior of the lamina without regard to micromechanical behavior of fibers and matrix. The prediction of strength using micromechanical models will be discussed subsequently.

Due to highly anisotropy of composites, similar to elastic constants, the strength of composites must be specified into certain directions: longitudinal tensile strength, longitudinal compressive strength, transverse tensile and compressive strength and in-plane shear strength.

Kelly and Davies proposed a model based on the rule of mixture for predicting longitudinal tensile strength of composites (Kelly and Davies, 1965). The model explains that different fiber and matrix properties result in different failure modes which produce different formula. The failure mode of longitudinal tensile case can be summarized to be matrix failure mode which happens

when the ultimate strain of matrix is smaller than the ultimate strain of fiber. The fiber failure mode happens when ultimate strain of fiber is smaller than the ultimate strain of matrix.

The failure under longitudinal compression, on the other hand, is much different than the failure under longitudinal tension. There are three basic longitudinal compression failure modes: microbuckling of fibers in either shear or extensional mode, transverse tensile rupture due to Poisson's strains, and shear failure of fibers without buckling. Failure models based on local buckling or microbuckling of fibers in the matrix have been developed by Rosen and Schuerch (Rosen, 1965; Schuerch, 1966). There are two types of failure modes in the microbuckling of fibers: the extensional mode and the shear mode. The extensional mode indicates the fibers are buckled in an out-of-plane pattern resulting into matrix compression or extension, whereas the shear mode indicates the fibers are buckled in an in-plane pattern resulting the matrix shearing. The critical buckling load for extensional model and shear model is calculated by energy method assuming a sinusoidal buckling shape. The buckling strength for extensional mode is given by:

$$S_L{}^{(-)} = 2V^f \left[\frac{V^f E_{11}{}^f E^m}{3(1-V^f)}\right]^2$$

The buckling strength for shear mode is given by:

$$S_L{}^{(-)} = \frac{G^m}{1-V^f}$$

It has been demonstrated that the extensional buckling mode is only appropriate for predicting compressive strength of composites with very low fiber volume fraction. While shear buckling mode can be applied to a range of practical volume fraction, it considerably overestimates the strength by comparing with experimental data. Greszczuk has proved that the failure mode will shift from microbuckling to compressive failure of the reinforcement if the shear modulus of

matrix is high enough (Greszczuk, 1974). A model for transverse tensile rupture due to Poisson strains has been developed by Agarwal and Broutman (Agarwal and Broutman, 1990). The model applies Maximum Strain Criterion to transverse direction of the composite under longitudinal compressive loading. According to transverse tensile rupture failure, composite fails because the strain in transverse direction exceeds the ultimate strain of composite. The compressive strength and max strain are given by:

$$S_L{}^{(-)} = \frac{E_{11} e_t{}^{(+)}}{v_{12}}$$

$$e_t{}^{(+)} = \frac{e_m{}^{(+)}}{F}$$

where F is the strain concentration factor which depends on the microstructure of fiber arrangement in matrix (Kies, 1962). Hull calculated the compressive strength based on maximum shear stress, which indicated good agreement with experimental data for graphite/epoxy (Hull, 1981). The compressive strength is derived from the maximum shear strength of the composite:

$$S_L{}^{(-)} = 2(S_{f12} V^f + S_{m12} V^m)$$

The failure in transverse direction can be examined by Maximum Strain Criterion so that the failure is determined by the ultimate strain value in transverse direction. Therefore, it is equivalent to transverse tensile rupture mode:

$$S_T{}^{(+)} = \frac{E_{22} S_m{}^{(+)}}{E^m F}$$

$$S_T{}^{(-)} = \frac{E_{22} S_m{}^{(-)}}{E^m F}$$

In-plane shear strength is given by the same formula as in the transverse failure:

$$S_{LT}{}^{(+)} = \frac{G_{12} {S_{LT}}^{m}}{G^m F}$$

Mechanics of Grid Structures

Considering the geometry of O-ACS, it can be said that O-ACS is analogous to grid structure. Grid structures were first used in the form of metal grid and fabric skin for aircraft construction (Rehfield, 1999). It has been found out that grid stiffened structure is economically good for high stiffness and strength application. With the rapid development of composite technology in past decades, composite grid has been invented and widely used in industry for its excellent stiffness and strength. The mechanical properties of grid structure can be analyzed by a plate or shell with equivalent stiffness. Chen, Tsai and Huybrechts proposed homogenization method or 'smearing out' to find out equivalent stiffness of a grid structure made of composite material (Chen and Tsai, 1996; Huybrechts and Tsai, 1996). However, such analysis assumes a perfect connection at the cross-over point. The mechanics of grid structure based on 'smearing out' method does not take the joint effect into account.

Chapter 3 Design and Analysis of Hybrid Cord-Preg Yarn for Braided Composite Structures

Abstract

The cord-preg yarn, which serves as the fundamental component in forming O-ACS, plays an important role in both manufacture and properties of O-ACS as it directly determines the stiffness, strength as well as the braid-ability of O-ACS. The hybrid cord-preg usually consists of a core and a jacket. The core is responsible for the majority of mechanical properties, whereas the jacket is functioning as a protective layer to hold fibers in the core together and keep them from damaging and buckling out during braiding process. The first part of this chapter introduces the visualization of the cord-preg's architecture. A toolbox which can generate the architecture of the cord-preg has been developed to help us design different cord-pregs. The second part elaborates the micro-mechanic models for predicting stiffness and strength of the cord-preg. Even though a braided jacket is necessary to consolidate fibers as one integrated part, the jacket can compromise the strength of the cord-preg because it provides additional radial force on the core as the cord-preg is being compressed or stretched due its braided helical nature. The failure mode under compression is observed under the light microscope.

Introduction

It has been demonstrated that a braided cord-preg is a well fitted material to braid an open truss composite structure characterized with high stiffness to weight ratio. The cord-preg utilizes the resin impregnated fiber tows which makes it flexible to form a truss structure. In addition, the outer jacket, which is braided outside of the core, has at least two purposes: to protect the core and prevent it from buckling out, and to provide a smooth surface and decrease friction during braiding process. Most fiber reinforced composites such as carbon fiber/resin, fiber glass/resin or basalt fiber/resin can be used as the core to meet specific requirements. However, election of jacket is limited. A braided jacket called true triaxial braid has been proven to be an ideal choice fulfilling these conditions (Branscomb, 2012).

But the design of a jacket can be more than just protective layer. The architecture of the jacket directly determines the shape of the cord-preg. A cord-preg can be designed with various cross-sectional shapes by allocating tow-pregs into axial locations to achieve other purposes. Cross-sectional shape has huge effect on the micro crimp of yarns in the braided composites. The yarn with elliptical cross-sectional shape decreases the crimp as it naturally fits kinematic motion of braiding. Reallocating fibers in the axial location can yield an optimal design with the highest bending stiffness. Therefore, the visualization of the cord-preg is desired for design as well as manufacture. Furthermore, finite element analysis of the cord-preg, if needed, requires the 3D geometry of the cord-preg.

With respect to the mechanical properties of the cord-preg, the measurement of them must be conducted with caution since there is no established standard tests. The preparation of the cord-preg samples for physical tests such as tension or compression tests requires well potted ends to ensure no slippage or damage at the connection between the cord-preg and the fixture. The

prediction of the mechanical properties of the cord-preg remains questionable. The prediction of mechanical properties including stiffness and failure mode is necessary to design tailored and desired properties for O-ACS without costing too much time on physical tests. It turns out that the stiffness and strength of the cord-preg can be solved using micromechanical models.

The aim of this research is to develop a toolbox which can generate appropriate geometry and calculate the stiffness/strength of the cord-preg.

Visualization of Cord-preg

Kinematic Equations of Braiding

In a maypole braiding process, half of carriers are travelling in clockwise direction and the other half are travelling in counterclockwise such that they form interlacing over a mandrel. The motion of the carrier can be modeled by compound function of a sinusoidal function which represents the helix over mandrel and a cosine which accounts for the oscillation over horn gear. The location of the yarn path in the plane which is perpendicular to the mandrel axis is given by (Branscomb, 2007):

$$X = \left[\frac{15}{8}\cos(2\pi t) + \frac{16.5}{2}\right] * \cos(-\frac{\pi t}{4})$$

$$Y = \left[\frac{15}{8}\cos(2\pi t) + \frac{16.5}{2}\right] * \sin(-\frac{\pi t}{4})$$

which can be derived into a more general form (Gurley, 2014):

$$X_{weft} = \left(\emptyset * cos\left(\frac{g}{2}\left(t - \frac{n\pi}{fg}\right)\right) + \frac{D}{2}\right) * \cos(-t - \frac{n\pi}{fg})$$

$$Y_{weft} = \left(\emptyset * cos\left(\frac{g}{2}\left(t - \frac{n\pi}{fg}\right)\right) + \frac{D}{2}\right) * \sin(-t - \frac{n\pi}{fg})$$

$$X_{warp} = \left(-\emptyset * cos\left(\frac{g}{2}\left(t - \frac{n\pi}{fg} + \frac{(2f-1)\pi}{g}\right)\right) + \frac{D}{2}\right) * \cos(t - \frac{n\pi}{fg} + \frac{(2f-1)\pi}{g})$$

$$Y_{warp} = \left(-\emptyset * cos\left(\frac{g}{2}\left(t - \frac{n\pi}{fg} + \frac{(2f-1)\pi}{g}\right)\right) + \frac{D}{2}\right) * \sin(t - \frac{n\pi}{fg} + \frac{(2f-1)\pi}{g})$$

where

$\emptyset$ is the radius of horn gear

D is the major diameter

n is the number of carriers being used

g is the total number of carriers

f is the number of forks in each horn gear

Figure 1 shows the geometrical representation over track-plate according to the above equations.

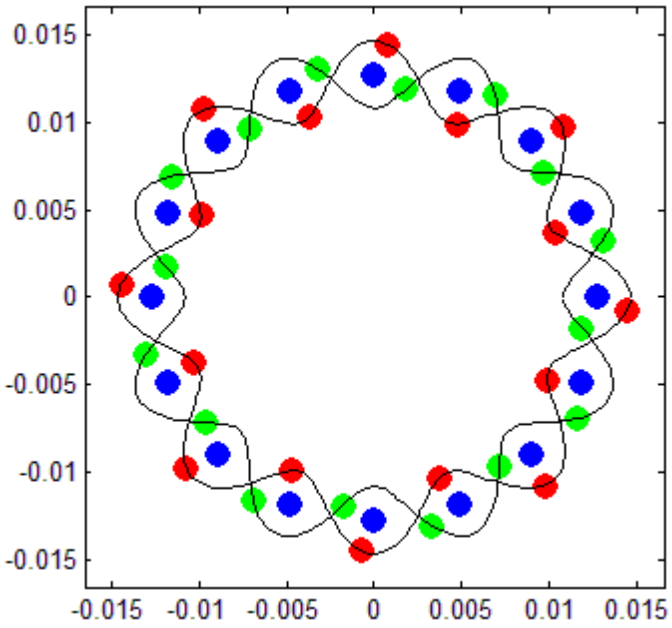

Figure 1 Representation of track-plate equations on braid geometry (Gurley, 2014)

The versatility of the cord-preg in terms of various cross-sectional shape depends on the axial yarn in the jacket. It is the size and location of axial yarn that determines the cross-sectional shape of the cord-preg. Therefore, the size of axial yarn must be taken into account in the kinematic model to produce various cross-sectional shapes. An amplitude term $permutation\ (n, k)$ which stands for the diameter of the axial yarn is introduced in the kinematic equations:

$$X_{weft} = \left(permutation(n,k) * cos\left(\frac{g}{2}\left(t - \frac{n\pi}{fg}\right)\right) + \frac{D}{2}\right) * \cos(-t - \frac{n\pi}{fg})$$

$$Y_{weft} = \left(permutation(n,k) * cos\left(\frac{g}{2}\left(t - \frac{n\pi}{fg}\right)\right) + \frac{D}{2}\right) * \sin(-t - \frac{n\pi}{fg})$$

Permutation (n, k) is a function of axial yarn location indicator (k) and shifted yarn location indicator (n), which outputs the correct oscillation amplitude corresponding to the n and k. An example is given in Figure 2 to indicate the shape. In this particular case, suppose that n=0 indicates the first braider yarn which meets four axial yarns as the order of (0.5, 1, 2, 3). The permutation (0, k) contains an array of 4 elements which are the diameter of the axial yarns: [0.5, 1, 2, 3]. Then the second yarn, which is indicated by n = 1, will be assigned with an array of [1, 2, 3, 0.5] because the second yarn has a phase shifted about the z axis. Therefore the first axial yarn which the second braider yarn meets is the axial yarn with diameter of 1 rather than 0.5. Such concept can be generalized by the following equation:

$$R_{axial} = permutation(n, R_1, R_2, \dots, R_N)[k]$$

where

n: number of permutation needs to be performed

$R_1, R_2, \dots, R_N$: diameter of each axial yarn

k: the k-th element extracted for output

Figure 3 shows geometry of 4 braids with 4 different axial yarns.

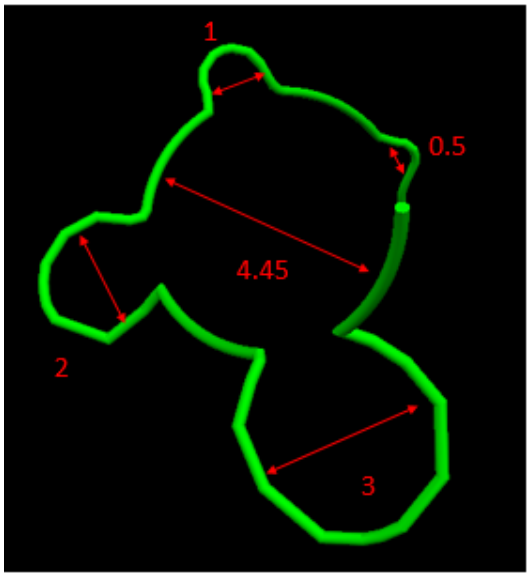

Figure 2 Four different oscillations with the diameter of 0.5, 1, 2, 3 and core diameter of 4.45

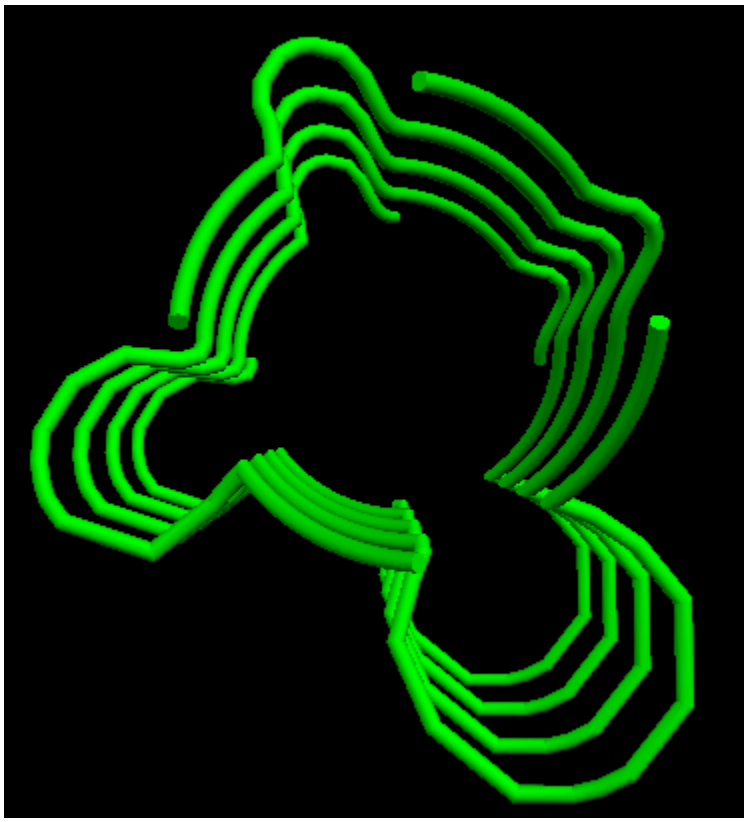

Figure 3 Four braids with different size of axial yarns

Artificial Tension and Relaxing

When the yarns are being braided over a mandrel, there is tension provided to compress the yarn to the mandrel as close as possible and stretch yarn as well. The kinematic equation is based on sinusoidal functions, which does not take tension effect into consideration. Undoubtedly, the formation of braid with tension effect included can be simulated using finite element method. However, a simpler geometrical model is preferred as compared to solving a complicated finite element problem.

The compression of yarns against the mandrel is considered to be consisting of two parts. First, the yarn section between the interlacing joint will be compressed to the circumference of the mandrel. Second, the yarn section at the interlacing joint will be compressed to the contour of each axial yarn.

Given a small increment in radial direction dr, the mathematical relationship between node coordinates before and after compression is:

$$X_{new} = X_{old} * \frac{\sqrt{{X_{old}}^2 + {Y_{old}}^2} - dr}{\sqrt{{X_{old}}^2 + {Y_{old}}^2}}$$

$$Y_{new} = Y_{old} * \frac{\sqrt{{X_{old}}^2 + {Y_{old}}^2} - dr}{\sqrt{{X_{old}}^2 + {Y_{old}}^2}}$$

Two boundary conditions have to be applied to ensure that the yarn will not penetrate the mandrel and axial yarns.

Given $\forall\, i \in [1,2,\dots,N]$, the new node must be chosen such that:

$$\sqrt{\left(X_{new} - X_{axial}(i)\right)^2 + \left(Y_{new} - Y_{axial}(i)\right)^2} \geq R_{axial}(i)$$

$$\sqrt{(X_{new})^2 + (Y_{new})^2} \geq R_{mandrel}$$

The relaxing effect can be also applied using the same algorithm when dr is a negative value, which means the yarn is expanding rather than compressing.

After the structure is compressed, the next step is to stretch the yarn on mandrel axis. Such longitudinal tension effect can be modelled using the concept of geodesics. The yarn path after stretch is a geodesic, or shortest path, from one joint to another joint (Gurley, 2014). This can be implemented using the following equations:

$$X_{new} = \frac{(Z_{old} - Z_0)(X_1 - X_0)}{(Z_1 - Z_0)} + X_0$$

$$Y_{new} = \frac{(Z_{old} - Z_0)(Y_1 - Y_0)}{(Z_1 - Z_0)} + Y_0$$

where $(X_1, Y_1, Z_1)\ and\ (X_0, Y_0, Z_0)$ is the coordinate of the nodes adjacent to node of interest.

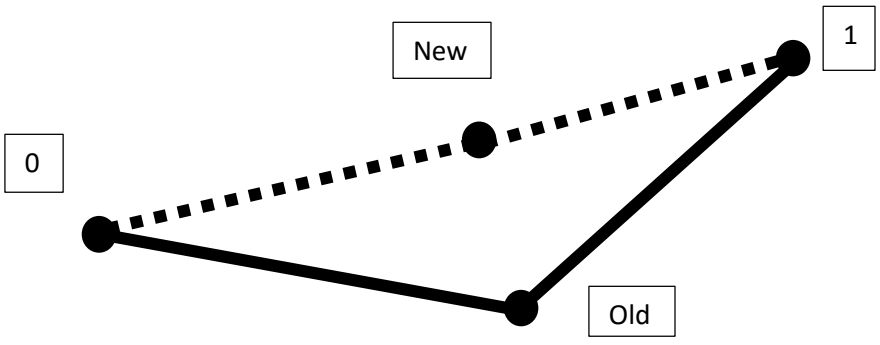

Figure 4 Illustration of geodesic path by longitudinal tension

As illustrated in Figure 4, the point of interest will be moved to the new location such that the new location will be on the line crossing adjacent nodes to achieve the shortest path. Finally, the

compression/relaxing and longitudinal tension will be repeatedly performed to generate the desired geometry as shown in Figure 5.

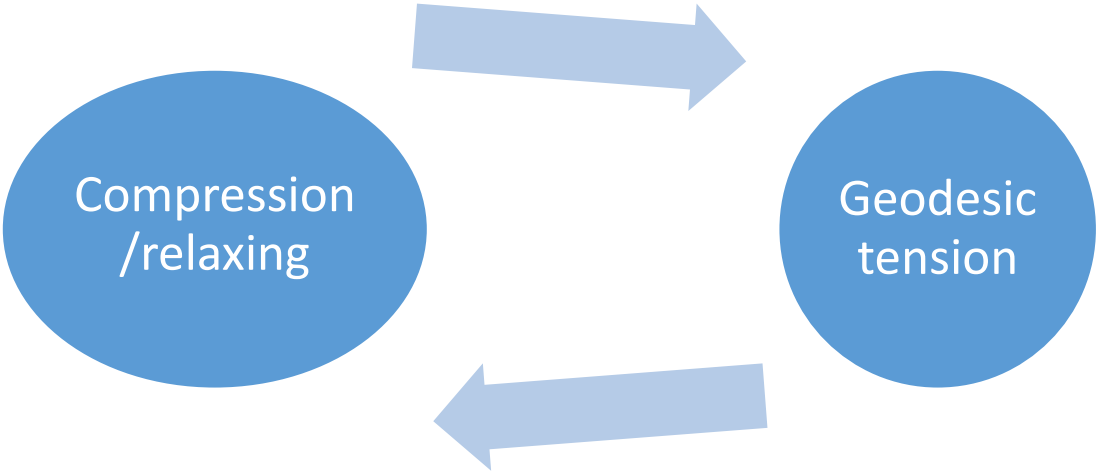

Figure 5 Iteration of relaxing and tension

Examples of visualization of cord-pregs are given in Figures 6, 7, and 8. Figure 6 shows a cord-preg with 4 different axial yarn. Figures 7 and 8 present a fully stretched axial yarn and a fully crimped axial yarn in the jacket, respectively. More analysis using this tool will be given in Chapter 4.

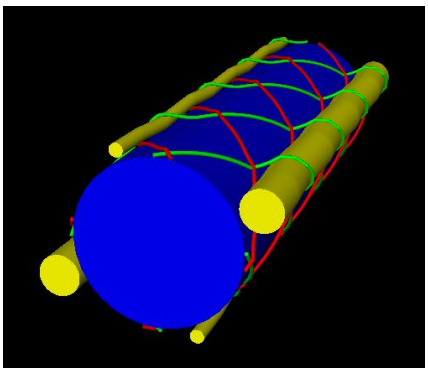

Figure 6 4x4x4 true triaxial jacket cord-preg with different axial yarn

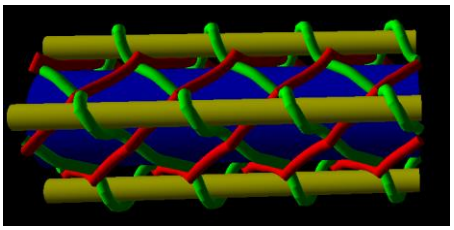

Figure 7 4x4x4 true triaxial jacket cord-preg with fully stretched axial yarn

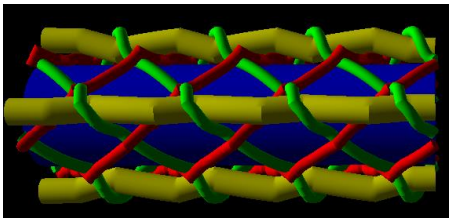

Figure 8 4x4x4 true triaxial jacket cord-preg with fully crimped axial yarn

Mechanical Properties of the cord-preg

The second aim of this research is to predict the mechanical properties of the cord-preg. Since 3D geometry of the cord-preg can be generated, finite element analysis is feasible even though the computational cost might be high. The type of element, mesh technique and material non-linearity in a finite element analysis can cause long computational time. Therefore, an analytical solution for predicting stiffness and strength of the cord-preg is preferred as compared to FEA solution. Due to the composite nature of the cord-preg, micromechanical models, which take the properties of fibers and matrix as input, are reasonable methods to obtain a closed form equation. The mechanical models of unidirectional composites and braided composites have been well established and show good agreement with experimental data. The mechanical properties of constituent components in a composite are the subject of the micromechanics. The mechanical

properties of a composite structure at large scale are the subject of macro-mechanics. The composite, which is a heterogeneous material, is considered to be homogenized volume in which the volume-averaged stress and volume-averaged strain can be studied. The relationship between volume-averaged stress and volume-averaged stain can be further calculated based on the volume fraction and modulus of each component in the composite. The micromechanical model serves as a bridge to connect the properties at fiber/matrix level to properties at macroscale level.

The micromechanics is based on either the mechanics of materials or the elasticity theory. In the mechanics of materials method, the assumption of the iso-strain or iso-stress is made to simplify the problem and derive the stress-strain relationship even though fiber packing geometry is not included. The elasticity theory, on the contrary, takes fiber packing geometry into consideration and actually solves the stress and strain distribution in each component. The elasticity theory involves a numerical solution like in finite element method due to the complex geometries and boundary conditions. Although the assumptions made in the mechanics of material approach are not exactly accurate, some results obtained using this method yield better agreement with experimental data than the results from elasticity theory. A third approach involves empirical solutions in which the equations are developed based on curving-fitting of experimental data. Physical tests have demonstrated that there are pitfalls in such micromechanical models. Experimental characterization is necessary and cannot be substituted by micromechanical models. However, a micromechanical model can become a very powerful tool which allows us to design tailored properties for structure and do the optimization. Moreover, some properties such as transverse modulus of composite are usually deduced from micromechanical models due to their difficult measurements.

Transversely Isotropy of the Cord-preg

If the volume fraction and modulus of the jacket is small enough so that they can be neglected, it is safe to say that the stiffness of the cord-preg is considered to be equivalent to the core. The core, which is essentially a unidirectional composite, is characterized with transversely isotropic properties. The compliance matrix of a transversely isotropic material is given in the following (Gibson, 2011):

$$[S] = \begin{bmatrix} \frac{1}{E_{11}} & -\frac{v_{12}}{E_{11}} & -\frac{v_{12}}{E_{11}} & & & \\ -\frac{v_{12}}{E_{11}} & \frac{1}{E_{22}} & -\frac{v_{23}}{E_{22}} & & 0 & \\ -\frac{v_{12}}{E_{11}} & -\frac{v_{23}}{E_{22}} & \frac{1}{E_{22}} & & & \\ & & & \frac{1}{G_{23}} & 0 & 0 \\ & 0 & & 0 & \frac{1}{G_{12}} & 0 \\ & & & 0 & 0 & \frac{1}{G_{12}} \end{bmatrix}$$

where 1 indicates the fiber direction and 2 is the perpendicular direction to fiber axis.

The transversely isotropic material contains 5 independent elastic constants: E_{11} (longitudinal modulus), E_{22} (transverse modulus), $G_{12}\ and\ G_{23}$ (longitudinal and transverse shear modulus), and v_{12} (major Poisson's ratio).

Effective Moduli of the Core

Based on the literature review of micromechanical models for predicting modulus, Chamis model is selected to calculate the 5 independent elastic constants for transversely isotropic core. The formulas are given as follows:

$$E_{11} = V^f {E_{11}}^f + V^m E^m$$

$$E_{22} = \frac{E^m}{1 - \sqrt{V^f}(1 - \frac{E_m}{{E_{22}}^f})}$$

$$v_{12} = V^f {v_{11}}^f + V^m v^m$$

$$G_{12} = \frac{G^m}{1 - \sqrt{V^f}(1 - \frac{G_m}{{G_{12}}^f})}$$

$$G_{23} = \frac{G^m}{1 - \sqrt{V^f}(1 - \frac{G_m}{{G_{23}}^f})}$$

Validation of Chamis Model

The tensile modulus and shear modulus of a unidirectional core formed by braiding are examined in this section. Three 12K carbon fiber tow-pregs from TCR Composites are used to manufacture the core with a 4x4x4 true triaxial jacket. The jacket is then carefully removed from the core before curing. The comparison of longitudinal modulus between experimental data and Chamis model data is given in Table 1.

Table 1 Data of tensile modulus

Samples	Measured effective tensile modulus (GPa)	Predicted effective tensile modulus (GPa)	Error (%)
1	161.22		
2	166.21		
3	157.23		

4	155.12		
5	160.56		
Average	160.06	165	3.12

Effective Diameter of the Core

The core that is consolidated during the braiding process has a definite diameter and it is necessary to predict its diameter for design purposes. The core of a cord-preg is formed by closely packing tow-pregs with a braided jacket on the circumference. The cross-sectional shape of the core is usually circular due to symmetrical nature of braiding. Therefore, the diameter of the core can be calculated given the number of monofilaments and the diameter of the monofilaments. This computation is critical because not only it can directly evaluate the diameter of the core, but also it can be further used to calculate the bending stiffness of the core.

Assuming each carbon fiber monofilament is packed together in a hexagonal pattern as shown in Figure 9, the monofilaments are gradually stacked layer by layer to form a circular cross-sectional core. The center of the core contains only one monofilament. The second layer is defined as the outer circumference layer, which contains 6 monofilaments. Similarly, the third layer has 12 monofilaments, and so on. The number of monofilaments at the i-th layer can be calculated as follows:

$$N_i = 6(i-1), i \geq 2$$

The total number of monofilaments is simply the sum of each layer:

$$N_t = 1 + \sum_{i=2}^{x} N_i = 1 + 6\sum_{n=1}^{x} n$$

After the mathematical operation, the total number of monofilament has a quadratic relationship in terms of the number of layer:

$$N_t = 1 + 3x(x-1)$$

Therefore, the number of layer x can be solved:

$$x = 0.5 + \frac{\sqrt{9 - 12(1 - N_t)}}{6}$$

The corresponding diameter is then calculated given the diameter of the monofilament d:

$$D_{core} = 2xd - \frac{d}{2}$$

where

N_i: Number of monofilament at i-th layer

N_t: Total number of monofilaments in the core

x: Number of layers in the core

d: Diameter of the monofilament

D_{core}: Diameter of the core

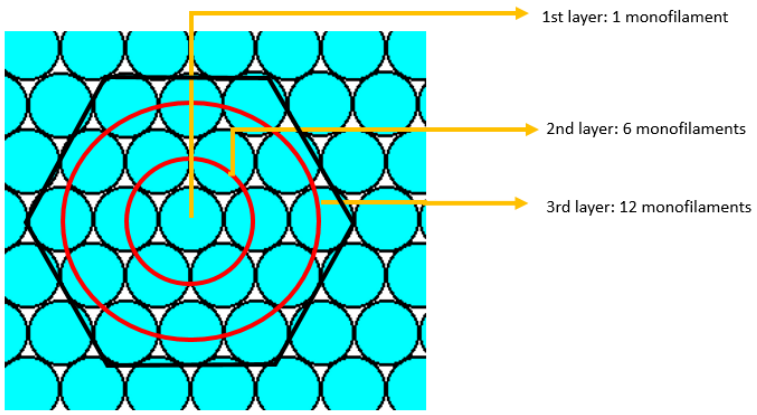

Figure 9 Hexagonal packing of the core

This hexagonal packing model is validated by experiments. The cord-pregs with 48K core, 72K core, 96K core and 192K core are manufactured and measured for effective diameter. As it is indicated in Table 2, the hexagonal packing model can accurately predict the effective diameter of the core.

Table 2 Diameter of the core

	Measured Diameter (mm)	Calculated Diameter (mm)	Deviation (%)
48 K	1.74	1.75	0.57
72 K	2.14	2.16	0.93
96 K	2.48	2.49	0.40
192 K	3.50	3.53	0.85

Flexural Modulus of the Core

The bending stiffness is a crucial property of a composite to evaluate its ability to resist bending moment. The flexural modulus is the same as elastic modulus for an isotropic and homogeneous beam element. However, in a composite beam that consists of fibers and matrix, the flexural modulus is different than the elastic modulus. This can be elaborated by the following equation:

$$M = \frac{E_f I_{yy}}{\rho} = \int_{-\frac{L}{2}}^{\frac{L}{2}} E_l \varepsilon z dA = \int_{-\frac{L}{2}}^{\frac{L}{2}} \frac{E_l z^2}{\rho} dA$$

When a pure bending moment M is applied on a beam element, the bending of the beam is nothing but a combination of tension and compression all over the cross-section (shear ignored). If the tensile modulus E_l is constant throughout the cross-sectional area, then flexural modulus E_f is equal to the tensile modulus. However, this is not the case for a composite yarn where resin, which has low tensile modulus, fills up the space between fibers, which have high tensile moduli.

A method of calculating the flexural modulus of composite core based on hexagonal pattern is proposed. The first layer is the neutral plane crossing the centroid. The rest of layers are chosen such that each monofilament in the same layer has the same distance from the neutral plane as shown in Figure 10.

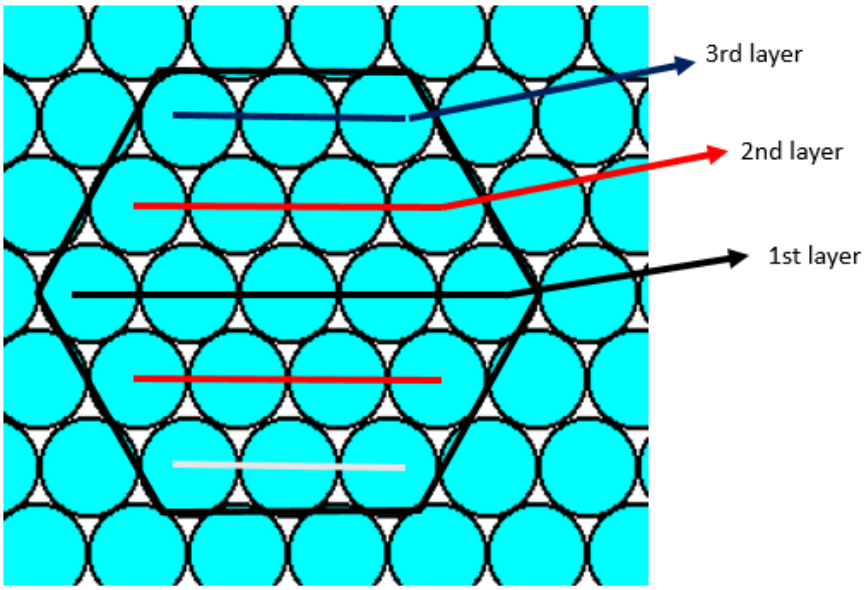

Figure 10 Fiber arrangement of inertia of the core based on hexagonal packing

Based on the parallel axis theorem, the area moment of inertia of the fibers at the i-th layer:

$$I_{i\_fiber\_yy} = (2x - i)(I_{mono\_yy} + \frac{3}{4}A_{mono}(i-1)^2{D_{core}}^2)$$

The total second moment of inertia of fibers is the sum of each layer:

$$I_{t\_fiber\_yy} = (2x-1)I_{mono\_yy} + 2\sum_{i=2}^{x}(2x-i)(I_{mono\_yy} + \frac{3}{4}A_{mono}(i-1)^2{D_{core}}^2)$$

The second moment of inertia of the core based on circular cross-section:

$$I_{c\_yy} = \frac{\pi}{4}(\frac{D_{core}}{2})^4$$

Then the area moment of inertia of matrix is given by:

$$I_{t\_matrix\_yy} = I_{c\_yy} - I_{t\_fiber\_yy}$$

$$E_{flex} = \frac{E_f * I_{t\_fiber\_yy} + E_m * I_{t\_matrix\_yy}}{I_{c\_yy}}$$

where

r: radius of monofilament

i: i-th layer

A_{mono}: cross-sectional area of one monofilament

Second moment of inertia of one monofilament: $I_{mono\_yy} = \frac{\pi}{4} r^4$

Number of monofilaments at the i-th layer: $(2x - i)$

Three point bending tests were conducted to validate the model and Table 3 shows the validation results.

Table 3 Data of flexural bending stiffness of 36K core

	Measured Flexural Modulus (GPa)	Predicted Flexural Modulus (GPa)	Deviation (%)
36 K	130.3	135.3	3.85

Strength of the Core

The basic strategy for strength prediction of the cord-preg is to analyze the jacket and the core separately. The core is considered to contribute the majority of the strength of the cord-preg. The micromechanical models which are used to study the strength of unidirectional composites can be applied to the strength analysis of the core. The jacket can only compromise the strength of the core due to its huge Poisson's ratio. Hence, the strength of the cord-preg is combined with unidirectional core and the negative effect from jacket. Composite materials usually have distinctive tensile and compressive strength. The tensile and compressive strength have to be

studied individually in terms of their failure modes. The transverse strength is excluded in this research because it is not applicable for a braided yarn in structure analysis.

Before proceeding any further, it should be pointed out that strength predictions using the micromechanical models are not expected to be as accurate as those for stiffness. Because the strength is affected more than the stiffness in terms of material and geometrical non-linearity and stress/strain concentration. Therefore, the micromechanical models usually overestimate the strength as it assumes some ideal conditions which could never happen in reality. It would be wiser to correct the models with experimental data by implementing coefficient or a safety factor if the models are to be used for design purposes. Moreover, the deviation of fiber strength alone may be quite significant so that statistical approach is needed for the analysis over large scale, which is beyond the scope of this research.

Longitudinal Tensile Strength

The failure of unidirectional core under tension can be explained by fiber failure mode and matrix failure mode. The fiber failure mode is applied when the maximum failure strain of fiber is less than the failure strain of matrix (Figure 11), whereas the matrix failure mode happens when the failure strain of fiber is greater than the failure strain of the matrix as shown in Figure 12. Since the tow-pregs contain the resin which has greater failure strain than the fiber, fiber failure mode is chosen to predict the tensile strength of the core. The equation for tensile strength is given by (Hull, 1981):

$$S_L{}^{(+)} = S_{f1}{}^{(+)} V^f + S_{mf1}{}^{(+)} (1 - V^f)$$

where

$S_L{}^{(+)}$: longitudinal tensile strength

$S_{f1}{}^{(+)}$: tensile strength of fiber

$S_{mf1}{}^{(+)}$: the matrix stress at the failure strain of fiber

V^f: volume fraction

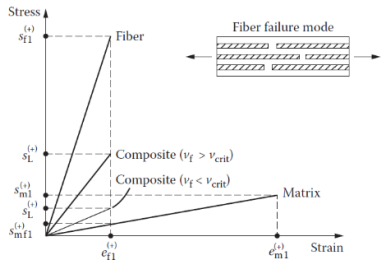

Figure 11 Fiber failure mode (Gibson, 2011)

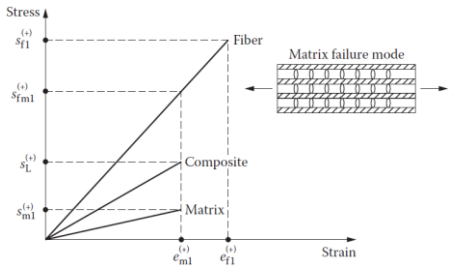

Figure 12 Matrix failure mode (Gibson, 2011)

Longitudinal Compressive Strength

It has been demonstrated that the models for tensile strength cannot be used for compressive strength because the corresponding failure modes are different. Accurate measurement of intrinsic compressive strength turns out to be very difficult. Unidirectional composite material may fail in different ways, each of which results in distinctive strength value. There are three dominating theories to explain the failure mode under compression: microbuckling of fibers, transverse tensile rupture due to Poisson strains, and shear failure of fiber without buckling. According to the

literature review, transverse tensile rupture and shear failure modes are more accurate and will be used in this research to predict the compressive strength of the core.

According to the transverse tensile rupture failure mode, it is the lateral expansion of composite due to Poisson's ratio effect that causes the composite to fail under compression. The illustration of the transverse tensile rupture is given in Figure 13. The mode can also be used for calculating strength in transverse direction. The equation of strength is given by (Agarwal and Broutman, 1990):

$$S_L{}^{(-)} = \frac{E_{11} e_t{}^{(+)}}{v_{12}}$$

where

$S_L{}^{(-)}$: compressive strength

E_{11}: effective longitudinal modulus of composite

$e_t{}^{(+)}$: maximum strain of composite in transverse direction at failure

v_{12}: major Poisson's ratio of the composite

The maximum strain of composite in transverse direction at failure has the following relationship with matrix tensile failure strain $e_m{}^{(+)}$:

$$e_t{}^{(+)} = \frac{e_m{}^{(+)}}{F}$$

Where F can be interpreted as the concentration factor (Kies, 1962).

$$F = \frac{1}{\frac{d}{s}\left(\frac{E^m}{E_{22}{}^f}\right) + 1}$$

where

$e_m{}^{(+)}$: matrix tensile failure strain

d: fiber diameter

s: spacing between fibers

E_m: matrix modulus

E_{f2}: transverse modulus of fiber

The shear failure mode without buckling is depicted in Figure 13. The shear failure mode states that composites fail because the maximum shear stress at 45 degree with respect to the axis exceeds the shear strength of the composite. The equation is given by (Hull, 1981):

$$S_L{}^{(-)} = 2(S_{f12}V^f + S_{m12}V^m)$$

where

S_{f12}: shear strength of fiber

S_{m12}: shear strength of matrix

V^f, V^m: volume fraction of fiber and matrix, respectively

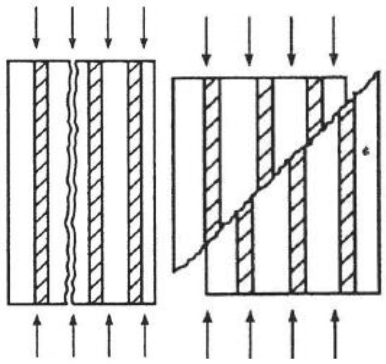

Figure 13 Transverse tensile rupture (left) and shear failure mode (right) (Gibson, 2011)

Effect of Jacket on Strength Property

The strength of the cord-preg can be considered as equivalent to the strength of the core if the modulus and volume fraction of the jacket are insignificant as compared to the core. However, it has been observed that the jacket has negative effect on the strength as it introduces a radial force on the core under longitudinal tension or compression. This phenomenon can be explained by the high Poisson's ratio effect of the helical structure. A helical structure when being stretched tends to reorient more to the force direction rather than its intrinsic deformation, which in turn results in large strain in the lateral direction. If the degree of freedom on helical structure is locked in radial direction, there must be reaction force in radial direction to constraint the structure from moving in lateral direction. Therefore, such additional radial force applied on the core will definitely compromise the strength. The constraint radial force to keep the helical yarn stationary can be calculated. First, the helical yarn will be imagined as an equivalent thin-walled tube. When the longitudinal tension or compression is applied, the resultant radial force is evenly distributed over the equivalent thin-walled tube. The free body diagram is given in Figure 14.

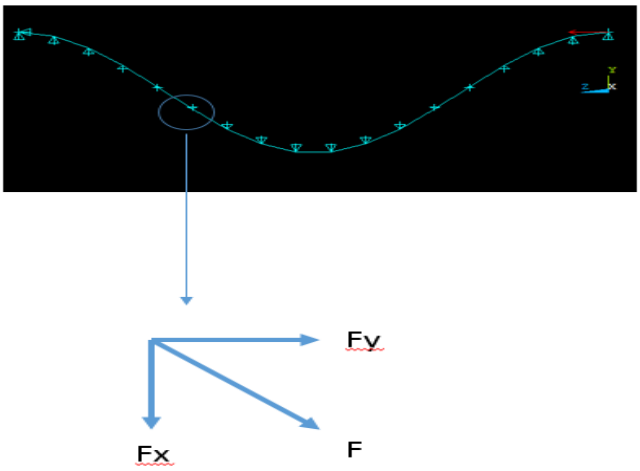

Figure 14 Free body diagram of helical yarn under longitudinal compression

The radial pressure is related to the force in hoop direction:

$$PDZ = 2F_x$$

The force equilibrium:

$$F_x = F\sin\alpha$$

$$F = \frac{N}{cos\alpha}$$

Then the radial pressure is expressed as a function of longitudinal force N, braiding angle θ, and core diameter D.

$$P = \frac{2Ntan\alpha}{DZ} = \frac{2Ntan^2\alpha}{\pi D^2}$$

For a helical yarn, the kinematic equations are:

$$X = Rcos(t)$$

$$Y = Rsin(t)$$

$$Z = \left(\frac{L}{2\pi}\right) t = \frac{R}{tan(\alpha)} t$$

The radial force can be written in form of t:

$$F_r = N * tan(\alpha) * t$$

Since the helical yarn does not really cover all the circumference of the core, the resultant radial stress can be calculated.

$$\sigma_r = \frac{F_r}{d * (\frac{\pi t}{\sin(\alpha)})} = \frac{N * tan(\alpha) * \sin(\alpha)}{\pi d}$$

where

P: imaginary internal pressure applied on the equivalent thin-walled tube

D: core diameter

F: force along helix

Fx: x component of F

F_r: Raidal force

N: compressive force applied on helix

α: braiding angle (the angle between helix and mandrel)

d: the thickness of the braider

The condition of strength analysis of the core changes from unidirectional to multi-axis due to the constraint radial force being applied on the core. The multiaxial strength criterion fits such condition. There are various improvements and modifications to the quadratic interaction criterion. Tsai–Wu's quadratic interaction criterion is used in this research (Tsai and Wu, 1971).

In a 2-dimensional analysis, the stress envelop is defined by:

$$F_{11}{\sigma_1}^2 + F_{22}{\sigma_2}^2 + F_{66}{\sigma_6}^2 + F_1\sigma_1 + F_2\sigma_2 + 2F_{12}\sigma_1\sigma_2 = 1$$

$F_{ij}\ and\ F_i$ are strength tensors that will be experimentally determined. $\sigma_1\ and\ \sigma_2$ are principle stresses. σ_6 is the shear stress. When the left hand side is greater than 1, the material fails. This failure criterion takes into consideration the different tensile and compressive strength as well as interaction between each stress.

$$F_{11} = \frac{1}{{S_L}^{(+)}{S_L}^{(-)}}$$

$$F_1 = \frac{1}{{S_L}^{(+)}} - \frac{1}{{S_L}^{(-)}}$$

$$F_{22} = \frac{1}{{S_T}^{(+)}{S_T}^{(-)}}$$

$$F_2 = \frac{1}{{S_T}^{(+)}} - \frac{1}{{S_T}^{(-)}}$$

$$F_{66} = \frac{1}{{S_{LT}}^2}$$

Tsai and Hahn have proposed the equation:

$$F_{12} = -\frac{\sqrt{(F_{11}F_{22})}}{2}$$

where

$S_L^{(+)}$: longitudinal tensile strength

$S_L^{(-)}$: longitudinal compressive strength

$S_T^{(+)}$: transverse tensile strength

$S_T^{(-)}$: transverse compressive strength

Suppose that the total longitudinal force on the cord-preg is F; the force applied on the jacket and the core can be determined by the rule of mixture:

$$F_{jacket} = (\frac{E_j A_j}{E_j A_j + E_c A_c})F$$

$$F_{core} = (\frac{E_c A_c}{E_j A_j + E_c A_c})F$$

The corresponding longitudinal stress on the core:

$$\sigma_{core}{}^{L} = \frac{F_{jacket}}{A_{core}}$$

The radial stress applied on the core:

$$\sigma_{core}{}^{T} = N_{braider} \frac{2F_{jacket} tan^2\theta}{\pi D^2}$$

where E_j, E_c are the equivalent longitudinal modulus of the jacket and core, and A_j, A_c are the cross-sectional area of the jacket and core, respectively. $N_{braider}$ is the number of spools in the jacket. Therefore, the longitudinal stress of the core can be plotted as a function of radial stress,

which can be examined to have failure or not by the quadratic interaction criterion envelope. 36K carbon fiber core is manufactured and physically tested for tensile and compressive strength. The failure criterion is established by the micromechanical models introduced before.

Table 4 Data for constituents in the core

	Elastic modulus (GPa)	Poisson's Ratio	Tensile Strength (MPa)	Maximum strain at failure (%)
HexTow® AS4D fiber	245	0.2	4750	1.8
UF3330 resin	2.3	0.35	60	3.4

The material properties of fiber and matrix from manufacturer are given in Table 4. Figure 15 depicts the failure envelope based on the quadratic interaction criterion and state of stress of the core. The intersection between stress curve and edge of envelope is considered as the failure initiation. The longitudinal force at the intersection point is obtained as the maximum tensile force. Table 5 gives the data of 36K core and 36 core with biaxial jacket and comparison with the experimental data. The model for predicting pure tensile strength overestimates the maximum tensile force, whereas the model with jacket effect taken into account underestimates the maximum tensile force. Therefore, this model exaggerates the effect of jacket on the core.

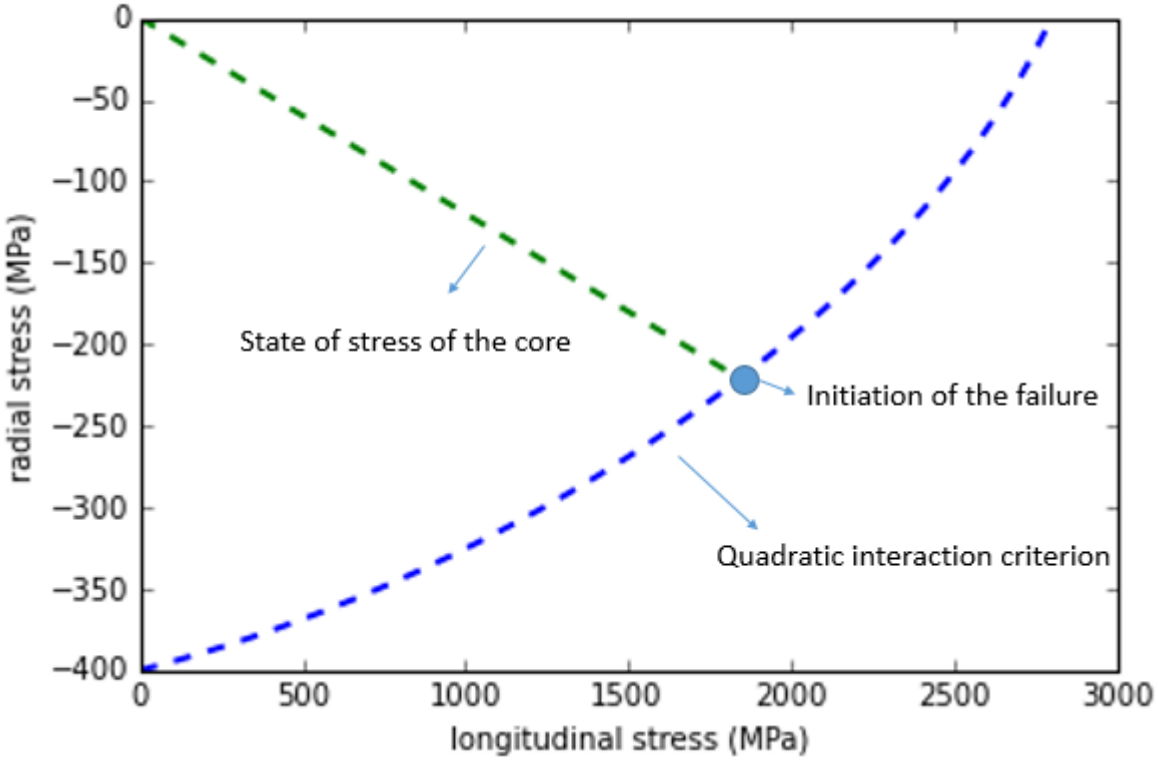

Figure 15 Failure envelope of the core based on quadratic interaction theory

Table 5 Maximum tensile force of 36K core with and without jacket

	Max tensile load from experimental tests (KN)	Max tensile load from the model (KN)
36K core	3.91	4.35
36K core with biaxial jacket	3.61	3.30

Conclusions

This chapter introduced a mathematical model which can generate the geometry of the cord-preg with various cross-sectional shape. The review of micromechanical models for predicting the stiffness and strength were also conducted. A toolbox which takes the axial and braider yarn information as input has been proposed to conveniently improve the design efficiency. The geometric model also includes the feature of various axial yarns. The effective diameter and bending stiffness of the core are calculated by hexagonal packing model. It is concluded that the Chamis model is a reliable micromechanical model for predicting elastic constants of the core. Fiber failure mode is used to predict the tensile strength of the core. Transverse tensile rupture mode and shear failure mode are used for compressive strength calculation. The analysis of jacket shows that it compromises the strength of the core. The model based on mechanics and quadratic interaction failure mode is derived to predict the maximum tensile force with the jacket. It exaggerates the negative effect of jacket on the core. The radial force from jacket is proportional to the number of the helical yarns and equivalent longitudinal stiffness of the helical yarns. A true triaxial jacket with less helical yarns can definitely decrease the negative effect on strength compared to a biaxial jacket.

Chapter 4 Cord-Preg Design with Optimal Bending Stiffness

Abstract

In this research, the possibilities of making a composite yarn with different cross sectional shapes are investigated which can provide different bending stiffness and fit into various applications. It was mathematically proven that the bar with triangular cross-sectional shape gives the highest area moment of inertia among all the other equilateral side shapes given the same area. In this chapter, an innovative method to braid the composite yarn with distinctive cross-sectional shapes is proposed. The composite yarn consisting of a core and jacket is characterized with tailored properties and fast manufacture and has been shown to be an ideal material to fabricate super lightweight open truss structures. The cross-sectional shape can be altered by manipulating the architecture of the jacket and core. Composite yarns with different cross-sectional shapes, which includes triangular, square, hollowed square and circular, were designed and studied for their compression and bending properties. It was shown that the cord-preg with triangular cross-sectional shape has the highest area moment of inertia, whereas the circular cross-section gives the lowest as it is expected. However, the triangular shape with the highest bending stiffness does not necessarily yield the highest compressive strength. It was found that the circular cross-sectional shape, which has no axial carbon fibers in the jacket, has the highest compressive strength. It is demonstrated that the bending stiffness with triangular cross-sectional shape is 60% higher than that with a circular cross-sectional shape.

Introduction

In the field of structural design, the beam structures turn out to be the most favorite choice because they can be easily assembled to form any shape in the most efficient fashion. The cross-sectional shape of the beam element is critical in the design as various cross-sectional shapes provide distinctive mechanical properties. The election of the optimal cross-sectional shape becomes a tricky issue due to not only the difficulty of the manufacture but also because of a time-consuming mathematic solution. Once the optimum shape of the beam is proven, the real application of it can significantly improve the efficiency and effectiveness. Numerous investigations have been devoted to solve the optimization problem in terms of the cross-sectional shape. It was mathematically shown that the bar with circular cross-section has the maximum torsional rigidity as compared to other convex shapes with the same area (Polya and Szego, 1962). Keller unveiled the problem of finding out the strongest cylindrical column, which means the column having the largest critical buckling load (Keller, 1960). It was shown that the shape of the strongest column is not circular but instead an equilateral triangle because the equilateral triangle has the highest area moment of inertia if it is compared to other convex shapes with equilateral sides. On the contrary, the strength of a column has the opposite fashion compared to the stiffness: circular shape provides the lowest torsional strength and equilateral triangle provides the lowest flexural strength. Therefore, there is compromise in terms of the stiffness and strength.

A composite beam is much different than a structural beam made of metal or polymer. The manufacture of a composite beam is more complicated as it requires more attention to the orientation of fibers. The material non-linearity and anisotropic characterization definitely increases the difficulty in understanding its mechanical behavior. The braiding technique is a competitive method for manufacturing composite beam structures in terms of rapid, large scale

manufacture, and low cost. Thousands of fibers can be deposited into desired shape simultaneously. Therefore, using braiding technology to fabricate a composite beam which has optimal bending stiffness is of interest in this research. More details can be found in the patent “Robust pre-impregnated yarn for manufacturing textile composites” US20130302604 A1. The aim of this chapter is to study the possibility of manufacturing composite yarns with various cross-sectional shapes using braiding and propose an architecture with the optimal bending stiffness.

Material Preparation

As it is introduced in the previous chapter, the cross-sectional shape is actually controlled by the architecture of braider and axial yarns in the jacket. The size of axial yarn and its allocation determines the contour. Six cord-preg designs are given in this analysis. Each one of them has different cross-sectional shape. In order to effectively compare the properties, the number of carbon fibers used to braid the yarn must be the same so that they have the same linear density. Carbon fiber tow-pregs provided by the TCR Composites are used to braid the composite yarn. The total number of tow-pregs is eight, each of which has 12K carbon fibers. The design problem becomes how to distribute eight tow-pregs into axial location to achieve the optimal properties. The side view of a cord-preg is given in Figure 16. The green and red indicate the location for the braiders. The center blue indicates the core and the rest shows the position for axial yarns. This example has six axial yarns resulting in the shape of a hexagon. A labeling system is given in Figure 17 to identify different designs of cord-pregs. The first parenthesis contains the number of axial yarns and the number of tow-pregs in each axial yarn. The second parenthesis has the information for the braider. The configuration of jacket are categorized into biaxial (BI), conventional triaxial (CT) and true triaxial (TT). The braiding angle means the angle between helical yarn and the longitudinal direction. The last parenthesis shows the number of tow-pregs

used in the core. If the cross-sectional shape of the cord-preg is unsymmetrical, instability will occur in the plane with the minimum area moment of inertia. In order to avoid this complicity, the cord-preg design in this paper is always considered to have a symmetrical shape.

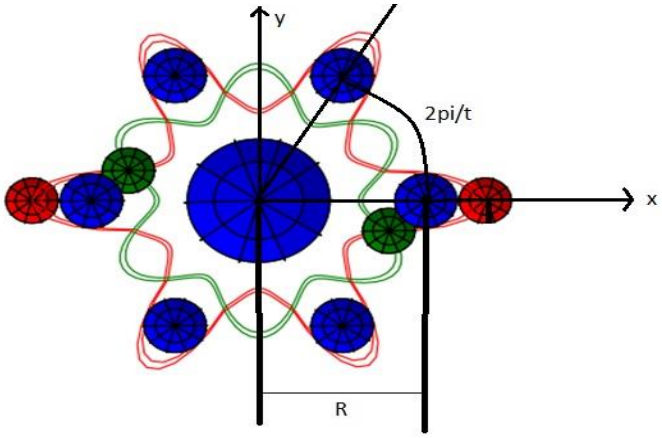

Figure 16 Illustration of cord-preg's side view

There are two conditions prescribed before analysis:

1 The cross-sectional shape of cord-preg must be symmetrical about the longitudinal axis, which means that the tow-pregs must be evenly distributed over axial locations.

2 The braiders must be insignificant and contribute little to the bending stiffness.

Six different cord-preg designs are given in Figures 18 to 23. The toolbox of cord-preg design is used to generate the geometry. The photo of actual shape of each cord-preg is taken under microscope for comparison. All the cord-pregs have eight tow-pregs to ensure the same linear density. As shown in the photos, circular, triangular, square and hollowed shape are developed. The next step is to test and compare their bending stiffness as well as compressive strength.

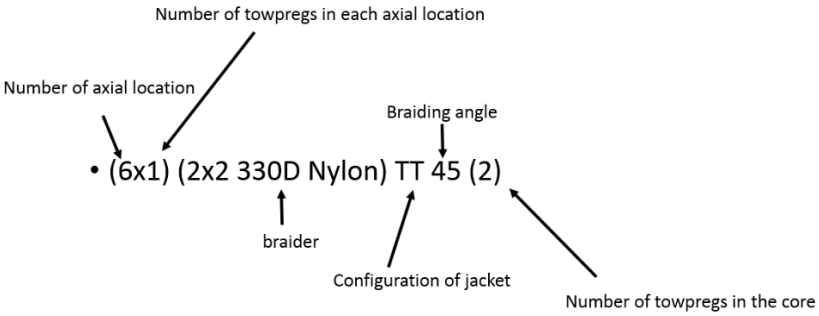

Figure 17 Labelling system of cord-preg

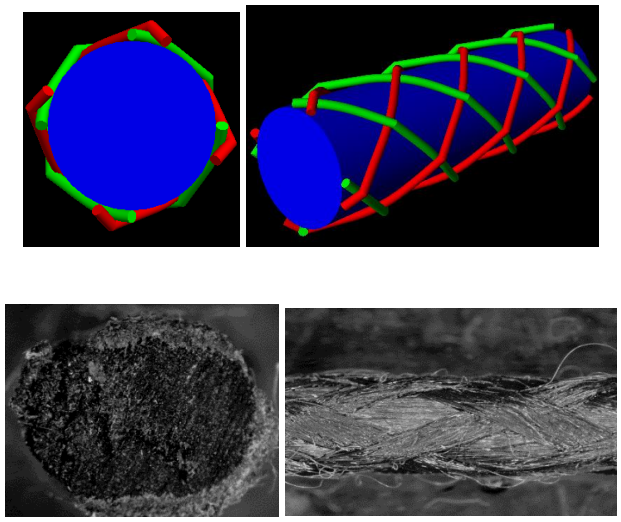

Figure 18 Cord-preg (0) (4x4 330D Nylon) BI 45 (8)

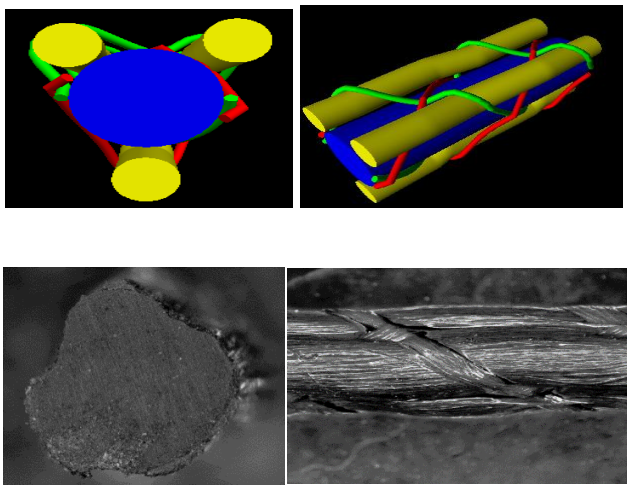

Figure 19 Cord-preg (3x1) (2x2 330D Nylon) TT 45 (5)

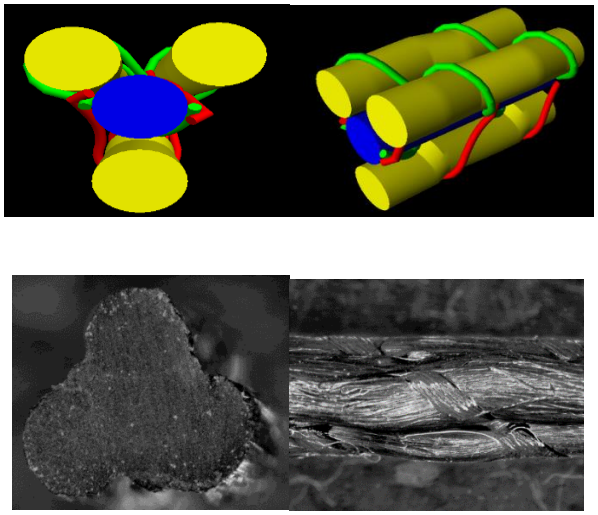

Figure 20 Cord-preg (3x2) (2x2 330D Nylon) TT 45 (2)

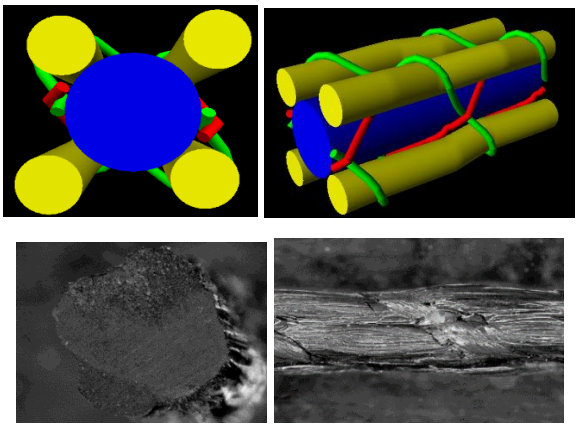

Figure 21 Cord-preg (4x1) (2x2 330D Nylon) TT 45 (4)

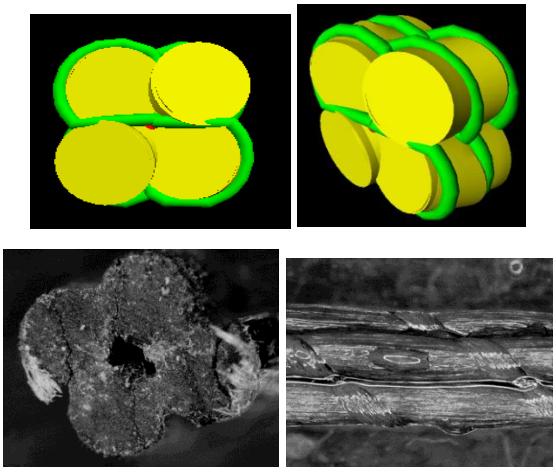

Figure 22 Cord-preg (4x2) (2x2 330D Nylon) TT 45 (0)

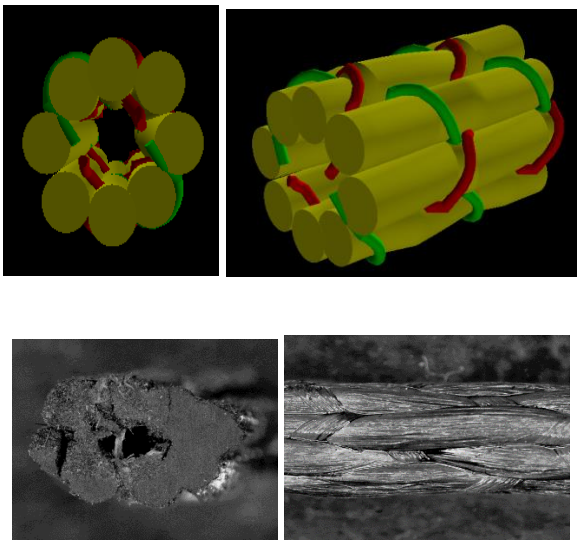

Figure 23 Cord-preg (8x1) (2x2 330D Nylon) TT 45 (0)

Results and Discussions

Three point bending test is used to measure the bending rigidity of the cord-preg. Five samples are tested for each cord-preg. The span length is 100 mm which is big enough to neglect shear deformation. Since there are two distinctive failure modes for composites under compression, namely buckling and intrinsic compressive failure, different span lengths of 14 mm, 17 mm, 25 mm, 36 mm, and 50 mm are used for compression test to recognize the critical buckling load under different span length and the compressive strength. Each cord-preg has three samples for test.

Table 6 gives the data of bending stiffness of each cord-preg. A simplified label is elaborated in Figure 24. It can be concluded that the cord-preg with triangle shape has the highest bending stiffness. The bending stiffness with architecture of 2x3x2 is improved by 60% compared to the circular shape. Since they all have the same linear density, the specific bending stiffness will also be increased by 60%. Besides, the bending stiffness of architecture 0x8x1 is the lowest because this cord-preg is flattened during the cure. Figure 25 shows a direct comparison between each cord-

preg. The toolbox can directly generate the visualization of how fiber tows are distributed over the cross-section.

Table 6 Bending stiffness data of cord-pregs

Cord-pregs	Specimen1	Specimen2	Specimen3	Specimen4	Specimen5	Average bending stiffness (N*m^2)	Percentage of improvement
8x0	0.131	0.123	0.113	0.121	0.143	0.124	Baseline
0x8x1	0.121	0.124	0.0912	0.111	0.127	0.114	NA
0x4x2	0.139	0.193	0.166	0.167	0.144	0.162	30.6%
4x4x1	0.158	0.172	0.161	0.177	0.155	0.164	32.3%
5x3x1	0.181	0.22	0.152	0.201	0.198	0.190	53.2%
2x3x2	0.218	0.187	0.174	0.214	0.212	0.201	62.1%

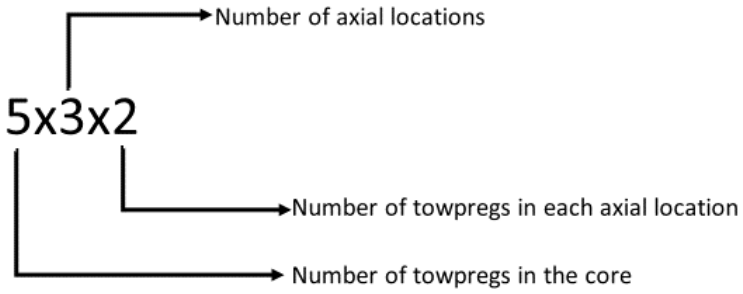

Figure 24 Simplified label

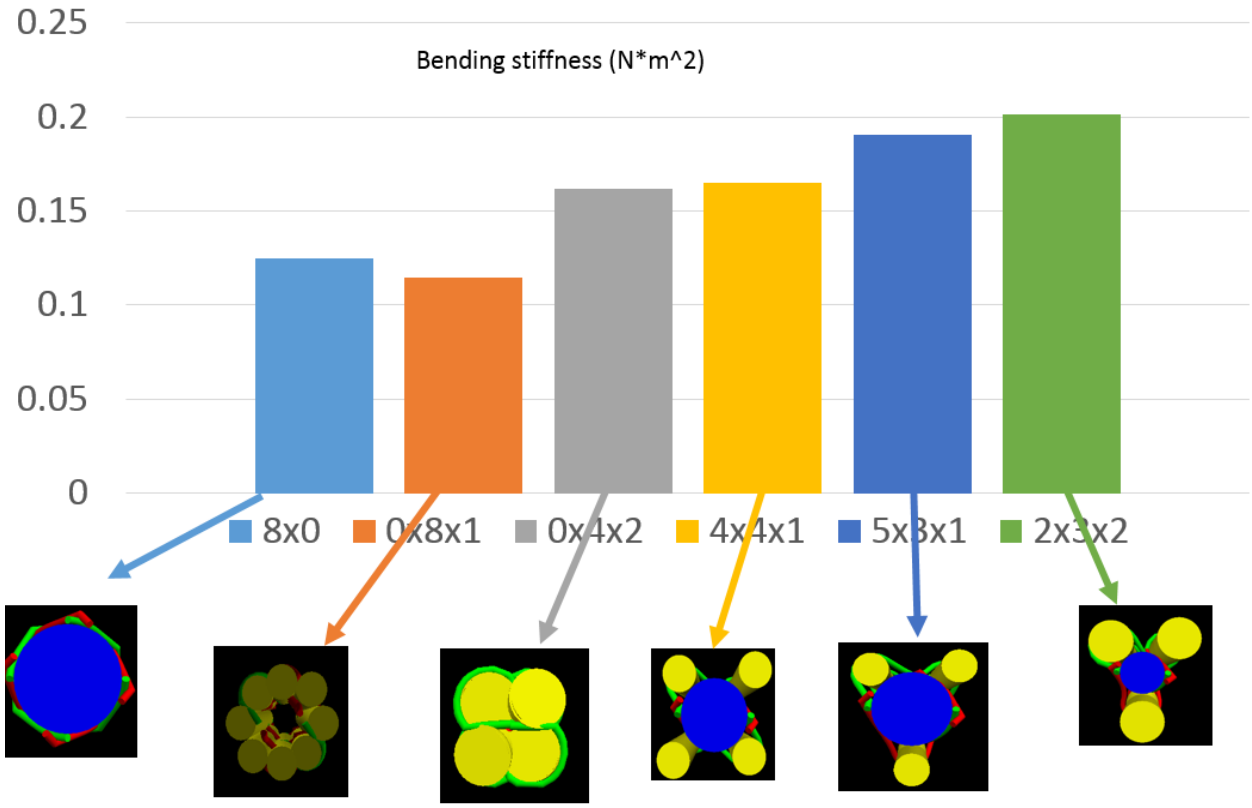

Figure 25 Bending stiffness comparison of the cord-pregs

Moreover, the corresponding area moment of inertia can be calculated using the parallel axis theorem. The data from parallel axis theorem and experiments are compared in Table 7. The parallel axis theorem shows the same tendency as the experimental data even though there are some big deviations. This deviation might come from circular cross-sectional shape assumption upon which the bending stiffness is calculated. Because the bending stiffness from three point bending test is calculated based on the equation which is used for circular beam, the experimental data might not be the accurate numerical value of the bending stiffness. However, by comparison, they indicate accurate ability to resist bending. Figure 26 exhibits the plot of area moment of inertia as a function of the number of tow-pregs in each axial location. The plot is based on the

condition of 8 tow-pregs. Eight 12K tow-pregs will be allocated for the core and axials. Four different curves stand for 3, 4, 6, and 8 axial locations, respectively. In each condition, the moment of inertia is expressed as a function of the number of tow-pregs used in each axial location. The plot covers all the combinations of axials and core with eight 12K tow-pregs. It is indicated that three or four axial yarns in the system can provide relatively higher bending stiffness. Therefore, the basic strategy to specific bending stiffness of a carbon fibers composite beam is to relocate carbon fibers into the locations which grant the structure more area moment of inertia. This principle can be applied to the design of O-ACS as well.

Table 7 Area moment of inertia comparison between experimental data and parallel axis theorem

Cord-preg	Area moment of inertia from experimental data	Area moment of inertia from parallel axis theorem	Deviation (%)
8x0	0.95	1.12	15
0x8x1	0.87	0.44	-97
0x4x2	1.24	0.93	-33
4x4x1	1.26	1.58	20
5x3x1	1.46	1.59	8
2x3x2	1.54	1.91	19

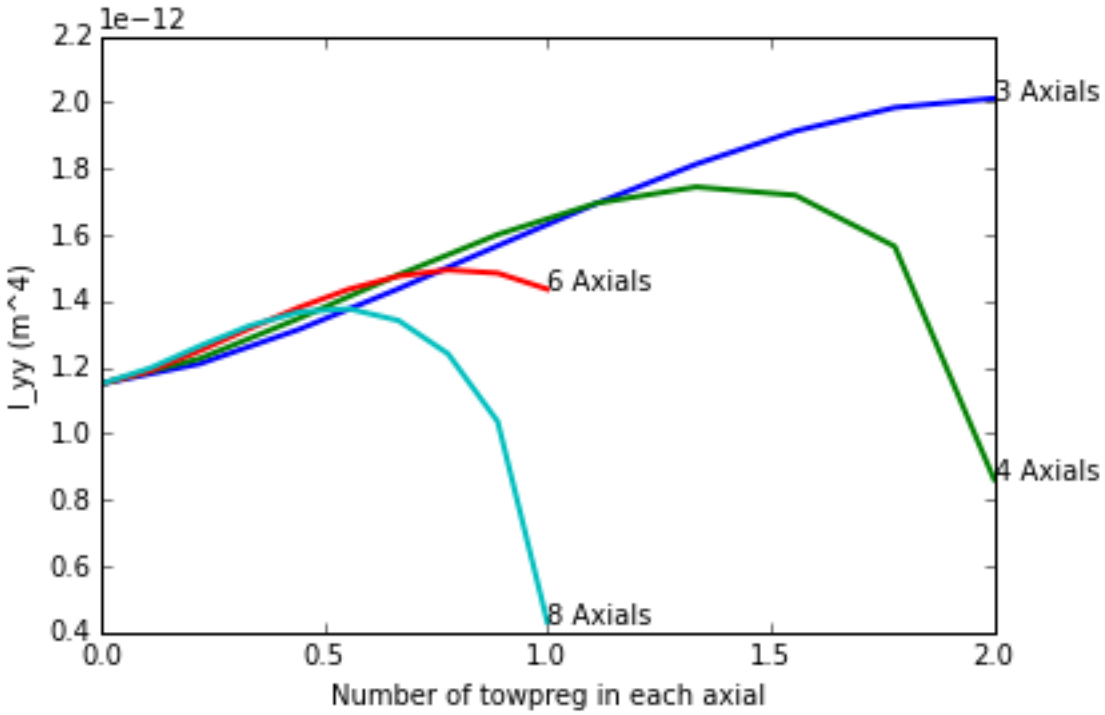

Figure 26 Area moment of inertia vs. number of tow-pregs in each axial

The samples for compression test are prepared with epoxy potted in acorn nuts as shown in Figure 27. The data of maximum compressive load is given in Figure 28. The cord-pregs with no axial pre-preg yarns in the jacket actually have the highest compressive strength. It is reasonable to say that carbon fibers which are held together as one part is stronger than separated parts. The braider which travels between the core and axial yarns will compromise the strength due to the stress/strain concentration. The cord-preg design with the highest bending stiffness does not necessarily yield the highest compressive strength. However, when the length exceeds a critical value at which the compressive failure causes the loss of stability rather than yarn crushing, the yarn with higher bending stiffness still has advantage because the critical buckling is proportional to the bending stiffness. Figure 29 depicts the buckling failure mode when span length of the sample is larger than the critical length. Figure 30 shows the failure mode as shear failure at 45 degree braiding angle.

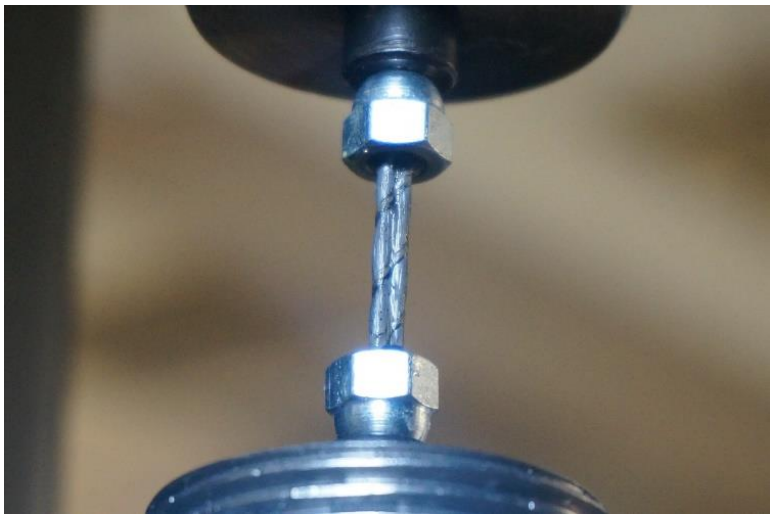

Figure 27 Compression test of cord-pregs

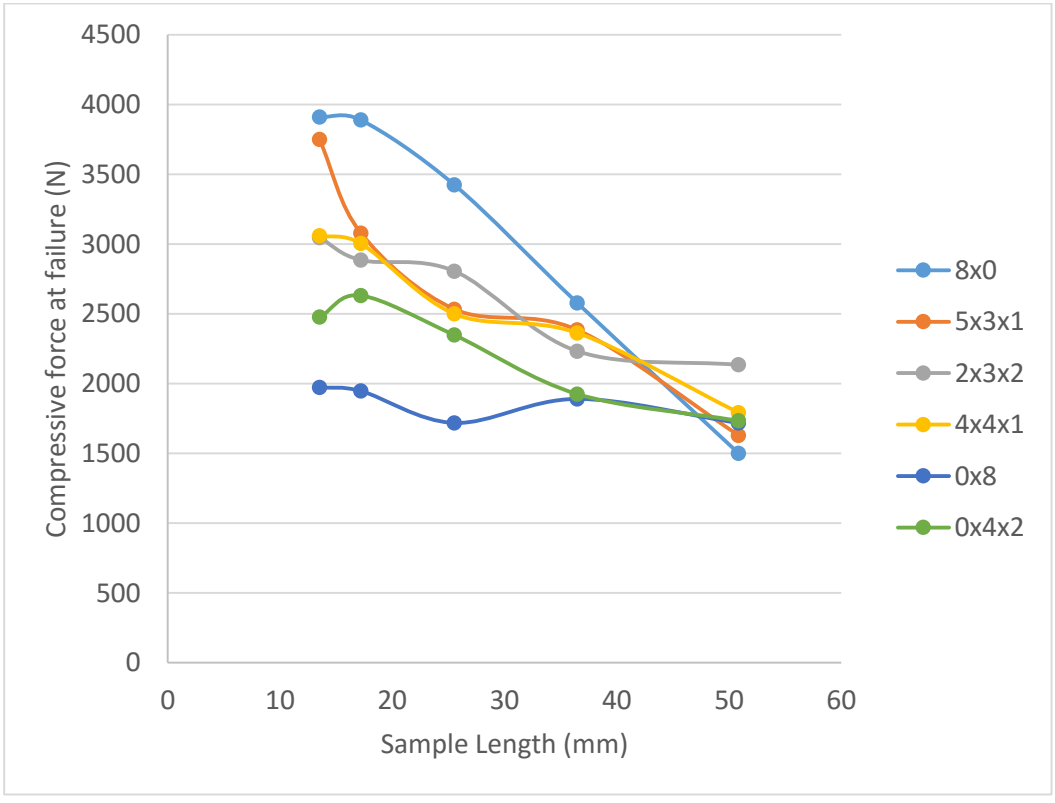

Figure 28 Compressive force vs. sample length

Figure 29 Failure due to the buckling under compression

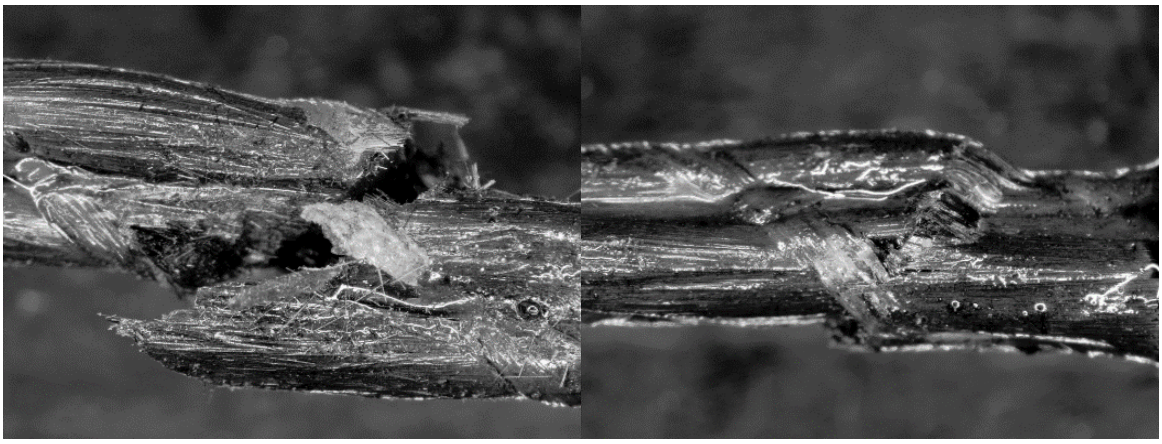

Figure 30 Failure due to the composite broken under compression

By using the quadratic interaction model with braider's effect, the compressive strength of 8x0 sample predicted (Figure 31) is about 4200 N, which compares favorably with the experimental data of 3900 N.

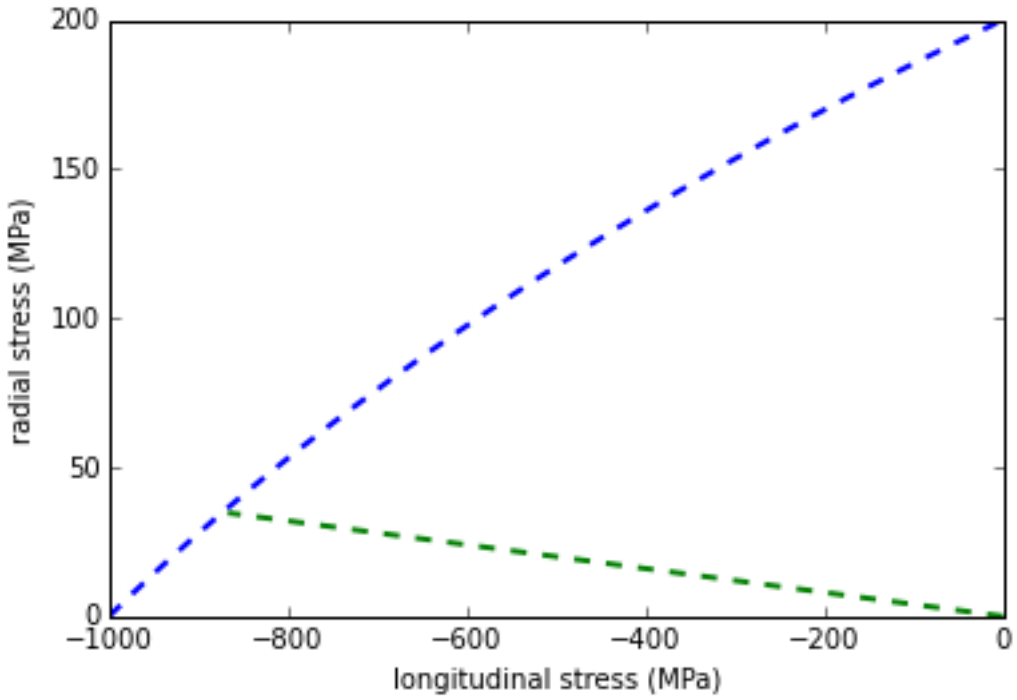

Figure 31 Compressive strength prediction using quadratic interaction failure criterion with the effect of braider

Conclusions

It has been shown that braiding technique is capable of distributing tow-pregs into various axial locations to achieve different cross-sectional shapes. The cord-preg design with three axial locations, which produces the shape close to triangle, and is found to have the highest bending stiffness given the same linear density. However, such a design does not necessarily guarantee the highest compressive strength. The mechanical model proposed based on the transverse tensile rapture and quadratic interaction failure criterion predicts a reasonable strength value considering the effect of braider.

Chapter 5 Stiffness Characterization of Open-Architecture Composite Structures

Abstract

The Open-Architecture Composite Structures (O-ACS) which are braided with hybrid composite yarns have been recently proposed for rapid, open-truss structure manufacturing. The high stiffness to weight ratio makes the O-ACS very promising in various applications. This chapter introduces an analytical solution based on strain energy and homogenization of the repeating unit for solving stiffness properties of the O-ACS. The model computes the stiffness of each axial yarn and helical yarn individually. It also takes the joint effect into consideration. The axial stiffness, bending stiffness and torsional stiffness are obtained using this method and indicate good agreement as compared to the experimental data. The constraints at each joint are considered and show that the number of joints can significantly change the stiffness. The design with respect to the stiffness of the O-ACS can be solved using analytical techniques.

Introduction

It has been realized for a long time that lightweight structures are essential to new structure renovation. If optimization analysis is conducted on a cantilever beam, the consequent shape will be a lattice structure where the materials are only added to the required locations and connected in such a way that they can transfer the load in the most efficient fashion. Numerous investigations have been done to successfully solve the optimization problem for a lattice structure (Rozvany, 2009). Besides, the methodology of optimization is well established. However, the real application of an optimized lattice remains questionable due partially to their high manufacture cost. The Open-Architecture Composite Structures are promising in terms of their rapid and low cost manufacturing. The Open-Architecture Composite Structures (O-ACS) are novel for minimum weight composites. More details can be found in the dissertation *Minimal Weight Composites Utilizing Advanced Manufacturing Techniques* (Branscomb, 2012).

The next step is to predict the stiffness of the O-ACS and understand their mechanical behavior as a function of manufacture variables such as braiding angle, mandrel diameter and number of yarns. Austin Gurley (2014) predicted the stiffness of O-ACS based on finite element method using Timoshenko beam element and the optimal configuration of O-ACS. Besides the finite element method, mechanics of materials approach such as classic laminate theory is also a popular solution for solving equivalent stiffness of a composite. The classic laminate theory has been improved many times by Smith, Pister and Dong, Reissner and Stavsky. The basic strategy of classic laminate theory is to smear out the stiffness over the volume (homogenization) based on elasticity theory. Such homogenization considers the repeating unit in the truss structure to be an equivalent plate or shell element. Although the classic laminate theory applies well to the continuous composite structures, there are certain drawbacks because the repeating unit of a truss structure

behaves very differently compared to the homogenized shell in terms of bending or torsion. Due to the lattice characterization, the beam element is a natural fit for the mechanical analysis. The energy method (Castigliano's theory) can be used to calculate the strain energy over a beam element considering the reaction force or displacement.

The aim of this chapter is to compute the stiffness of O-ACS using energy method and determine how the architecture can affect the stiffness.

Mathematical Elaboration

Vectorial Transformation

Based on the observation of O-ACS, the yarn path can be described as the helical motion for braider yarn and zigzag motion for axial yarn. The local coordinate in which the z' axis is the tangent direction of the helical path is given in Figure 32. The local crimp in axial yarn can be simulated using the zigzag model. The crimp angle shown in Figure 33 is defined as the angle between axial yarn direction and longitudinal direction.

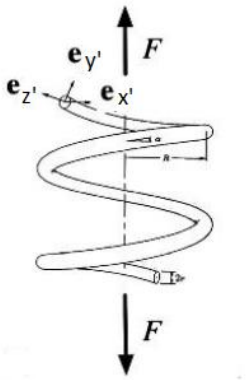

Figure 32 Local coordinate system of helical yarn

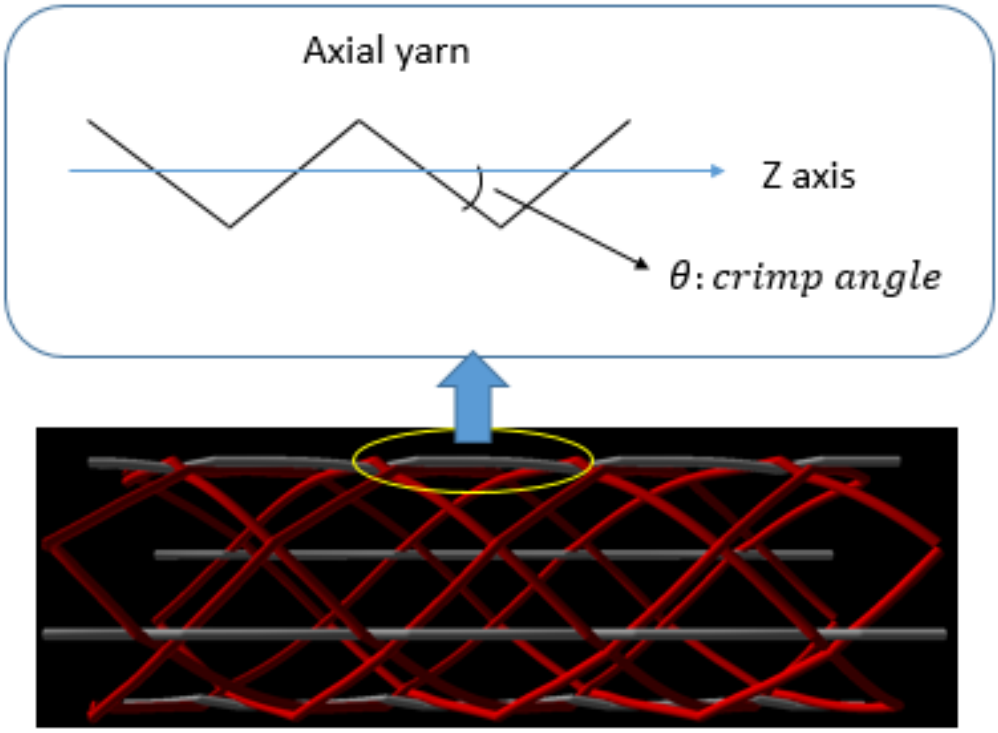

Figure 33 Zig-zag representation of axial yarn

Therefore, in addition to the global coordinate system two local coordinate systems for helical yarns and axial yarns are established such that z axis is along the tangent direction of the yarn path.

Global orthogonal coordinate system:

$$(\overrightarrow{e_x}, \overrightarrow{e_y}, \overrightarrow{e_z})$$

Global cylindrical coordinate system:

$$(\overrightarrow{e_r}, \overrightarrow{e_v}, \overrightarrow{e_{zr}})$$

Local coordinate system of helical yarn:

$$(\overrightarrow{e_{x\prime}}, \overrightarrow{e_{y\prime}}, \overrightarrow{e_{z\prime}})$$

Local coordinate system of axial yarn:

$$\left(\overrightarrow{e_{x''}}, \overrightarrow{e_{y''}}, \overrightarrow{e_{z''}}\right)$$

The function to describe the zigzag path of the axial yarn can be written in the global coordinate system:

$$X = \left(R - L * tan(\theta)\right) * \cos(\frac{2\pi}{N} i)$$

$$Y = \left(R - L * tan(\theta)\right) * \sin(\frac{2\pi}{N} i)$$

$$Z = L = \frac{Rt}{\tan(\alpha)}$$

The unit vector in z'' axis in the local coordinate system of the axial yarn can be calculated as follows:

$$\overrightarrow{e_{z''}} = -sin(\theta)\, cos\left(\frac{2\pi}{N} i\right)\overrightarrow{e_x} - sin(\theta)\, sin\left(\frac{2\pi}{N} i\right)\overrightarrow{e_y} + cos(\theta)\overrightarrow{e_z}$$

Choose a unit vector v perpendicular to the global axis z.

$$v = \left(cos\left(\frac{2\pi}{N} i\right), sin\left(\frac{2\pi}{N} i\right), 0\right)$$

The unit vector in x'' axis:

$$\overrightarrow{e_{x''}} = \frac{\overrightarrow{e_{z''}} \times v}{\cos(\theta)} = -\sin\left(\frac{2\pi}{N} i\right)\overrightarrow{e_x} + \cos(\frac{2\pi}{N} i)\overrightarrow{e_y}$$

The unit vector in y'' axis

$$\overrightarrow{e_{y''}} = \overrightarrow{e_{z''}} \times \overrightarrow{e_{x''}} = -cos\left(\frac{2\pi}{N} i\right) cos(\theta)\, \overrightarrow{e_x} - sin\left(\frac{2\pi}{N} i\right) cos(\theta)\, \overrightarrow{e_y} - sin(\theta)\overrightarrow{e_z}$$

Therefore, the vectorial transformation between local coordinate of axial yarn and global coordinate is written in the tensor form.

$$\begin{Bmatrix} \overrightarrow{e_{x''}} \\ \overrightarrow{e_{y''}} \\ \overrightarrow{e_{z''}} \end{Bmatrix} = [A] \begin{Bmatrix} \overrightarrow{e_x} \\ \overrightarrow{e_y} \\ \overrightarrow{e_z} \end{Bmatrix}$$

$$\begin{Bmatrix} \overrightarrow{e_x} \\ \overrightarrow{e_y} \\ \overrightarrow{e_z} \end{Bmatrix} = [A]^{-1} \begin{Bmatrix} \overrightarrow{e_{x''}} \\ \overrightarrow{e_{y''}} \\ \overrightarrow{e_{z''}} \end{Bmatrix}$$

Where $[A]$ is transformation matrix:

$$[A] = \begin{bmatrix} -sin(\frac{2\pi}{N}i) & cos(\frac{2\pi}{N}i) & 0 \\ -cos(\frac{2\pi}{N}i)cos(\theta) & -sin(\frac{2\pi}{N}i)cos(\theta) & -sin(\theta) \\ -sin(\theta)\,cos(\frac{2\pi}{N}i) & -sin(\theta)\,sin(\frac{2\pi}{N}i) & cos(\theta) \end{bmatrix}$$

The helical function for the braider yarn:

$$X = Rcos(t)$$

$$Y = Rsin(t)$$

$$Z = \left(\frac{L}{2\pi}\right)t = \frac{R}{tan(\alpha)}t$$

The unit vectors representing the local coordinate system of helical yarn are given as follows:

$$\overrightarrow{e_{z'}} = -sin(\alpha)\,sin(t)\,\overrightarrow{e_x} + sin(\alpha)\,cos(t)\,\overrightarrow{e_y} + cos(\alpha)\overrightarrow{e_z}$$

$$\overrightarrow{e_{x'}} = \overrightarrow{e_z} \times \overrightarrow{e_{z'}} = -cos(t)\,\overrightarrow{e_x} - sin(t)\overrightarrow{e_y}$$

$$\overrightarrow{e_{y'}} = \overrightarrow{e_{x'}} \times \overrightarrow{e_{z'}} = cos(\alpha)\, sin(t)\, \overrightarrow{e_x} - cos(\alpha)\, cos(t)\, \overrightarrow{e_y} + sin(\alpha)\overrightarrow{e_z}$$

Tensor form:

$$\begin{Bmatrix} \overrightarrow{e_x} \\ \overrightarrow{e_y} \\ \overrightarrow{e_z} \end{Bmatrix} = [T] \begin{Bmatrix} \overrightarrow{e_{x'}} \\ \overrightarrow{e_{y'}} \\ \overrightarrow{e_{z'}} \end{Bmatrix}$$

$$\begin{Bmatrix} \overrightarrow{e_{x'}} \\ \overrightarrow{e_{y'}} \\ \overrightarrow{e_{z'}} \end{Bmatrix} = [T]^{-1} \begin{Bmatrix} \overrightarrow{e_x} \\ \overrightarrow{e_y} \\ \overrightarrow{e_z} \end{Bmatrix}$$

where transformation matrix $[T] = \begin{bmatrix} -cos(t) & sin(t)cos(\alpha) & -sin(t)sin(\alpha) \\ -sin(t) & -cos(t)cos(\alpha) & cos(t)sin(a) \\ 0 & sin(\alpha) & cos(\alpha) \end{bmatrix}$

Besides, a cylindrical coordinate system is also used since there are force in radial tangential direction.

$$\begin{Bmatrix} \overrightarrow{e_r} \\ \overrightarrow{e_v} \\ \overrightarrow{e_{zr}} \end{Bmatrix} = \begin{bmatrix} cos(t) & sin(t) & 0 \\ -sin(t) & cos(t) & 0 \\ 0 & 0 & 1 \end{bmatrix} \begin{Bmatrix} \overrightarrow{e_x} \\ \overrightarrow{e_y} \\ \overrightarrow{e_z} \end{Bmatrix}$$

R: radius of mandrel diameter

θ: crimp angle of axial yarn

N: number of axial yarn location

i: axial yarn location indicator

α: braiding angle of helical yarn

After the relationships between the local coordinate system and global coordinate system are derived, the boundary conditions, which are the exterior force and reaction force applied on the structure, can be transformed from the global coordinate system to local coordinate system.

Free Body Diagram of Representative Volume of O-ACS

The representative volume is considered to be the repeating unit where the helical yarn completes a full cycle. For example, the free body diagram of the axial yarn in 4x4x4 true triaxial O-ACS for tension is depicted in Figure 34. The left side end is fixed while tensile force is applied on the node at the other end. All the black dots indicate the joint location at which the axial yarn is bonded with helical yarn. Therefore, these are certain constraints provided by the helical yarns at the joint locations of the axial yarn. As it is introduced in the cord-preg Chapter 3, the helical yarn has a huge Poisson's strain effect in lateral direction when the helical yarn is loaded in the longitudinal direction. The reaction force in radial direction is generated from axial yarn on helical yarns in order to keep helical yarns contracting or expanding in radial direction. The constraining radial force is depicted in Figure 35. The free body diagram for the torque applied on the O-ACS can be analyzed similarly because torque can also cause the same radial expansion or contraction effect. The free body diagram analysis is not included here since the bending stiffness can be derived by axial stiffness of each component.

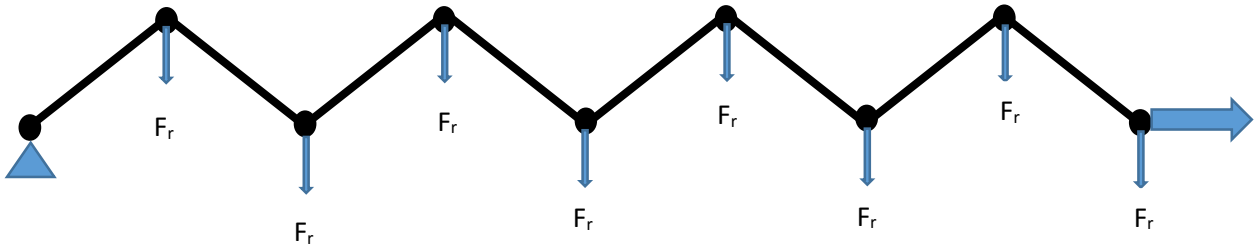

Figure 34 Free body diagram of zigzag axial yarn in O-ACS with 8 braiders

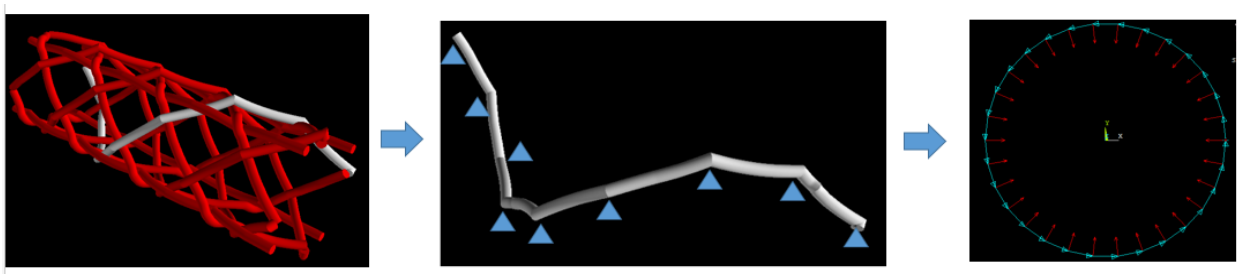

Figure 35 Free body diagram of helical yarn

The radial pressure is related to the force in the hoop direction:

$$PDZ = 2F_x$$

$$F_x = F\sin\theta$$

$$F = \frac{N}{cos\theta}$$

Then the radial pressure is expressed as a function of the longitudinal force N, braiding angle θ, and core diameter D.

$$P = \frac{2Ntan\theta}{DZ} = \frac{2Ntan^2\theta}{\pi D^2}$$

$$F_r = N * tan\theta * t$$

Energy Method and Equivalent Stiffness

The force and moment applied on braider yarn can be written in the form of local coordinate system:

$$\hat{F}_{braider} = F_{x'}\overrightarrow{e_{x'}} + F_{y'}\overrightarrow{e_{y'}} + F_{z'}\overrightarrow{e_{z'}}$$

$$\hat{M}_{braider} = M_{x'}\overrightarrow{e_{x'}} + M_{y'}\overrightarrow{e_{y'}} + M_{z'}\overrightarrow{e_{z'}}$$

Similarly for axial yarn:

$$\hat{F}_{axial} = F_{x''}\overrightarrow{e_{x''}} + F_{y''}\overrightarrow{e_{y''}} + F_{z''}\overrightarrow{e_{z''}}$$

$$\widehat{M}_{axial} = M_{x''}\overrightarrow{e_{x''}} + M_{y''}\overrightarrow{e_{y''}} + M_{z''}\overrightarrow{e_{z''}}$$

The total strain energy is:

$$U_{braider} = \int \left(\frac{{M_{x'}}^2}{2E_f I_{xx}} + \frac{{M_{y'}}^2}{2E_f I_{yy}} + \frac{{M_{z'}}^2}{2G_t J} + \frac{\gamma {F_{x'}}^2}{2G_s A} + \frac{\gamma {F_{y'}}^2}{2G_s A} + \frac{{F_{z'}}^2}{2E_l A}\right) dl$$

$$U_{axial} = \int \left(\frac{{M_{x''}}^2}{2E_f I_{xx}} + \frac{{M_{y''}}^2}{2E_f I_{yy}} + \frac{{M_{z''}}^2}{2G_t J} + \frac{\gamma {F_{x''}}^2}{2G_s A} + \frac{\gamma {F_{y''}}^2}{2G_s A} + \frac{{F_{z''}}^2}{2E_l A}\right) dl$$

where

E_l: tensile modulus of the yarn

E_f: flexural modulus of the yarn

G_t: torsional shear modulus of the yarn

G_s: short beam shear modulus of the yarn

I_{xx}: area moment of inertia with respect to the local x axis

I_{yy}: area moment of inertia with respect to the local y axis

J: area moment of inertia with respect to the local z axis

A: cross-sectional area of the yarn

γ: cross-sectional shape coefficient for shear stiffness

$F_{x'}$, $F_{y'}$, $F_{z'}$, $M_{x'}$, $M_{y'}$, $M_{z'}$: force and moment components in the local coordinate

Tension Scenario

The total force applied on braider and helical yarns are given respectively:

$$\hat{F}_{B\_tension} = \left[F_{r\_b}, V_b, N_{z\_b}\right]\begin{Bmatrix}\overrightarrow{e_r}\\ \overrightarrow{e_v}\\ \overrightarrow{e_{zr}}\end{Bmatrix} = \left[F_{r\_b}, V_b, N_{z\_b}\right]\begin{bmatrix} cos(t) & sin(t) & 0\\ -sin(t) & cos(t) & 0\\ 0 & 0 & 1\end{bmatrix}\begin{Bmatrix}\overrightarrow{e_x}\\ \overrightarrow{e_y}\\ \overrightarrow{e_z}\end{Bmatrix}$$

$$= \left[F_{r\_b}, V_b, N_{z\_b}\right]\begin{bmatrix} cos(t) & sin(t) & 0\\ -sin(t) & cos(t) & 0\\ 0 & 0 & 1\end{bmatrix}[T]\begin{Bmatrix}\overrightarrow{e_{x\prime}}\\ \overrightarrow{e_{y\prime}}\\ \overrightarrow{e_{z\prime}}\end{Bmatrix}$$

$$\hat{F}_{A\_tension} = \left[F_{r\_a}, V_a, N_{z\_a}\right]\begin{Bmatrix}\overrightarrow{e_r}\\ \overrightarrow{e_v}\\ \overrightarrow{e_{zr}}\end{Bmatrix} = \left[F_{r\_a}, V_a, N_{z\_a}\right]\begin{bmatrix} cos(t) & sin(t) & 0\\ -sin(t) & cos(t) & 0\\ 0 & 0 & 1\end{bmatrix}\begin{Bmatrix}\overrightarrow{e_x}\\ \overrightarrow{e_y}\\ \overrightarrow{e_z}\end{Bmatrix}$$

$$= \left[F_{r\_a}, V_a, N_{z\_a}\right]\begin{bmatrix} cos(t) & sin(t) & 0\\ -sin(t) & cos(t) & 0\\ 0 & 0 & 1\end{bmatrix}[A]^{-1}\begin{Bmatrix}\overrightarrow{e_{x\prime\prime}}\\ \overrightarrow{e_{y\prime\prime}}\\ \overrightarrow{e_{z\prime\prime}}\end{Bmatrix}$$

N_{z_b}, N_{z_a} are the exterior tensile forces of interest applied in the longitudinal direction, whereas $F_{r\_a}, V_a, F_{r\_b}, V_b$ are just the reaction forces in radial and hoop direction.

Given an arbitrary point P $\left(Rcos(t), Rsin(t), \frac{R}{tan(\alpha)}t\right)$ on the helical yarn, and the starting point O $(R, 0, 0)$, the vector OP is :

$$\overrightarrow{OP} = \left(Rcos(t) - R, Rsin(t), \frac{R}{tan(\alpha)}t\right)$$

The corresponding moment applied on braider yarn:

$$\hat{M}_{B\_tension} = \overrightarrow{OP} \times \hat{F}_{B\_tension}$$

Given an arbitrary point P' $\left(\left(R - L * tan(\theta)\right) * \cos\left(\frac{2\pi}{N} i\right), \left(R - L * tan(\theta)\right) * \sin(\frac{2\pi}{N} i), \frac{Rt}{\tan(\alpha)}\right)$ on the helical yarn, and the starting point O' $\left((R) * \cos\left(\frac{2\pi}{N} i\right), (R) * \sin(\frac{2\pi}{N} i), 0\right)$, the vector O'P' is :

$$\overrightarrow{O'P'} = \left(-L * tan(\theta) * \cos\left(\frac{2\pi}{N} i\right), -L * tan(\theta) * \sin\left(\frac{2\pi}{N} i\right), \frac{R}{tan(\alpha)} t\right)$$

The moment applied on axial yarn:

$$\widehat{M}_{A\_tension} = \overrightarrow{O'P'} \times \widehat{F}_{A\_tension}$$

Because the radial reaction force is applied on each joint location, the force and moment must be calculated individually at each section between the joints. The total strain energy is summation of strain energy within each section:

$$U_{B\_tension} = \sum_{i=1}^{s\_b} (U_b)_i$$

$$U_{A\_tension} = \sum_{i=1}^{s\_a} (U_a)_i$$

Equivalent axial stiffness of the helical yarn:

$$EA_b = \frac{{N_{z\_b}}^2 L}{2U_{B\_tension}}$$

where the strain energy of braider under tension $U_{B\_tension}$ is a function of each component in $\hat{F}_{B\_tension}\ and\ \hat{M}_{B\_tension}$

The equivalent axial stiffness of the axial yarn:

$$EA_a = \frac{{N_{z\_a}}^2 L}{2U_{A\_tension}}$$

Where the strain energy of axial yarn under tension $U_{A\_tension}$ is a function of each component in $\hat{F}_{A\_tension}\ and\ \hat{M}_{A\_tension}$

The total axial stiffness is the sum of each axial and braider yarn in the O-ACS.

$$EA_{total} = \sum_{i=1}^{N_a} (EA_a)_i + \sum_{i=1}^{N_b} (EA_b)_i$$

where $N_a\ and\ N_b$ are the total number of axial yarns and braider yarns in the O-ACS.

Torsion Scenario

Torque about global z axis is considered to be the same as shear force applied on each component in hoop direction. Total force applied on braider and helical yarns has the same form as in tension scenario:

$$\hat{F}_{B\_torque} = \left[F_{r\_b}, V_b, N_{z\_b}\right] \begin{Bmatrix} \overrightarrow{e_r} \\ \overrightarrow{e_v} \\ \overrightarrow{e_{zr}} \end{Bmatrix} = \left[F_{r\_b}, V_b, N_{z\_b}\right] \begin{bmatrix} cos(t) & sin(t) & 0 \\ -sin(t) & cos(t) & 0 \\ 0 & 0 & 1 \end{bmatrix} \begin{Bmatrix} \overrightarrow{e_x} \\ \overrightarrow{e_y} \\ \overrightarrow{e_z} \end{Bmatrix}$$

$$= \left[F_{r\_b}, V_b, N_{z\_b}\right] \begin{bmatrix} cos(t) & sin(t) & 0 \\ -sin(t) & cos(t) & 0 \\ 0 & 0 & 1 \end{bmatrix} [T] \begin{Bmatrix} \overrightarrow{e_{x'}} \\ \overrightarrow{e_{y'}} \\ \overrightarrow{e_{z'}} \end{Bmatrix}$$

$$\hat{F}_{A\_torque} = \left[F_{r\_a}, V_a, N_{z\_a}\right]\begin{Bmatrix}\overrightarrow{e_r}\\ \overrightarrow{e_v}\\ \overrightarrow{e_{zr}}\end{Bmatrix} = \left[F_{r\_a}, V_a, N_{z\_a}\right]\begin{bmatrix} cos(t) & sin(t) & 0\\ -sin(t) & cos(t) & 0\\ 0 & 0 & 1\end{bmatrix}\begin{Bmatrix}\overrightarrow{e_x}\\ \overrightarrow{e_y}\\ \overrightarrow{e_z}\end{Bmatrix}$$

$$= \left[F_{r\_a}, V_a, N_{z\_a}\right]\begin{bmatrix} cos(t) & sin(t) & 0\\ -sin(t) & cos(t) & 0\\ 0 & 0 & 1\end{bmatrix}[A]^{-1}\begin{Bmatrix}\overrightarrow{e_{x''}}\\ \overrightarrow{e_{y''}}\\ \overrightarrow{e_{z''}}\end{Bmatrix}$$

But in this case, the shear forces in hoop direction V_a, V_b are exterior forces of interest, whereas $F_{r\_a}, N_{z\_a}, F_{r\_b}, N_{z\_b}$ are reaction forces in radial and longitudinal directions.

Equivalent torsional stiffness of the helical yarn:

$$GJ_b = \frac{(V_b * \frac{D}{2})^2 L}{2U_{B\_torsion}}$$

Equivalent torsional stiffness of the axial yarn:

$$GJ_a = \frac{(V_a * \frac{D}{2})^2 L}{2U_{A\_torsion}}$$

$$GJ_{total} = \sum_{i=1}^{N_a}(GJ_a)_i + \sum_{i=1}^{N_b}(GJ_b)_i$$

Bending Scenario

For the axial yarn, based on the mechanics of moment:

$$M = \frac{E_{ef} I}{\rho} = \int E_l \frac{z^2}{\rho} dA$$

$$\left(E_{ef} I\right)_{axial} = \int E_l z^2 dA = EA_a * z^2$$

where ρ is the curvature, z is the radius of the mandrel. If the cross-sectional area is assumed to be very small, the equivalent bending stiffness of zigzag axial yarn is considered to be the product of its equivalent axial stiffness and square of the distance.

The equivalent bending stiffness of a helical yarn is:

$$\left(E_{ef}I\right)_{helical} = EA_b * h^2$$

where h is the distance of the center point to x axis as shown in Figure 36.

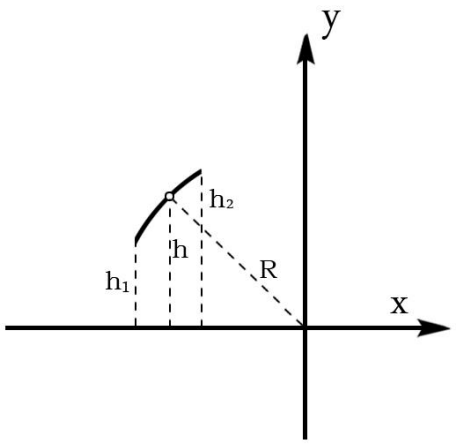

Figure 36 Illustration of the section between joints within a helical yarn

Results and Discussions

The stiffness of 15 different O-ACS was measured in the work by Gurley (Design and Analysis of Optimal Braided Composite Lattice Structures, 2014). The architecture of 15 O-ACS are given in Table 8. These data will be used as experimental data to validate the analytical model based on energy method. The stiffness calculated based on the analytical solution is given in Table 9. Because the stiffness of axial and helical yarns is calculated individually, their contribution can also be reflected for further understanding of the structure. As compared to the experimental data,

the analytical solution has about 13.5%. 14.2, and 11.5% error for axial stiffness, bending stiffness, and torsional stiffness, respectively as shown in Table 10. A minus sign means the value predicted by the analytical solution is lower than the experimental data. The contribution of both axial yarn and helical yarn to the stiffness is given in Table 11. The axial yarn is responsible for at least 99% of the axial and bending stiffness in O-ACS, where helical yarn accounts for about 95% of torsional stiffness. This conclusion intuitively fits the optimization solution for tension, bending and torsion scenario.

Table 8 Manufacture parameter data for O-ACS (Gurley, 2014)

Sample	Mandrel diameter (mm)	Braiding angle (deg.)	Number of axials	Visualization
1	25.4	30	4	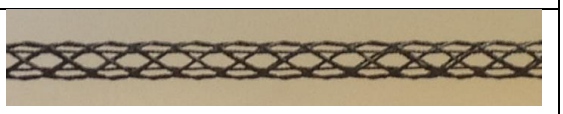
2	63.5	30	4	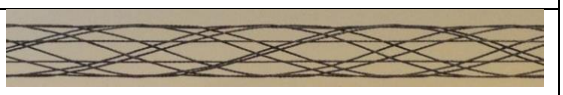
3	25.4	60	4	
4	63.5	60	4	
5	25.4	30	12	
6	63.5	30	12	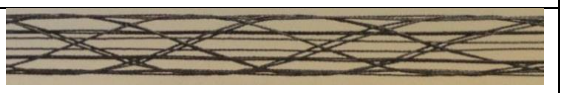
7	25.4	60	12	
8	63.5	60	12	

9	44.45	45	8	
10	25.4	45	8	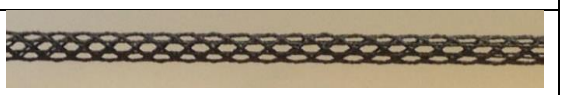
11	63.5	45	8	
12	44.45	30	8	
13	44.45	60	8	
14	44.45	45	4	
15	44.45	45	12	

Table 9 Comparison of the experimental data (axial stiffness EA, bending stiffness EI, torsional stiffness GJ) and analytical solution

0.0254m 30degree 4x4x4

	Helical	Axials	Total	Experiments (KN)
EA	13.432	479.696	493.128	501.7
EI	2.22	74.1	76.32	130.2
GJ	34.56	0.4	34.96	53.51

0.0254m 60degree 4x4x4

	Helical	Axials	Total	Experiments (KN)	Deviation (%)
EA	7.632	466.22124	473.8532	541.8	12.54
EI	1.22	71	72.22	90.5	20.20
GJ	48.24	3.6	51.84	53.06	2.30

0.0635m 30degree 4x4x4

	Helical	Axials	Total	Experiments (KN)	Deviation (%)
EA	2.16	481.172	483.332	511.8	5.56
EI	2.27	465	467.27	386.2	20.99
GJ	138.96	0.4	139.36	148.43	6.11

0.0635m 60degree 4x4x4

	Helical	Axials	Total	Experiments (KN)	Deviation (%)
EA	1.24	478.928	480.168	560.5	14.33
EI	1.3	462	463.3	381.2	21.54
GJ	279.76	3.6	283.36	270.79	4.64

0.0254m 30degree 4x4x12

	Helical	Axials	Total	Experiments (KN)	Deviation (%)
EA	13.432	1439.088	1452.52	1055	37.68
EI	2.22	222	224.22	279	19.63
GJ	34.56	1.2	35.76	43.15	17.13

0.0635m 30degree 4x4x12

	Helical	Axials	Total	Experiments (KN)	Deviation (%)
EA	2.16	1436.784	1438.944	1264	13.84
EI	2.27	1386	1388.27	1178.6	17.79
GJ	138.96	10.8	149.76	126.91	18.00

0.0254m 60degree 4x4x12

	Helical	Axials	Total	Experiments (KN)	Deviation (%)
EA	7.632	1398.66	1406.292	1114	26.24
EI	1.22	213.1	214.32	328.1	34.68
GJ	48.24	10.8	59.04	43.19	36.70

0.0635m 60degree 4x4x12

	Helical	Axials	Total	Experiments (KN)	Deviation (%)
EA	1.24	1436.784	1438.024	1314	9.44

EI	1.3	1386.13	1387.43	1224.7	13.29
GJ	279.76	10.8	290.56	306.55	5.22

0.04445m 45degree 4x4x8

	Helical	Axials	Total	Experiments (KN)	Deviation (%)
EA	3.592	959.464	963.056	957.8	0.55
EI	1.84	453.94	455.78	501.2	9.06
GJ	123.68	2.48	126.16	138.39	8.84

0.0254m 45degree 4x4x8

	Helical	Axials	Total	Experiments (KN)	Deviation (%)
EA	10.92	952.456	963.376	929.9	3.60
EI	1.79	146	147.79	170.2	13.17
GJ	43.92	2.56	46.48	47.3	1.73

0.0635m 45degree 4x4x8

	Helical	Axials	Total	Experiments (KN)	Deviation (%)
EA	1.76	961.216	962.976	1031	6.60
EI	1.8	928	929.8	725.5	28.16
GJ	223.28	2.48	225.76	266.4	15.26

0.04445m 30degree 4x4x8

	Helical	Axials	Total	Experiments (KN)	Deviation (%)
EA	4.408	961.76	966.168	996.7	3.06
EI	2.26	455	457.26	422.8	8.15
GJ	86.96	0.8	87.76	102.2	14.13

0.04445m 60degree 4x4x8

	Helical	Axials	Total	Experiments (KN)	Deviation (%)
EA	2.5352	952.664	955.1992	987.5	3.27
EI	1.28	449	450.28	427.4	5.35
GJ	143.84	7.2	151.04	145	4.17

0.04445m 45degree 4x4x4

	Helical	Axials	Total	Experiments (KN)	Deviation (%)
EA	3.5976	479.732	483.3296	617.9	21.78
EI	1.84	226	227.84	240.4	5.22
GJ	123.68	1.24	124.92	131.41	4.94

0.04445m 45degree 4x4x12

	Helical	Axials	Total	Experiments (KN)	Deviation (%)
EA	3.5976	1439.196	1442.794	1219	18.36
EI	1.84	680	681.84	571.2	19.37
GJ	123.68	3.72	127.4	151.38	15.84

Table 10 Average deviation between the experimental data and analytical solution

	Axial stiffness	Bending stiffness	Torsional stiffness
Average deviation (%)	13.5	14.2	11.5

Table 11 Contribution of axial and helical yarns on stiffness

	Axial yarn contribution (%)	Helical yarn contribution (%)
Axial stiffness (EA)	99.4	0.6
Bending stiffness (EI)	99.3	0.7
Torsional stiffness (GJ)	4.1	95.9

It is observed that the O-ACS with 45 degree braiding angle does not necessarily have the highest torsional stiffness, which counteracts the conclusion from continuum mechanics that the composite tube with 45 degree fiber reinforcement yields the highest torsional stiffness. This is because of the fact that the open truss structure behaves different than a continuous composite tube. The joint location and the section between the joints affects its equivalent stiffness. A simple example is given below to elaborate the importance of joints. The same analytical method is applied to solve the equivalent stiffness of a helix structure:

$$X = Rcos(t)$$

$$Y = Rsin(t)$$

$$Z = \left(\frac{L}{2\pi}\right)t = \frac{R}{tan(\alpha)}t$$

But at this time, the stiffness will be plotted as a function of t which indicates the rotational angle of the helical yarn. Material properties and geometry of the helical yarn are given in Table 12. Figures 37 and 38 plot the relationship between the stiffness and angle variable t. It is shown that the smaller the t, the higher the stiffness. Therefore, the unsupported length between the two adjacent joints directly influences the stiffness of an open truss structure. It is a fact that more bonded joints will increase the stiffness of O-ACS.

Table 12 Material properties and geometry of the helical yarn

Material type	Isotropic
Elastic Modulus (GPa)	106e9
Shear Modulus (GPa)	40.76e9
Poisson's ratio	0.3
Mandrel Diameter (m)	0.4
Braiding Angle (Degree)	45

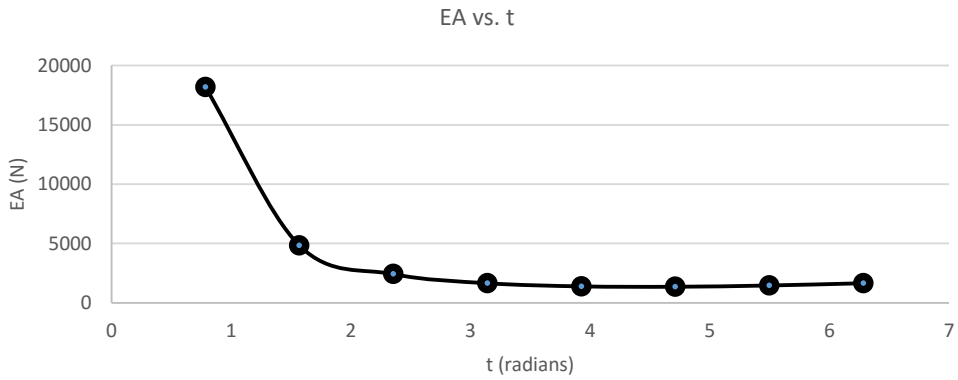

Figure 37 Axial stiffness (EA) vs. t

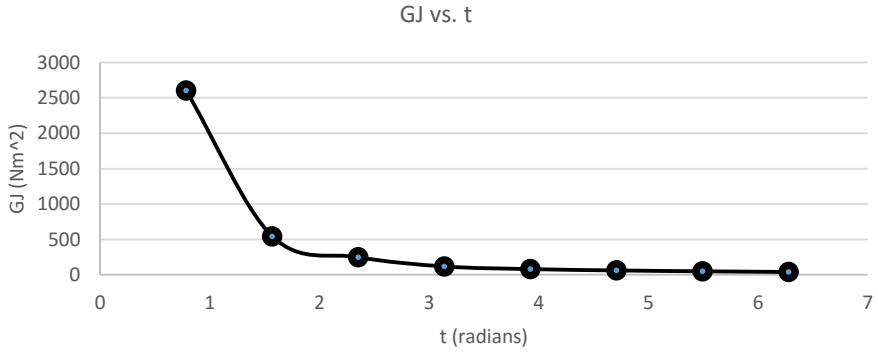

Figure 38 Torsional stiffness (GJ) vs. t

Conclusions

Analytical solution using energy method is proposed to calculate the equivalent stiffness of O-ACS. The method takes the local crimp of axial yarns and reaction force at the joint into consideration. The results from the analytical solution fit well with the experimental data. It is shown that it is the axial yarn that contributes to the majority of axial and bending stiffness, whereas it is the helical yarn that contributes the most to torsional stiffness. The importance of the joint is also explained by this model.

Chapter 6 Failure Analysis of Micro-joints In Open Braided Composite Structures

Abstract

The Open-Architecture Composite Structure (O-ACS) has been designed and demonstrated as a new solution to meet the requirements of minimum weight composite structures. In O-ACS, the composite yarn is connected to each other by epoxy joint, which is critical to the failure behavior of the structure. This chapter discusses the physical test and predictive model of these micro-joints in order to predict the failure behavior of the entire structure under different loading conditions. The FEA model of micro-joint is established and validated with experimental data. The model shows good agreement with the physical tests to predict the strength of the joint. These data will be further used as input to predict the failure behavior of the entire structure.

Introduction

The micro-joints in O-ACS are extremely important since the overall structure is formed by epoxy bonding between the yarns. The structure is held together by overlaying one yarn on top of another, which results in the formation of joints made of yarns and epoxy. The strength of the joint might have a big influence on the strength of the structure under different loading conditions because there is nothing but epoxy at the joint. There are three possible parameters which could affect the bond strength of the joint regardless of the manufacture parameters: bond thickness (epoxy thickness), bond interface between epoxy and yarns, and contact area between epoxy and yarns. The bond strength is considered to be decreased with increasing the bond thickness of the joint. The bond thickness depends on the tension put on the yarn during manufacture process. The yarn can be squeezed more to develop a thinner bond thickness and larger contact area if more tension is put on the yarn. The de-bonding at the interface between yarn and epoxy is another critical issue to be concerned with. The de-bonding strength of the interface directly determines the strength of

the joint. However, improving the interface properties might require surface treatment of yarns and different types of resin, which is beyond the scope of the current stage of research. The last parameter, contact area, can be easily changed by adding extra epoxy resin after the first cure of the structure.

There are three major types of failure modes for the joint as shown in Figure 39.

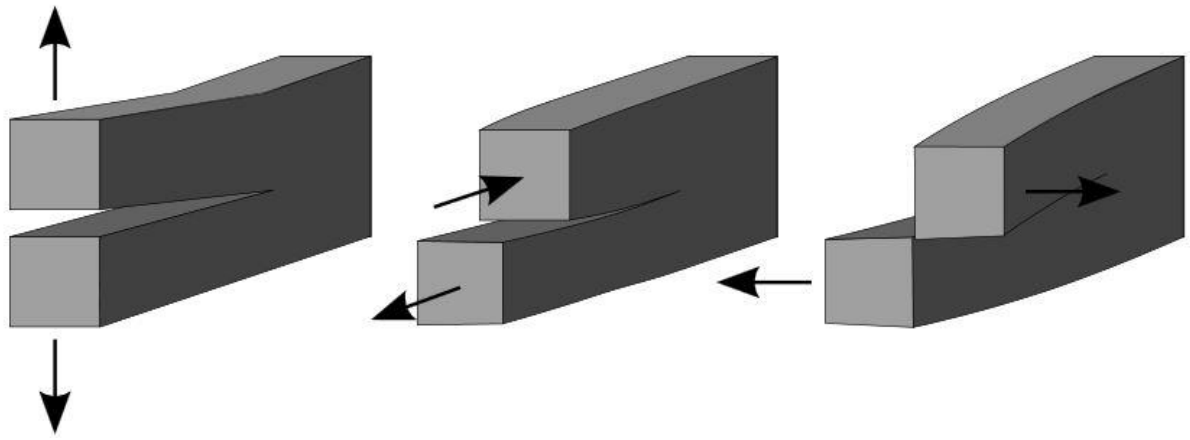

Figure 39 Mode 1, Mode 2, and mixed mode de-bonding modes (Kothari, 2014)

Mode 1 involves the normal separation to the interface, whereas Mode 2 and 3 involve the tangential slip to the interface. Applying these three de-bonding models to our joints leads to two different models: radial separation and tangential slip.

The Finite Element Model of the Joint

Cohesive zone model is well fitted for modeling of the joint. In our particular case, the joint consists of two yarns crossing over each other with epoxy in-between. The following assumptions are made in order to perform the finite element analysis efficiently without losing much accuracy:

1 The yarn has a constant circular cross section.

2 The material property of the yarn is considered to be transversely isotropic and epoxy is isotropic.

3 The interface is perfectly bonded without any defects.

Geometry

The yarn is modeled by a cylinder with a diameter of 2.4 mm. The distance between centroids of top and bottom yarns is defined to be 2.4 mm so that there will be no penetration and a 5% of the total length is added to compensate for the thickness of epoxy. A sphere with radius of 1.2 mm is generated at the center of the joint and the part apart from the intersection between the yarn cylinder and sphere is considered be the epoxy. This technique can easily create shared nodes at the interfaces, which is required for the cohesive zone model. Figure 40 shows the geometry of the joint.

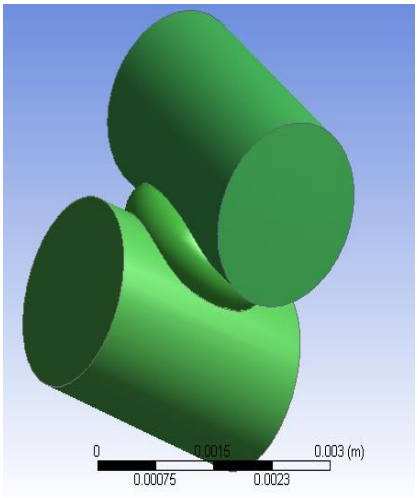

Figure 40 Geometry of the joint

Material Properties

The epoxy can be assumed to have isotropic property. However, material property of composite yarn is transversely isotropic. The transversely isotropic material property of yarn and isotropic property of epoxy are shown in Table 13. The longitudinal modulus E1, transverse modulus E2, in plane shear modulus G23 and Poisson's ratio V12 were obtained from the physical tests. The out of plane shear G12 is assumed to be the same as the shear modulus of epoxy.

Table 13 Material properties of composite yarn and epoxy resin

	E1 (GPa)	E2 (GPa)	G12 (GPa)	G23 (GPa)	V12
Composite yarn	106	1.68	1.04	1.05	0.29

	E (GPa)	V(Poisson's ratio)
Epoxy resin	2.83	0.35

Element and Mesh

The selection of element for the finite element analysis is important because it can directly affect the accuracy of the results. Both solid and plate elements have been widely used for joint study. The plate element is fitted for the case of neglected bond thickness compared to the thickness of the adherend. The bond thickness in our case cannot be neglected; therefore the element used in the simulation is 20 nodes brick solid element.

The mesh is generated by the sweeping method and its axis is symmetric due to transverse isotropic nature of the composite yarn as shown in Figure 41.

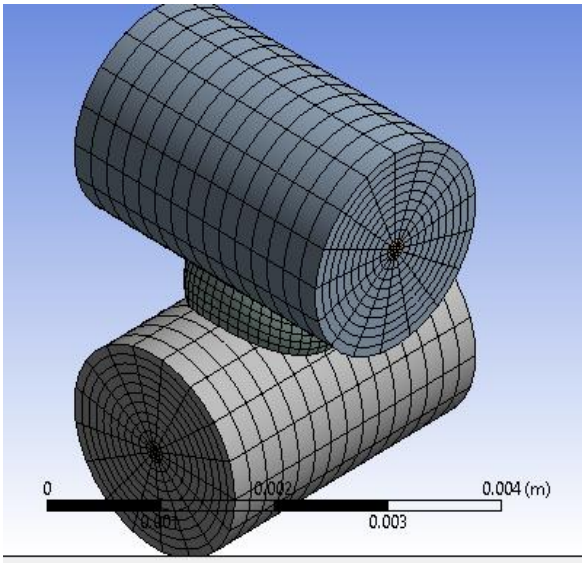

Figure 41 Axial symmetrical mesh

Boundary Conditions

The boundary conditions are shown in Figure 42 for radial separation test and tangential slip test. The end surface of top yarn is fixed and the end surface of the other yarn is applied a normal force for radial separation or a tangential force for tangential slip.

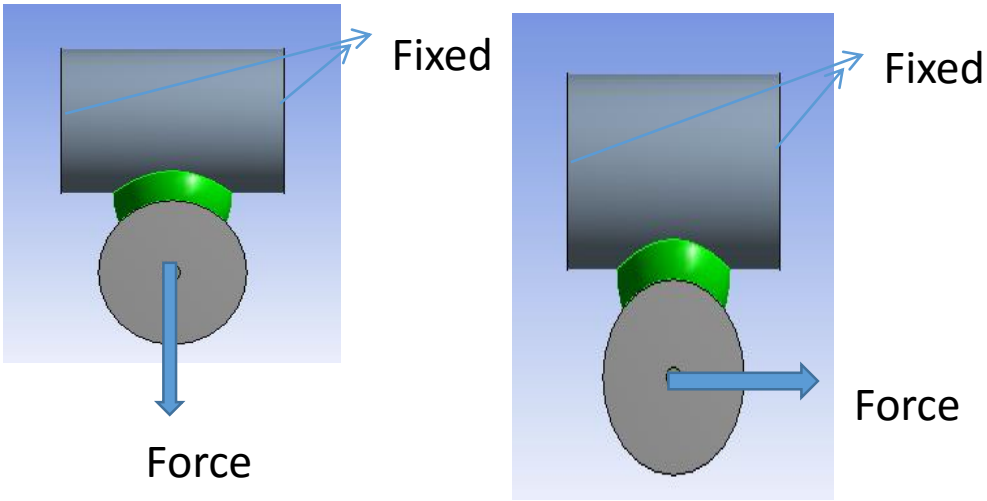

Figure 42 Boundary conditions for radial separation test and tangential slip test

Cohesive Zone Model

The cohesive zone model has been developed to model the de-bonding of the interface. The interface surfaces of the materials can be represented by a special set of interface elements or contact elements, and a CZM model can be used to characterize the constitutive behavior of the interface. The CZM model consists of a constitutive relation between the traction T acting on the interface and the corresponding interfacial separation δ (displacement jump across the interface). The definitions of traction and separation depend on the element and the material model. The constitutive equation defined in the cohesive zone model is shown in Figure 43. The surface traction gradually grows with the separation distance. The failure begins when the traction reaches the maximum and then the traction starts to decrease to complete failure. The maximum traction and maximum separation distance were calculated from the physical test data of radial separation and tangential slip.

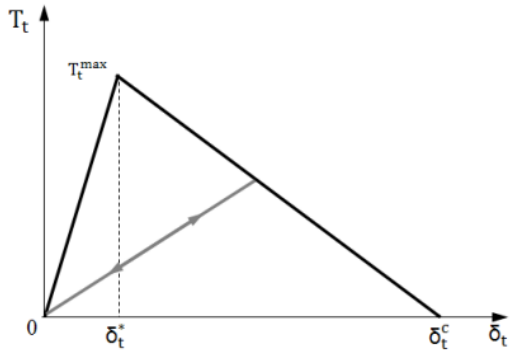

Figure 43 Constitutive equation plot for cohesive zone model

Physical Test of the Strength of the Joint

As it is discussed in the previous section, the strength test of the joint should include the radial separation and shear separation. In order to accurately obtain the strength of the joints in the structure, the joint sample is directly cut from the structure (Figure 44). The joint sample was fixed through two pairs of hook (Figure 45).

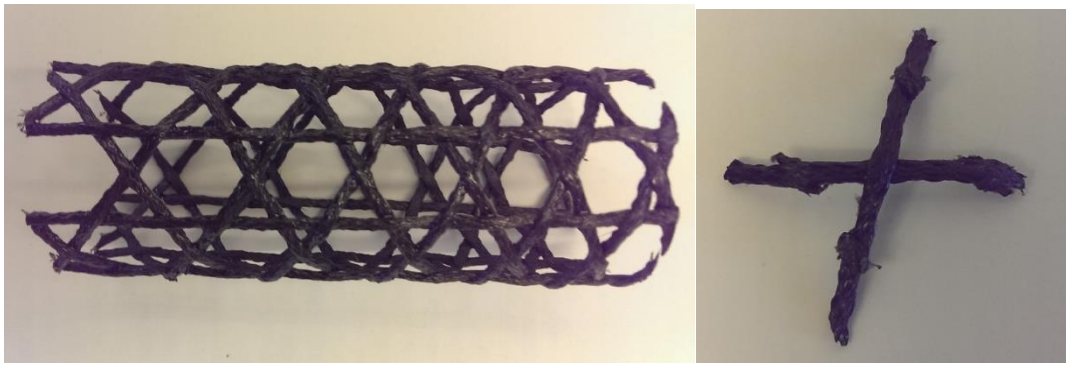

Figure 44 Joint samples for test

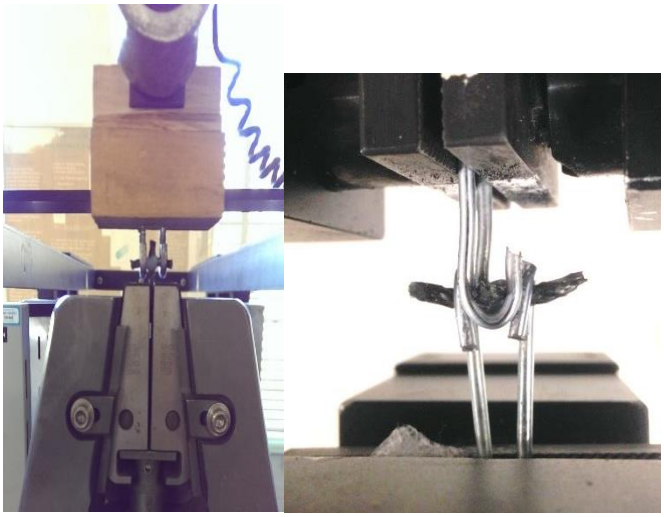

Figure 45 Test configuration

Results and Verification

The reaction force was recorded as a function of deformation. The maximum force was recorded at the initiation of de-bonding as shown in Figure 46.

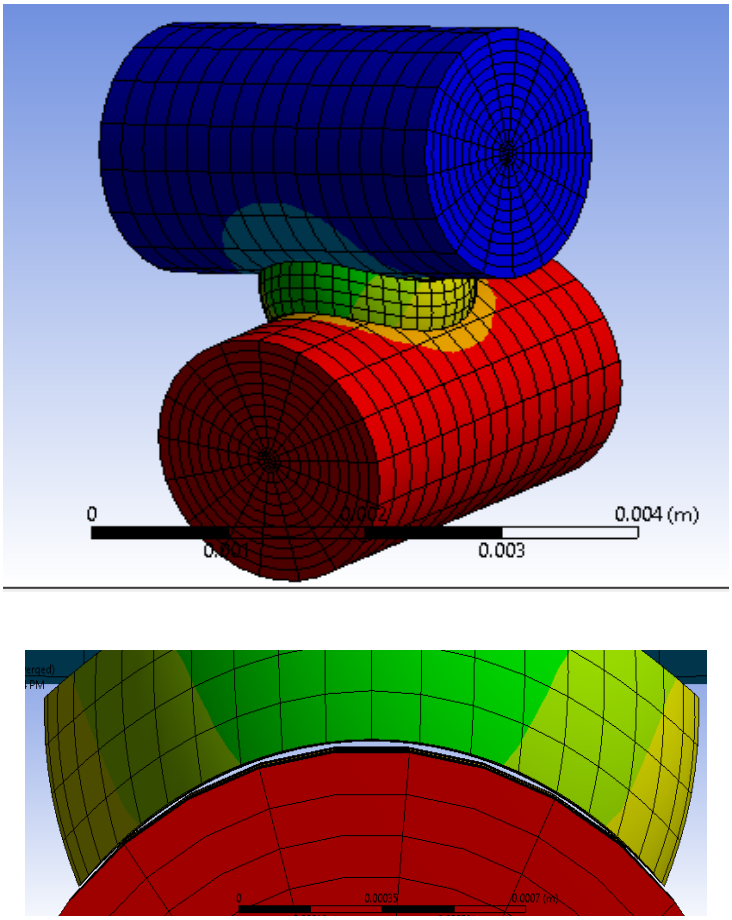

Figure 46 Stress distribution and de-bonding initiation

Figure 47 shows the effect of mesh density on reaction force. That the reaction force converged to a value around 84 N with the increasing number of elements. The minimum number of elements to obtain a good result is 2100. Figures 48 and 49 show the comparison between the FEA results and the experimental data. The radial separation, predicting a maximum force value of 84 N, agrees well with the experimental data. However, tangential slip predicts a maximum value around 150 N, which is lower than the experimental result.

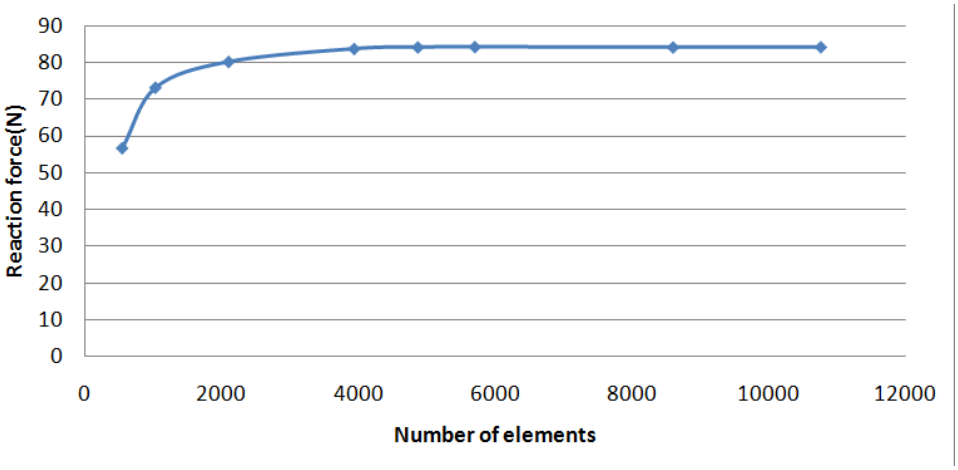

Figure 47 Study of element size for radial separation

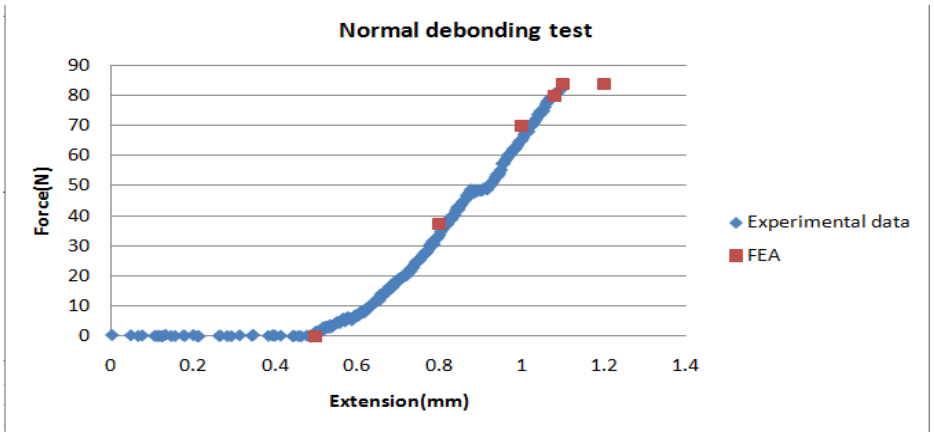

Figure 48 Comparison between FEA and experimental data for radial separation

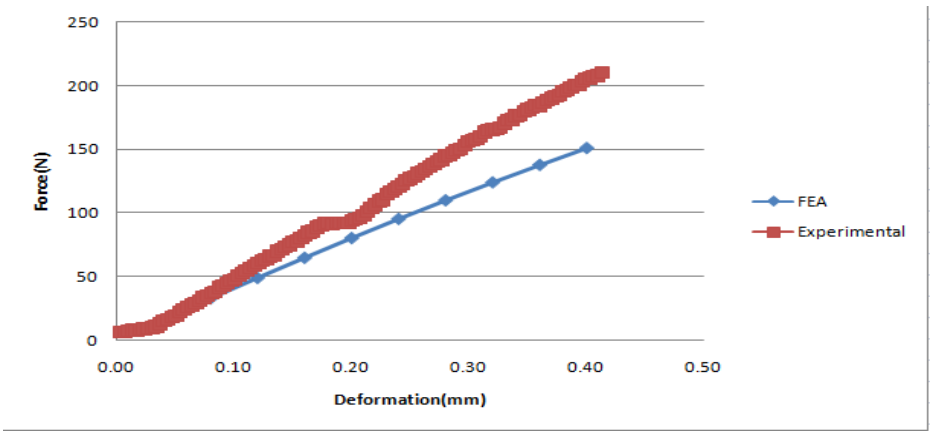

Figure 49 Comparison between FEA and experimental data for tangential slip

Conclusions

The de-bonding of the joint in O-ACS has been studied in this chapter. The finite element model based on the cohesive zone material model is established for predicting the de-bonding behavior of the joint. The finite element model also includes the detailed geometry generation and appropriate mesh technique. The result for de-bonding in radial direction is in good agreement with the experimental data.

Chapter 7 Failure Analysis of O-ACS using FEA

Abstract

This chapter is about the failure behavior of Open-Architecture Composite Structures under tension, compression, bending, and torsion. The failure criterion which is based on joint de-bonding, material yielding, and buckling is established to examine possible failure modes. The finite element model generation program is developed to automatically output various O-ACS finite element models as APDL for ANSYS. The effect of varying braiding angle and mandrel diameter is considered using parametric analysis. It is indicated that this model can predict the failure strength of O-ACS under different loading conditions and provide useful guidance for optimal design.

Introduction

Open-Architecture Composite Structures (O-ACS) have been developed in recent years for rapid manufacturing of open lattice structures. O-ACS is made of composite yarns using braiding technique. One advantage of O-ACS is that it offers very high stiffness to weight ratio, which is particularly useful for the space industry where lightweight is essential. The mechanical properties characterization of truss lattice structure is as important as manufacture since understanding of the mechanical properties can fundamentally guide the structural design which leads to optimization. While the stiffness of a truss lattice can be predicted using analytical solution based on homogenization and finite element method, the strength prediction is more difficult to comprehend as such structure could have numerous failure modes. Many investigations have been done to study the buckling behavior of truss lattice both analytically and numerically. However, buckling mode does not include the joint failure such as de-bonding of the resin at junction and composite failure.

The possible failure modes of a truss lattice may be significantly affected by the fiber reinforcement, resin, bonding, and the buckling behavior which is closely related to the geometry.

The buckling failure is a geometrical instability, which draws more attention than the other failure mode because buckling usually occurs before intrinsic material failure. It is possible that O-ACS with high stiffness may buckle at much lower stress than the material yielding stress due to buckling. Eigenvalue and nonlinear solution can be used for obtaining. However, such methods in FEA employs the model in which each truss member shares a common node at the joint location; The joint effect is not included in the analysis.

The strength of composite is highly directional in nature. The strength in fiber direction is usually much higher than the strength in transverse direction. Compressive strength is lower than the tensile strength. Different failure modes such as fiber failure, matrix failure, and fiber micro-buckling are taken into account for deriving micromechanical models. The direction of the stress must be considered carefully when failure criterion is established to examine the failure in structure.

Another failure mode specific to the truss frame structure is the joint failure. Most analysis in the past ignored the failure at joint assuming a perfect bonding condition. There are some loading conditions which may apply significant force on the joint location resulting in joint de-bonding or delamination. This effect can be simulated by robust delamination models such as cohesive zone material model to find out exact force for delamination. In an O-ACS, the axial yarns and helical yarns are connected together by adhesively bonding. The joint strength is determined by the fiber and resin properties as well as the interface property between the fiber and matrix.

The aim of this research is to propose a method to examine failure in O-ACS. The failure modes take yarn failure, joint de-bonding and buckling into consideration.

Failure Mode Analysis

The initial analysis of possible failure modes starts with the observation of O-ACS under compression. When a compressive force is applied on the O-ACS, the structure starts to expand in lateral direction. If the unsupported length which is referred as span length is long enough, the axial yarn can buckle out at the location of joint rather than buckle within the unsupported length. Meanwhile, if the joint is not strong enough, the joint between axial yarn and helical yarn will de-bond before the axial yarn starts to lose stability. After the joint is de-bonded, the structure can still take more load until it reaches the critical buckling load of the new unsupported length. The stress in the composite yarn may exceed the tensile or compressive strength of the yarn, which is considered as a composite yarn failure or composite yarn yielding. The summary of all the failure modes in O-ACS is given in Table 14.

Table 14 Failure modes for O-ACS

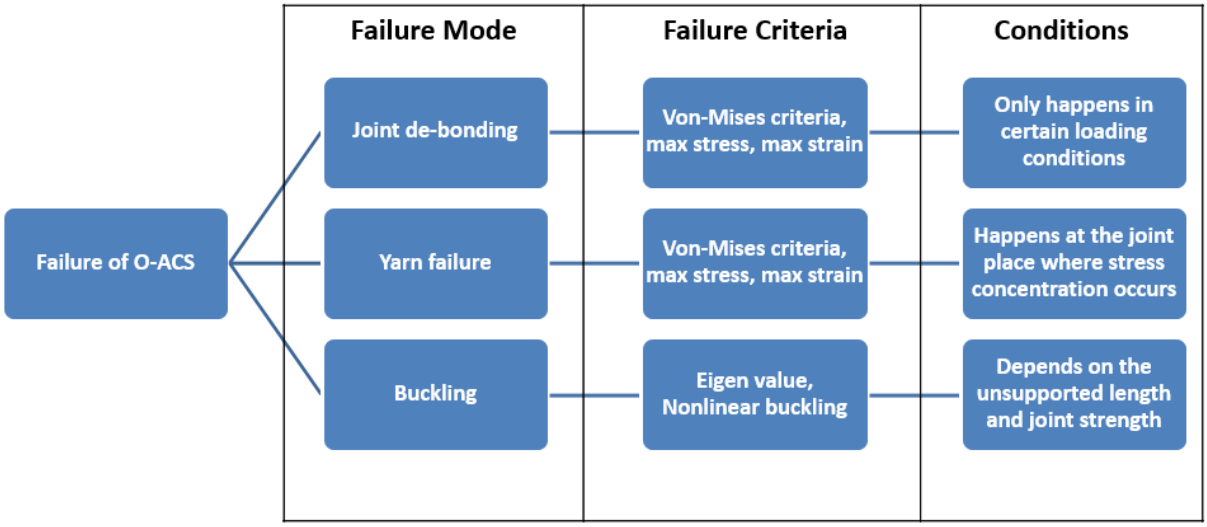

Joint De-bonding

The joint is simulated by a beam element which is defined with the axial modulus and shear modulus. As introduced in Chapter 6, a detailed finite element model which is implemented with the cohesive zone model was established to analyze the failure of the joint. However, the finite element solution is complicated and time-consuming. Therefore, a simplified model is preferred over the finite element model. Upon observation of the cross-section of the joint, the top yarn and bottom yarn are compressed such tightly that they are meshed as one integrated part (Figure 50). Therefore, the joint properties can be simulated by homogenized laminate properties. Similarly, the tensile strength of the joint is equivalent to the transverse tensile strength of composite and the shear strength of the joint is the same as the shear strength of composite yarn. Using Tsai-Wu's quadratic failure criterion, the envelope equation can be simplified into:

$$F_{11}{\sigma_1}^2 + F_{66}{\sigma_6}^2 + F_1\sigma_1 = 1$$

$F_{ij}\ and\ F_i$ are the strength tensors that will be experimentally determined. σ_1 is the principle stress in axial direction; σ_6 is the shear stress.

$$F_{11} = \frac{1}{{S_L}^{(+)}{S_L}^{(-)}}$$

$$F_1 = \frac{1}{{S_L}^{(+)}} - \frac{1}{{S_L}^{(-)}}$$

$$F_{66} = \frac{1}{{S_{LT}}^2}$$

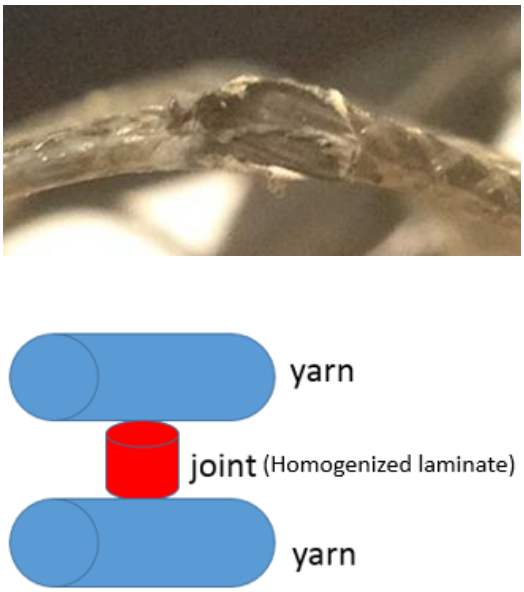

Figure 50 Equivalent beam for modeling joint

The element which has the maximum stress will be identified and the maximum stress will be recorded at every time step in the nonlinear iteration. The corresponding force or moment will be taken as the maximum force or moment when the maximum stress reaches the yielding stress.

Yarn Failure

The quadratic interaction theory can be used for establishing failure criterion of the composite yarn. Only axial and shear force are considered in the beam element. Since the loading conditions are tension, compression, bending, and torsion, the shear force applied on the yarn is considered to be much smaller than the axial force in these conditions. Therefore, the quadratic interaction failure criterion can be simplified into maximum stress failure criterion in axial direction.

Buckling

Buckling analysis is achieved by finite element method. The global geometrical matrix of the entire model which is based on beam element is formed to calculate the eigenvalue under different loading conditions. The nonlinear critical buckling load is also calculated when solution fails to

converge. Buckling behavior can be categorized into global buckling and local buckling. The global buckling refers to a shape change over the entire structure, whereas local buckling refers to the loss of stability within a small section on an individual member. The local buckling is considered to be the dominating buckling failure mode. It was found that a typical O-ACS could only have global buckling failure when the length is up to 3 or 4 meters. Unless specified otherwise, the buckling failure mode in the following analysis always indicates the local buckling failure. The global buckling will be briefly discussed at the end.

Finite Element Model

The finite element code generation program is written in Matlab to output APDL file for Ansys. The program can load the coordinates which are generated from Fellpoint (Gurley, 2014) and define all the necessary components for FEA such as joint search, element type, and boundary conditions. This automation process facilitates parametrical analysis using finite element method. The Timoshenko beam element is used for the analysis. The standard procedure for failure analysis of O-ACS is given in Figure 51.

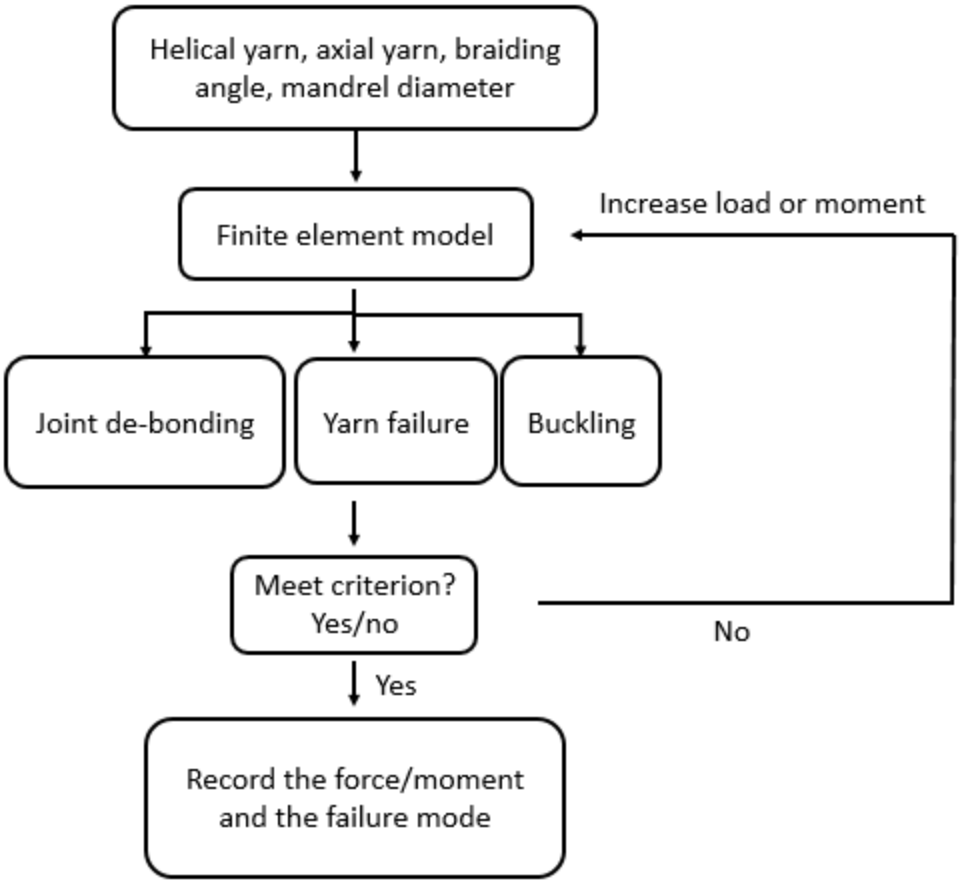

Figure 51 Standard chart flow for failure analysis of O-ACS

Eight different O-ACS models are built as shown in Table 15 to study the effect of braiding angle and mandrel diameter. The braiding angle is the angle between helical yarn and mandrel direction. Each O-ACS has 4 clockwise helical yarns, 4 counterclockwise helical yarns and 4 axial yarns. The architecture of each O-ACS is true triaxial structure. Table 16 gives material properties for the yarn and joint which was derived from the micromechanical models introduced in Chapter 3.

Table 15 O-ACS models in FEA

Samples	Braiding angle (degree)	Mandrel diameter (m)	Visualization
1	22.5	0.04445	
2	33.5	0.04445	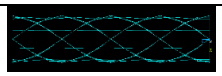
3	45	0.04445	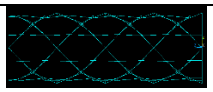
4	56.5	0.04445	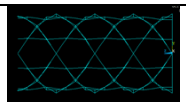
5	67.5	0.04445	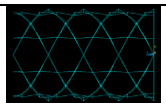
6	45	0.0254	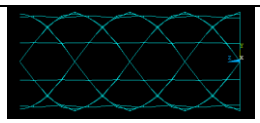
7	45	0.0635	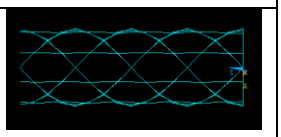
8	45	0.0835	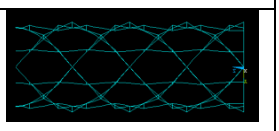

Table 16 Material properties of the yarn and joint (derived from micromechanics introduced in Chapter 3)

	Axial modulus (GPa)	Shear modulus (GPa)	Tensile strength (MPa)	Compressive strength (MPa)	Shear strength (MPa)
Composite yarn	160	15	2000	1000	125
Joint	15	15	70	70	125

Axial Compression

Buckling Failure under Compression

The data of eigenvalue and nonlinear solution for different braiding angle O-ACS buckling under compression is given in Table 17. Figure 52 shows the plot of critical buckling as a function of braiding angle for the same mandrel diameter. It is indicated that critical buckling load increases with higher braiding angle, which can be explained by the fact that increasing braiding angle decreases the unsupported length. Table 18 and Figure 53 show the results for O-ACS with different mandrel diameters. It is shown that higher mandrel diameter at the same braiding angle can result in lower critical buckling load. However, this trend starts to slow down as the slop of the curve gradually decreases. It must be pointed out that the buckling analysis at this moment assumes that there is no yarn failure or joint de-bonding. The critical buckling load in this analysis is not the actual compressive load.

Table 17 Eigenvalue and nonlinear solution for various braiding angles

0.04445m mandrel diameter O-ACS with different braiding angles (degree)	Buckling shape (undeformed and buckled shape)	Critical buckling load by eigenvalue solution (N)	Critical buckling load by nonlinear solution (N)
22.5	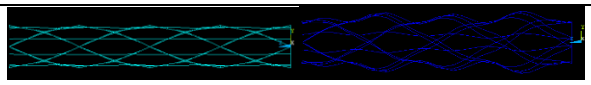	2864	2243.2
33.5	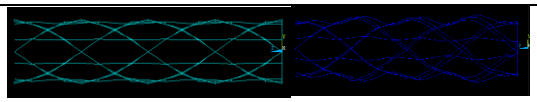	6248	4800
45	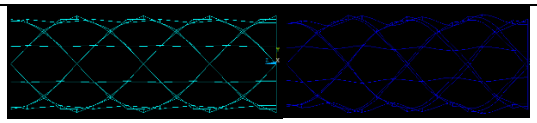	10742	9987
56.5	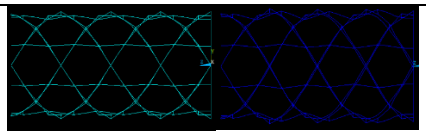	17268	16660
67.5	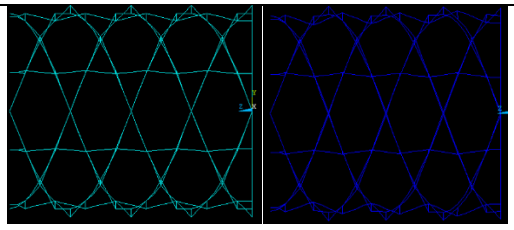	26897	26304

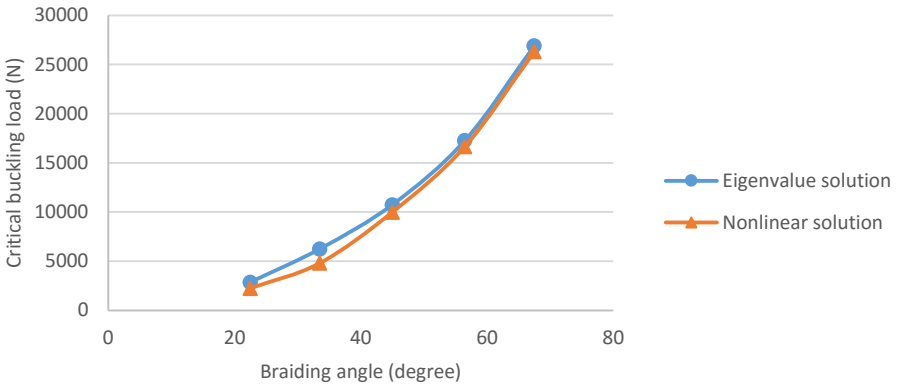

Figure 52 Critical buckling load from eigenvalue solution vs. braiding angle

Table 18 Eigenvalue and nonlinear solution for various mandrel diameters

45degree braiding angle mandrel O-ACS with different mandrel diameters (m)	Buckling shape (undeformed and buckled shape)	Critical buckling load by eigenvalue solution (N)	Critical buckling load by nonlinear solution (N)
0.0254	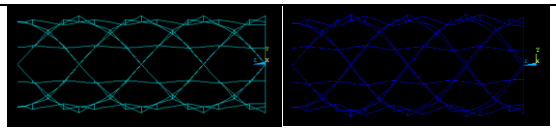	23270	22500
0.04445	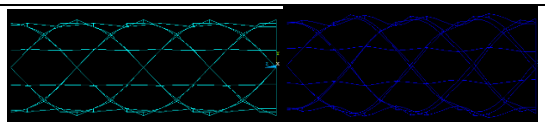	10742	9987
0.0635	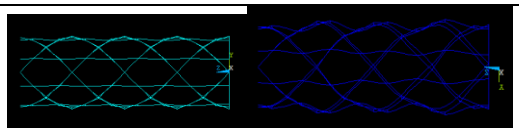	5869.8	5120
0.0835	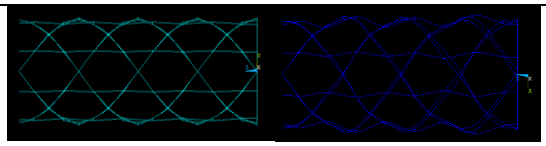	5001	5202

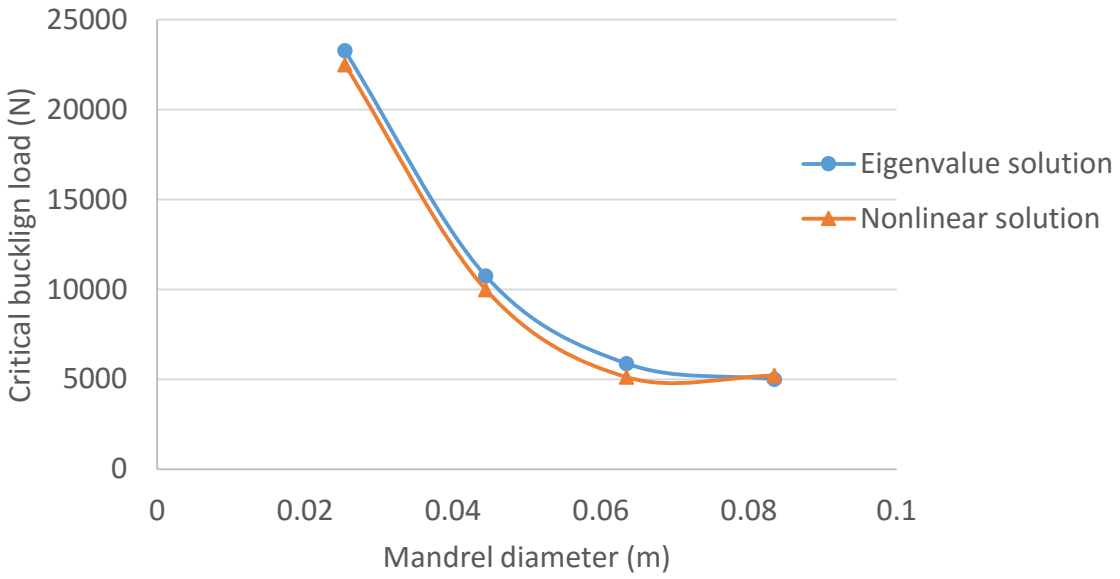

Figure 53 Critical buckling load vs. mandrel diameter

Yarn Failure under Compression

Tables 19, 20 and Figures 54, and 55 show the results for maximum compressive force based on yarn failure criterion. It is indicated that 45 degree braiding angle has the highest maximum compressive force at failure, which means that O-ACS with 45 degree braiding angle has the lowest stress concentration at the joint location. This can be explained by the micro-crimp effect of the axial yarn. It is shown that the mandrel diameter does not affect the compressive strength much since the variation is small.

Table 19 Maximum compressive force for the yarn failure criterion for O-ACS with different braiding angles

Braiding angle (degree)	The element with maximum stress	Maximum compressive force at failure (N)
22.5	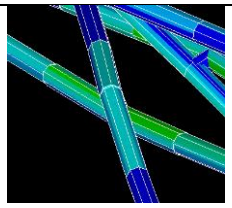	1614
33.5	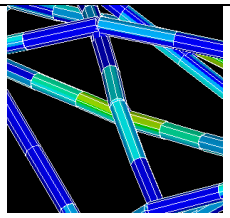	2100
45	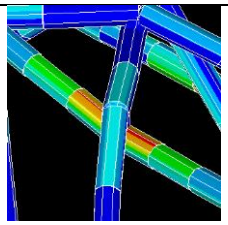	2588
56.5	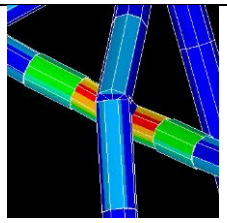	2378
67.5	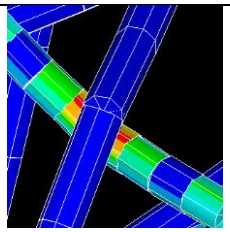	2120

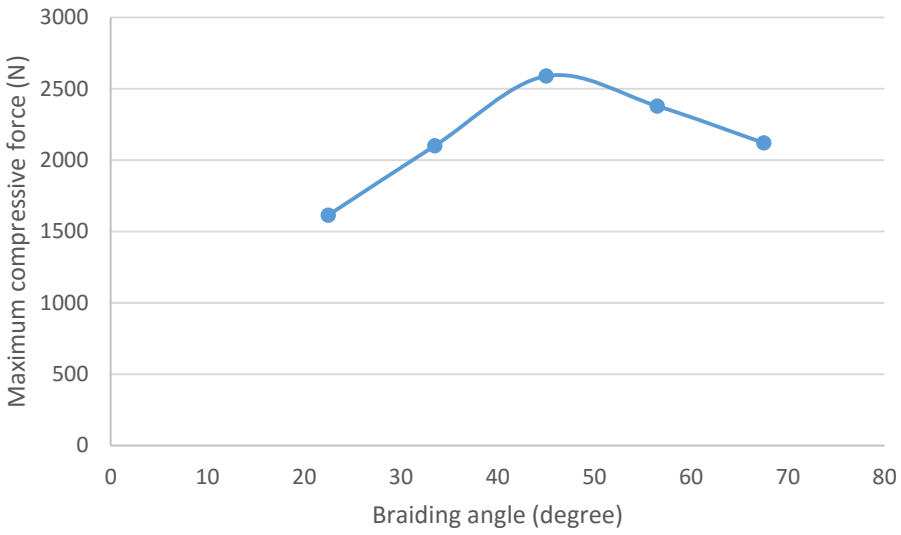

Figure 54 Maximum compressive force for the yarn failure criterion vs. braiding angle

Table 20 Maximum compressive force for the yarn failure criterion for O-ACS with different mandrel diameters

Mandrel diameter (m)	The element with maximum stress	Maximum compressive force at failure (N)
0.0254	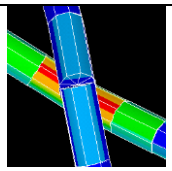	2571
0.0445	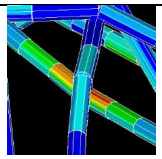	2588
0.0635	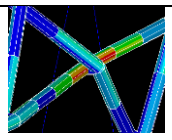	2560
0.0835	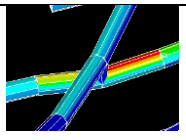	2520

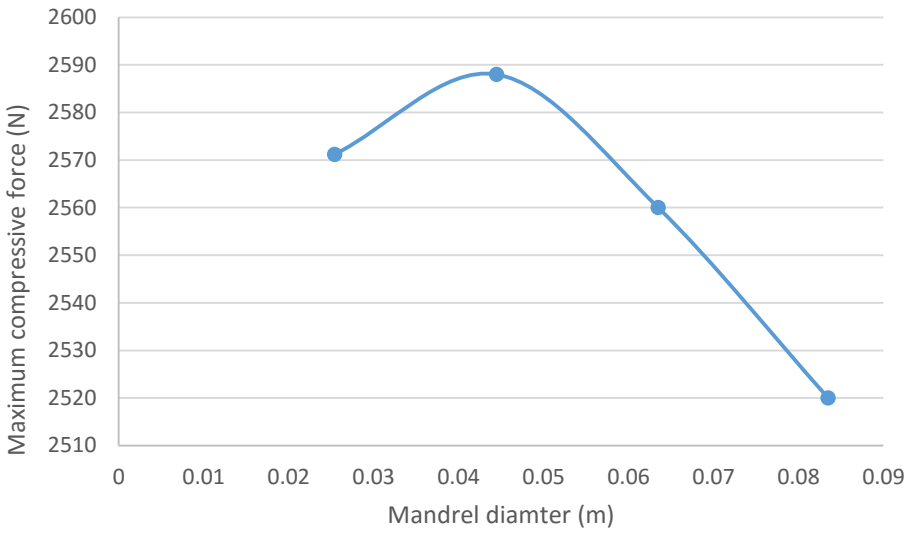

Figure 55 Maximum compressive force for the yarn failure criterion vs. mandrel diameter

Joint De-bonding under Compression

The results of maximum compressive force based on joint de-bonding are given in Tables 21 and 22. The data reflect that braiding angle affects the joint de-bonding failure, whereas mandrel diameter does not. Relatively low braiding angle can cause the joint de-bonding first before the stress reaches the yielding point.

Table 21 Maximum compressive force for the joint de-bonding failure criterion for O-ACS with different braiding angles

Braiding angle (degree)	Maximum compressive force at failure (N)
22.5	1506
33.5	1770
45	NA
56.5	NA
67.5	NA

Table 22 Maximum compressive for the joint de-bonding failure criterion for O-ACS with different mandrel diameters

Mandrel diameter (m)	Maximum compressive force at failure (N)
0.0254	NA
0.0445	NA
0.0635	NA
0.0835	NA

Overall Failure Mode under Axial Compression

The failure modes under compression are compared and the summary is given in Tables 23 and 24. It can be concluded that theoretical critical buckling load is hard to reach because the yarn always fails first at relatively lower compressive load. The joint de-bonding only occurs at 22.5 and 33.5 degree braiding angle. Figure 56 illustrates the buckling failure mode over axial yarn without joint de-bonding and yarn failure. The critical buckling load is calculated by eigenvalue and nonlinear solution. Figure 57 illustrates the yarn failure mode, which occurs when the stress in the yarn exceeds the yielding point. The yarn failure mode mainly depends on the microcrimp in the axial yarns and the joint. O-ACS samples 3, 4, 5, 6, 7, and 8 under compression can be categorized as yarn failure. Figure 58 illustrates the joint de-bonding failure and subsequent buckling. What happens here is that the joint will de-bond first and buckling will occur within the new unsupported section. Even if the joint is de-bonded, the structure can still bear load until it reaches the critical buckling load of the new section.

Table 23 Summary of failure modes under compression for different braiding angles

Braiding angle (degree)	Buckling	Yarn failure force (N)	Joint de-bonding force (N)
22.5	Happened after de-bonding	No	1506 N
33.5	Happened after de-bonding	No	1770 N
45	No	2588 N	No
56.5	No	2378 N	No
67.5	No	2120 N	No

Table 24 Summary of failure modes under compression for different mandrel diameters

Mandrel diameter (m)	Buckling	Yarn failure force (N)	Joint de-bonding force (N)
0.0254	No	2571 N	No
0.0445	No	2588 N	No
0.0635	No	2560 N	No
0.0835	No	2520 N	No

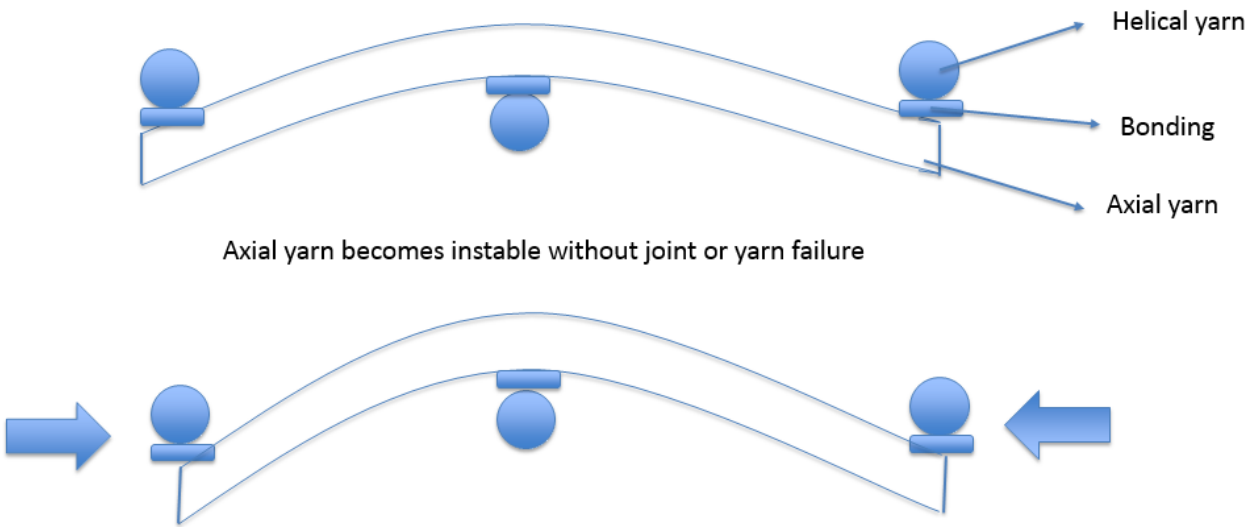

Figure 56 Illustration of buckling failure over axial yarn

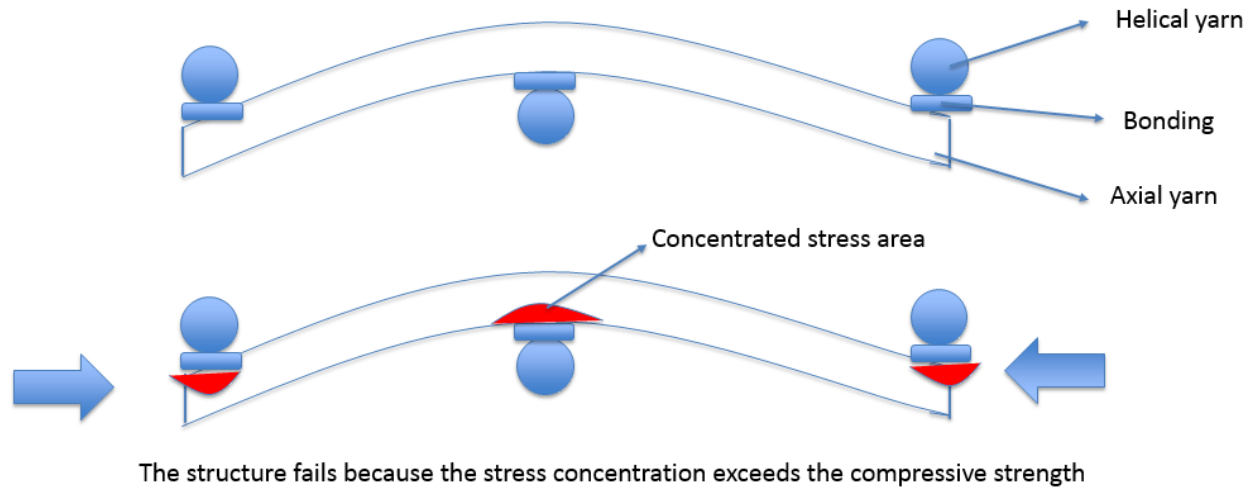

Figure 57 Illustration of yarn failure over axial yarn

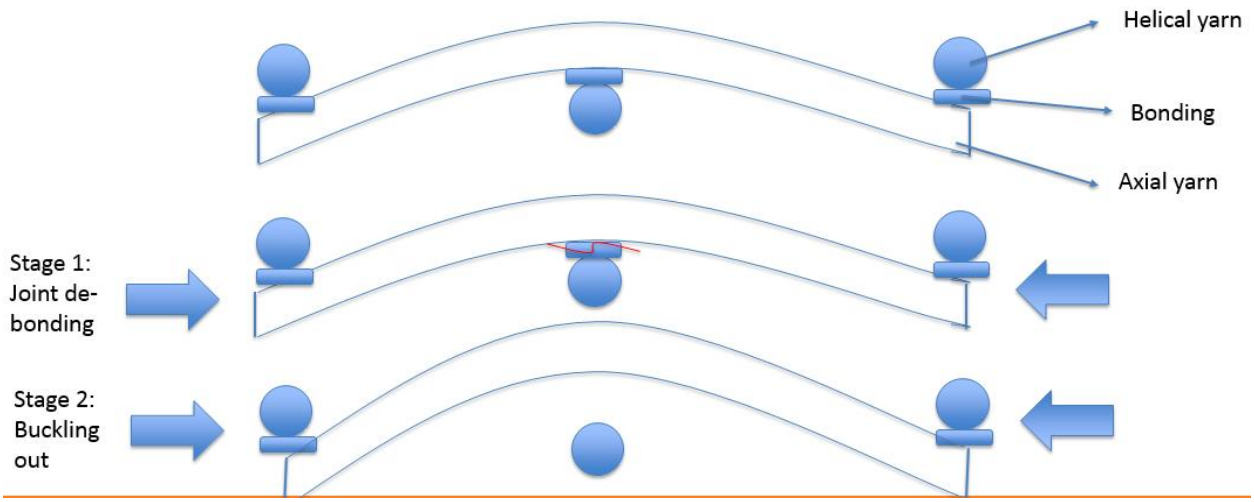

Figure 58 Illustration of combination of joint de-bonding and buckling failure over axial yarn

Axial Tension

Buckling Failure under Axial Tension

As expected, buckling failure under tension is not observed as the tensile force increases to 50000N. The deformed shape in a nonlinear solution is given in Table 25. It is shown that the axial yarn in the O-ACS tends to get straightened as the tensile force increases. There is no local instability over the axial yarn under tension.

Table 25 Deformed shape of O-ACS under tension

Braiding angle (degree)	Deformed shape	Buckling ?
22.5	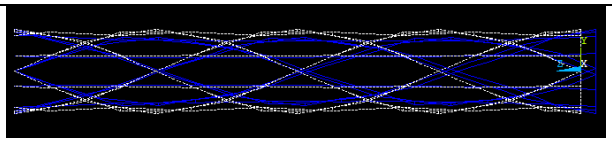	No
33.5	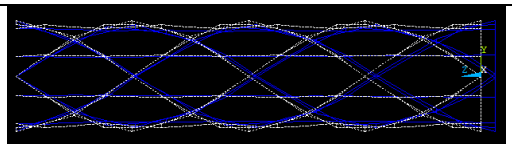	No
45	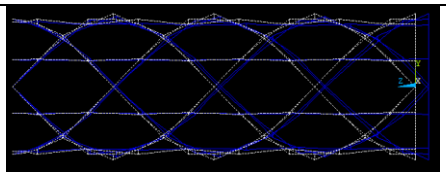	No
56.5	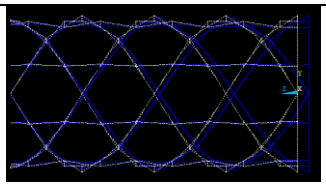	No
67.5	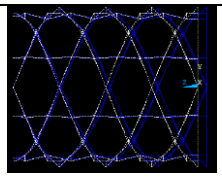	No

Yarn Failure under Tension

Maximum tensile force based on yarn failure criterion is given in Tables 26, 27 and Figure 59, and 60. The maximum tensile force increases as the braiding angle decreases. The maximum tensile force is not affected much by mandrel diameter since its variation is small.

Table 26 Maximum tensile force for the on yarn failure for different braiding angles

Braiding angle (degree)	The element with maximum stress	Maximum tensile force (N)
22.5	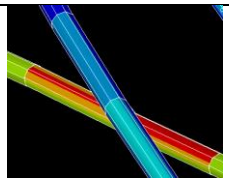	14150
33.5	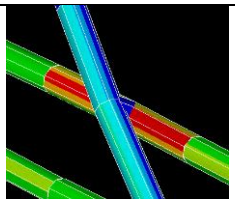	9500
45	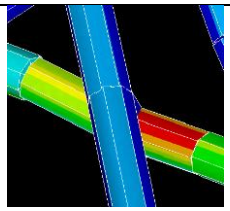	8163
56.5	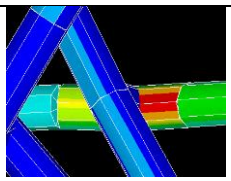	6930
67.5	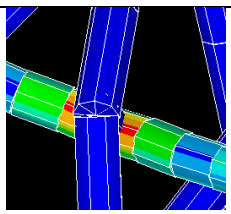	5797

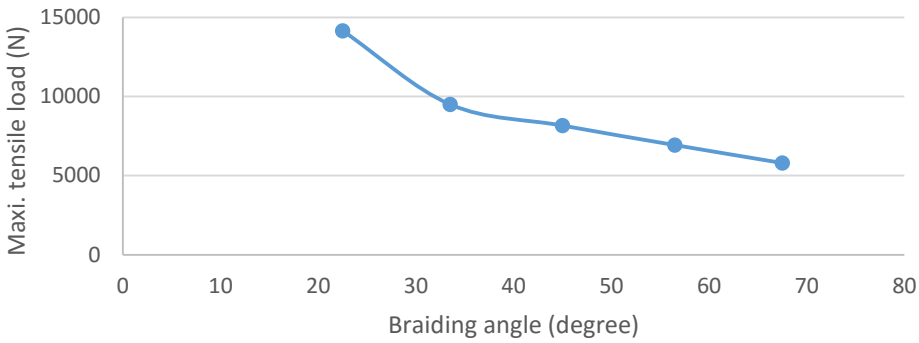

Figure 59 Maximum tensile force for the on yarn failure vs. braiding angle

Table 27 Maximum tensile force for the on yarn failure for different mandrel diameter

Mandrel diameter	The element with maximum stress	Maximum tensile force (N)
0.0254	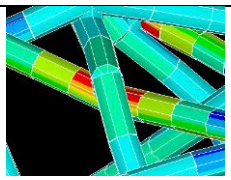	9370
0.0445	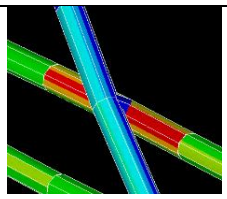	9500
0.0635	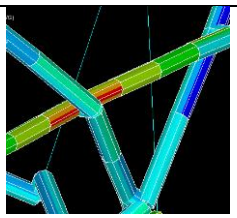	9945
0.0835	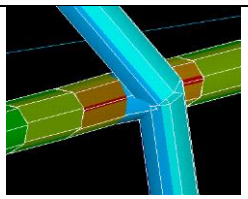	10109

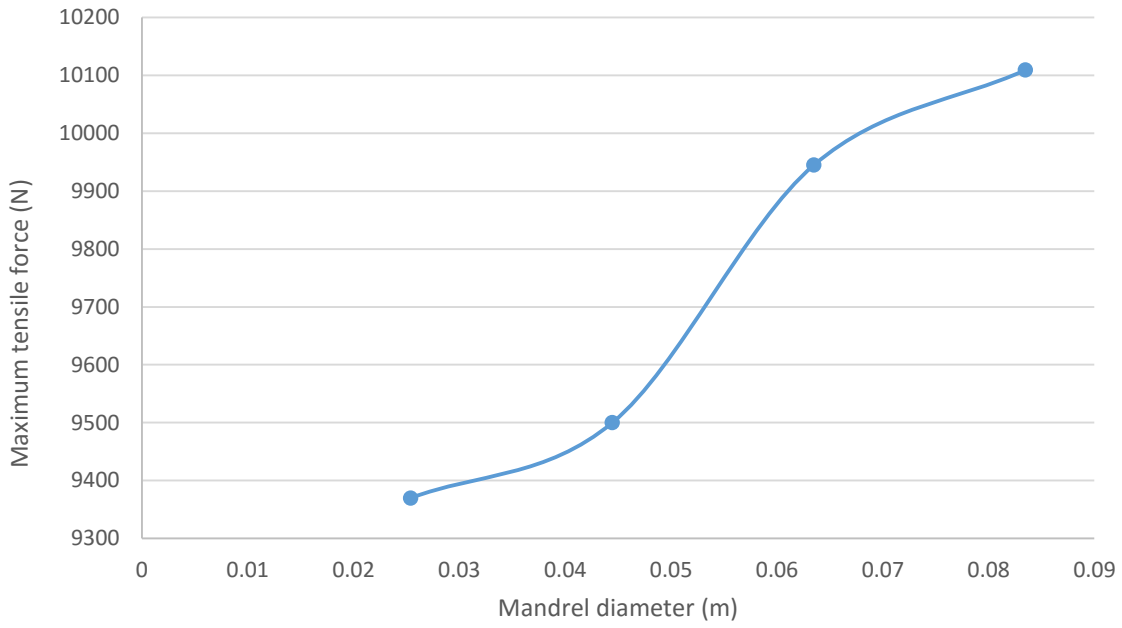

Figure 60 Maximum tensile force for the on yarn failure vs. mandrel diameter

Joint De-bonding under Tension

Joint de-bonding is not observed for all 8 models under tension condition. Even if the joint failure occurs, its delamination will not affect the tensile strength since the axial yarn can still take up tensile load as it is stretched. Therefore, joint de-bonding is not a critical issue in axial tensile loading.

Overall Failure Mode under Axial Tension

The failure mode of O-ACS under axial tension is summarized in Table 28. In conclusion, the dominating failure mode of O-ACS under axial tension is the yarn failure. The loss of stability does not occur under tension condition even though there are micro-crimps on axial yarns. The axial yarn will be stretched and continuously bear tensile load until the stress in axial yarn exceeds the yielding point. Therefore, the local buckling failure is not applicable to axial tension. During the whole tensile process, the joint has limited influence on the tensile strength since the axial yarn can still have tensile force with or without joint de-bonding.

Table 28 Summary of failure modes of O-ACS under axial tension

Braiding angle (degree)	Buckling	Yarn failure force (N)	Joint de-bonding
22.5	NA	14150 N	No
33.5	NA	9500 N	No
45	NA	8163 N	No
56.5	NA	6930 N	No
67.5	NA	5797 N	No

Mandrel diameter (m)	Buckling	Yarn failure force (N)	Joint de-bonding
0.0254	NA	9370 N	No
0.0445	NA	9500 N	No
0.0635	NA	9945 N	No
0.0835	NA	10109 N	No

Pure Bending

Buckling Failure under Pure Bending

Results for critical buckling moment under pure bending are given in Tables 29, 30 and Figures 61, and 62. Again, it must be pointed out that the buckling failure only involves the local buckling failure. It is indicated that the local buckling failure under pure bending increases as the braiding angle increases and decreases as the mandrel diameter increases.

Table 29 Critical buckling moment under pure bending for different braiding angles

Braiding angles (degrees)	Buckling shape	Critical buckling moment by eigenvalue solution (Nm)	Critical buckling moment by nonlinear solution (Nm)
22.5	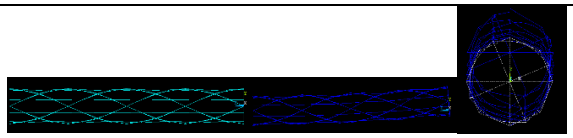	38	55
33.5	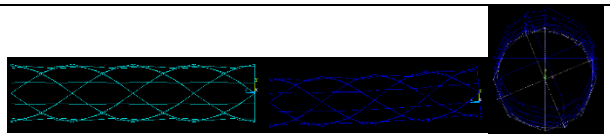	90	95
45	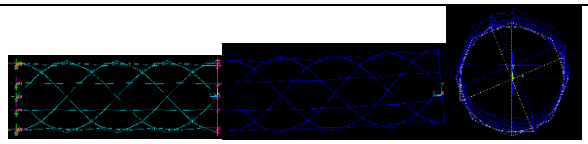	167	185
56.5	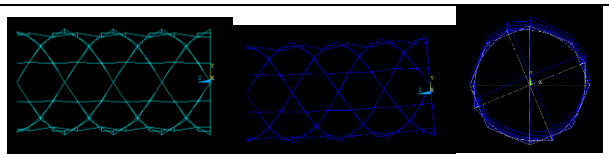	259	294
67.5	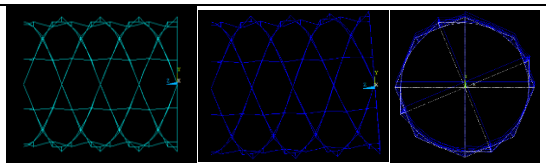	407	336

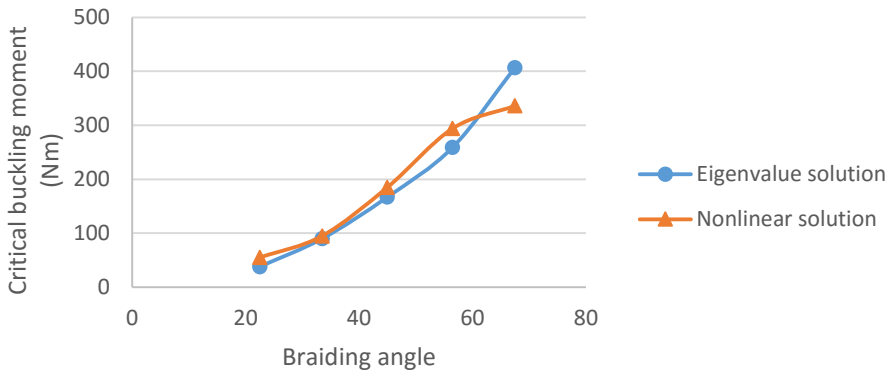

Figure 61 Critical buckling moment vs. braiding angle under pure bending

Table 30 Critical buckling moment under pure bending for different mandrel diameter

Mandrel diameter (m)	Buckling shape	Critical buckling moment by eigenvalue solution (Nm)	Critical buckling moment by nonlinear solution (Nm)
0.0254	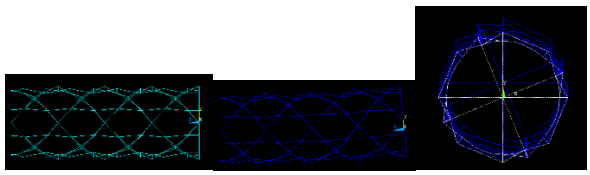	233	250
0.0445	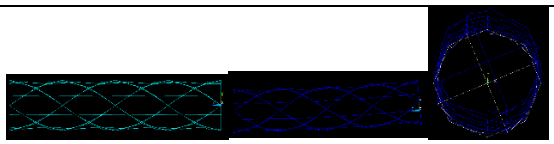	167	185
0.0635	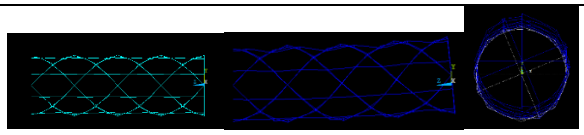	125	140
0.0835	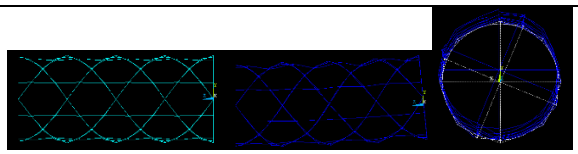	97	110

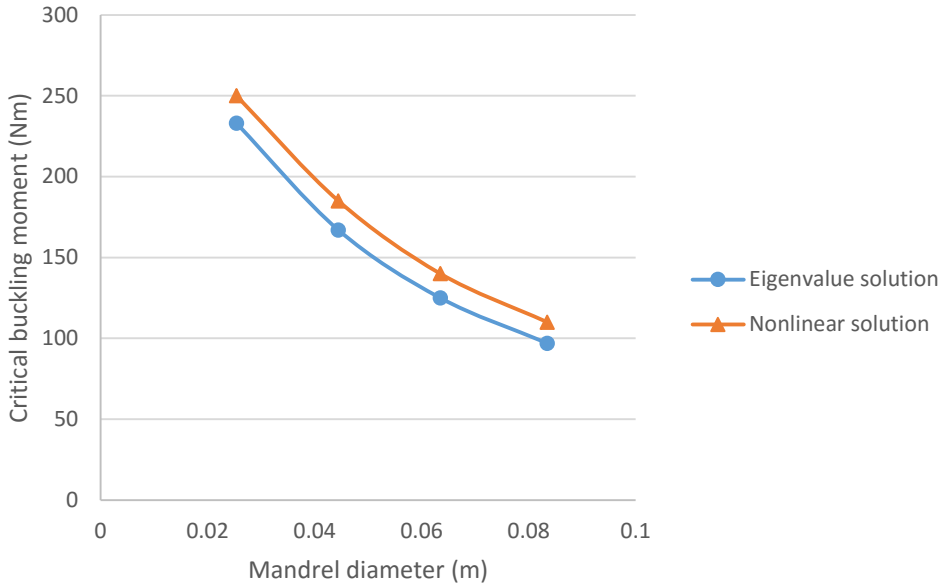

Figure 62 Critical buckling moment vs. mandrel diameter under pure bending

Yarn Failure under Pure Bending

Maximum bending moment based on yarn failure criterion are given in Tables 31, 32 and Figures 63, and 64. It is concluded that the braiding angle does not affect maximum bending strength. The maximum bending strength will increase as the mandrel diameter increases. It must be pointed out that the orientation of O-ACS is also an important issue considering the maximum bending moment. In reference to Figure 65, a is the orientation used in the simulation, b is the orientation which yields the lowest stress, and c is the orientation which has the highest stress.

Table 31 Maximum bending moment for the yarn failure for different braiding angles

Braiding angle (degree)	The element with maximum stress	Maximum bending moment (Nm)
22.5	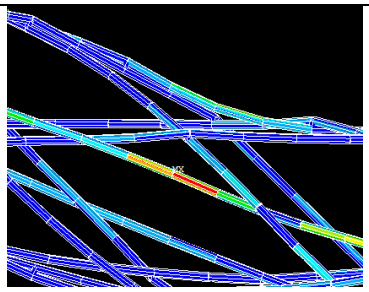	37
33.5	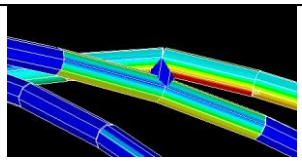	37
45	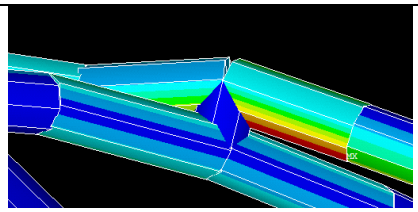	42
56.5	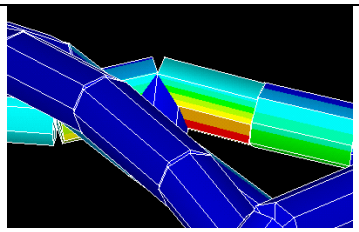	39
67.5	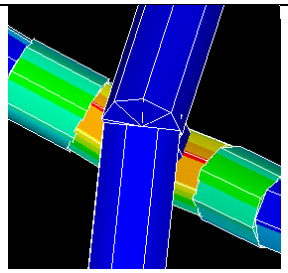	35

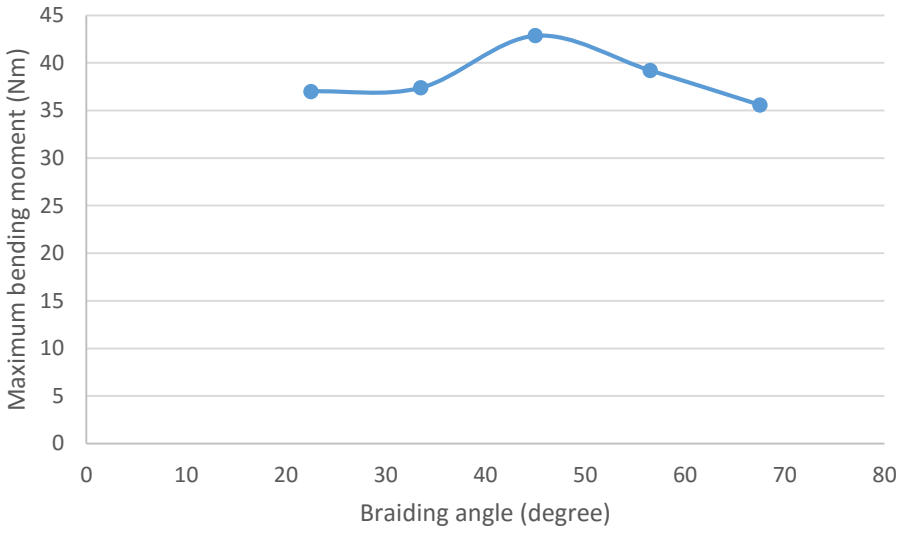

Figure 63 Maximum bending moment for the yarn failure vs. braiding angle under pure bending

Table 32 Maximum bending moment for the yarn failure for different mandrel diameters

Mandrel diameter (m)	The element with maximum stress	Maximum bending moment (Nm)
0.0254	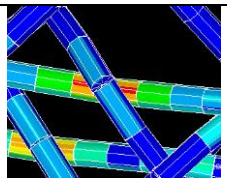	26
0.0445	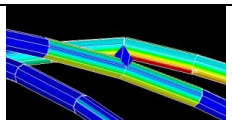	37
0.0635	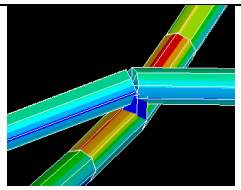	58
0.0835	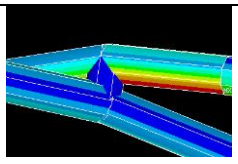	70

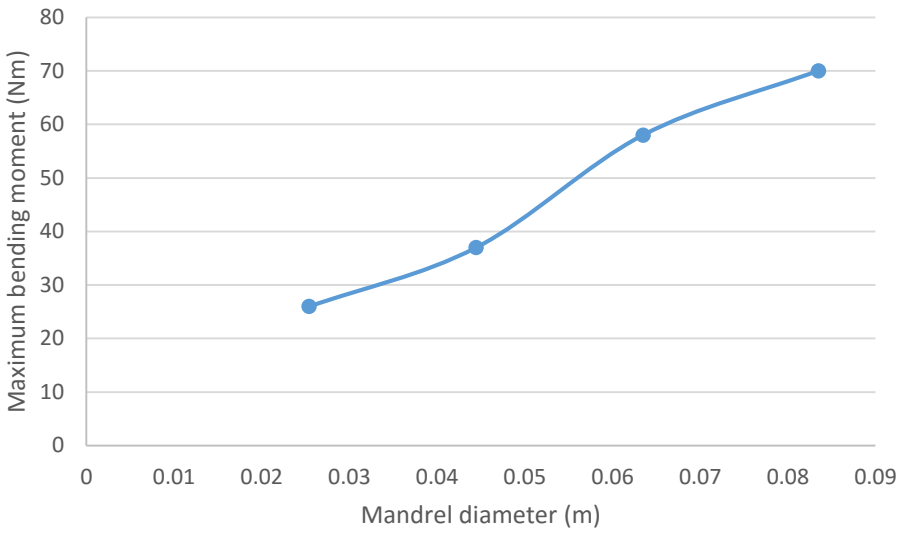

Figure 64 Maximum bending moment based on yarn failure vs. mandrel diameter under pure bending

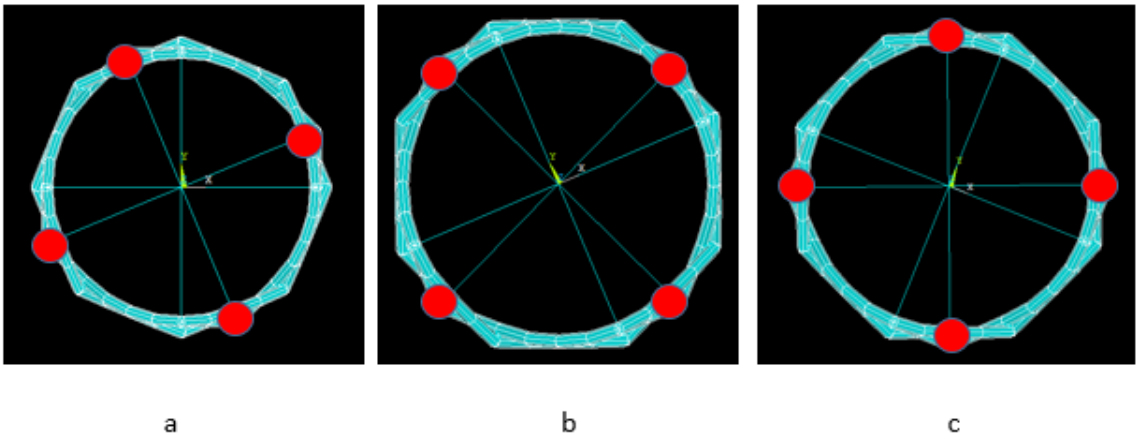

Figure 65 Different orientations of O-ACS under bending tests

Joint De-bonding under Pure Bending

Joint de-bonding is not observed for any of the O-ACS models under pure bending conditions.

Overall Failure Mode under Pure Bending

The failure mode of O-ACS under pure bending is summarized in Table 33. Yarn failure is responsible for all of the eight O-ACS models.

Table 33 Summary of failure modes of O-ACS under pure bending

Braiding angle (degree)	Buckling	Yarn failure moment (Nm)	Joint de-bonding
22.5	No	37 Nm	No
33.5	No	37 Nm	No
45	No	42 Nm	No
56.5	No	39 Nm	No
67.5	No	35 Nm	No

Mandrel diameter (m)	Buckling	Yarn failure Moment (Nm)	Joint de-bonding
0.0254	No	26 Nm	No
0.0445	No	37 Nm	No
0.0635	No	58 Nm	No
0.0835	No	70 Nm	No

Torsion

Buckling Failure under Torsion

Critical buckling torques for O-ACS are given in Tables 34, 35 and Figures 66, and 67. The critical buckling torque, unlike the critical bending moment, was a positive correlation with the braiding angle and negative correlation with the mandrel diameter. This is because the local buckling failure under torsion occurs within the span length of the helical yarns rather than the axial yarns which have smaller contribution to torsional stiffness. The higher the braiding angle, the smaller the span

length on helical yarn, which results in higher critical buckling torque. The larger the diameter of the tube, the longer the span length on helical yarn, which yields lower critical buckling torque.

Table 34 Critical buckling torque under torsion for different braiding angles

Braiding angle (degree)	Buckling shape	Critical buckling torque by eigenvalue solution (Nm)	Critical buckling torque by nonlinear solution (Nm)
22.5	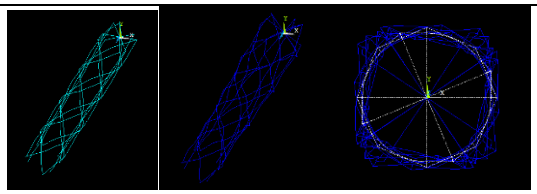	36	47
33.5	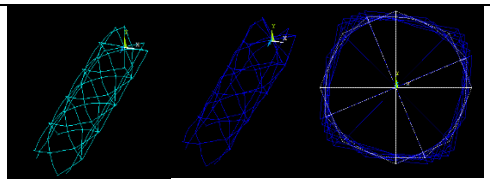	101	140
45	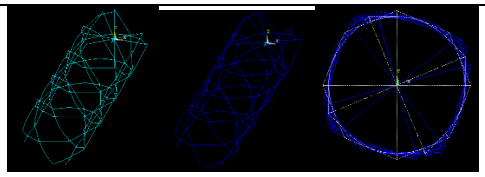	206	288
56.5	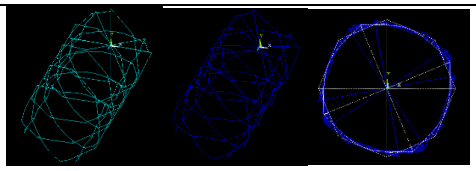	359	434
67.5	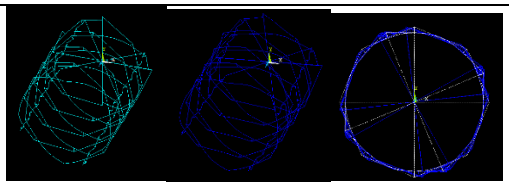	579	637

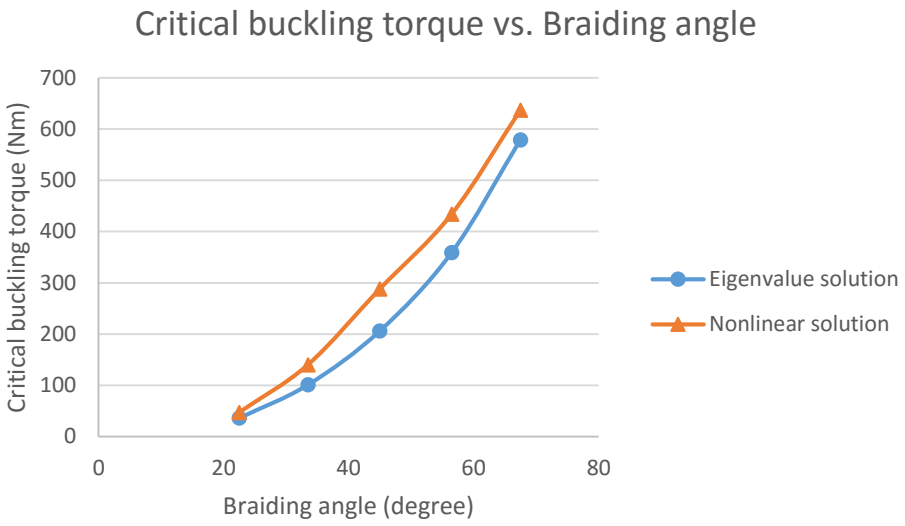

Figure 66 Critical buckling torque vs. braiding angle under torsion

Table 35 Critical buckling torque under torsion for different mandrel diameters

Mandrel diameter (m)	Buckling shape	Critical buckling torque by eigenvalue solution (Nm)	Critical buckling torque by nonlinear solution (Nm)
0.0254	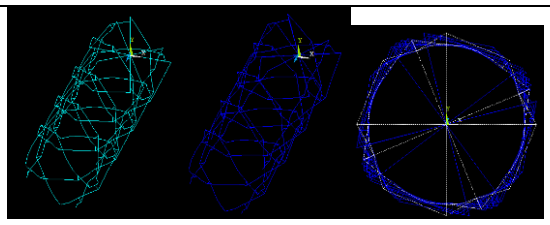	303	355

0.0445	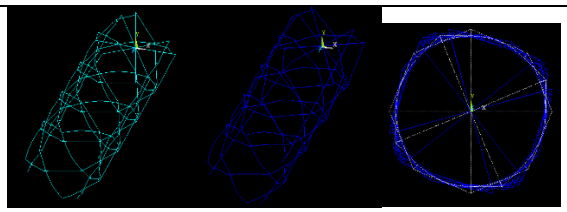	206	240
0.0635	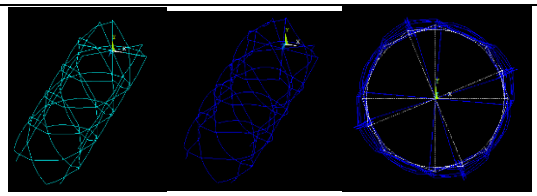	153	189
0.0835	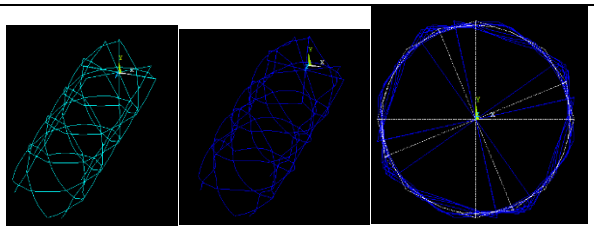	121	144

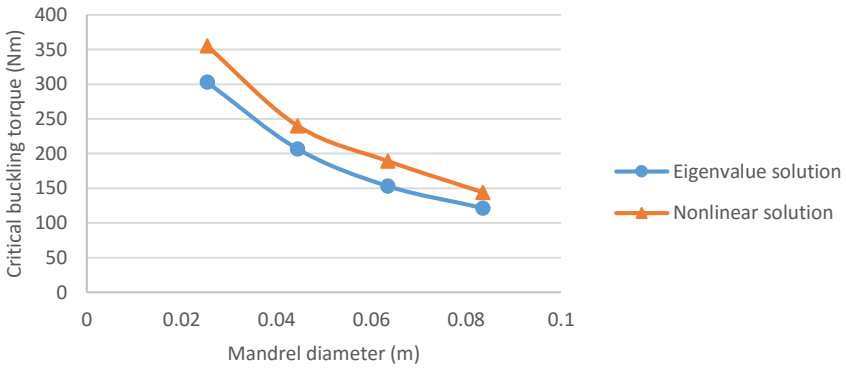

Figure 67 Critical buckling torque vs. mandrel diameter under torsion

Yarn Failure under Torsion

Results of maximum torque of O-ACS based on yarn failure are given in Tables 36, 37 and Figures 68, and 69. The maximum torque shows a positive correlation with both the braiding angle and mandrel diameter.

Table 36 Maximum torque based on the yarn failure for different braiding angles

Braiding angle (degree)	The element with maximum stress	Maximum torque (Nm)
22.5	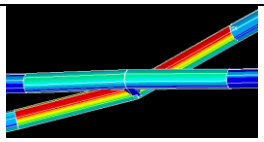	34
33.5	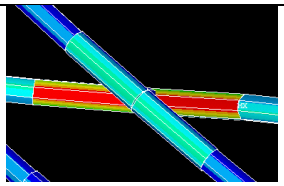	58
45	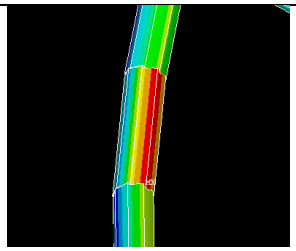	71
56.5	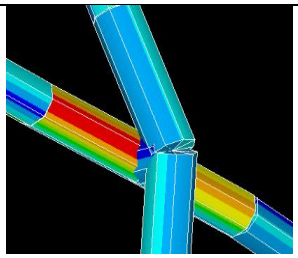	92
67.5	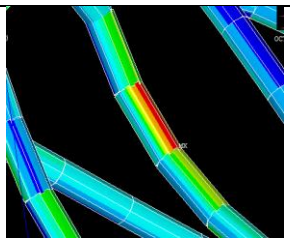	99

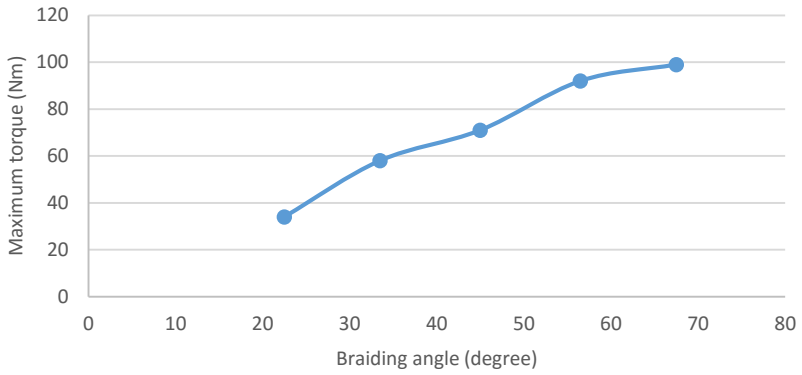

Figure 68 Maximum torque based on yarn failure vs. braiding angle under torsion

Table 37 Maximum torque based on the yarn failure for different mandrel diameters

Mandrel diameter (m)	The element with maximum stress	Maximum torque (Nm)
0.0254	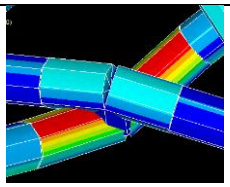	55
0.0445	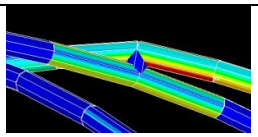	71
0.0635	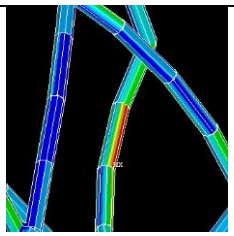	80
0.0835	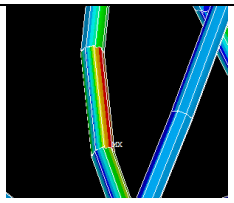	93

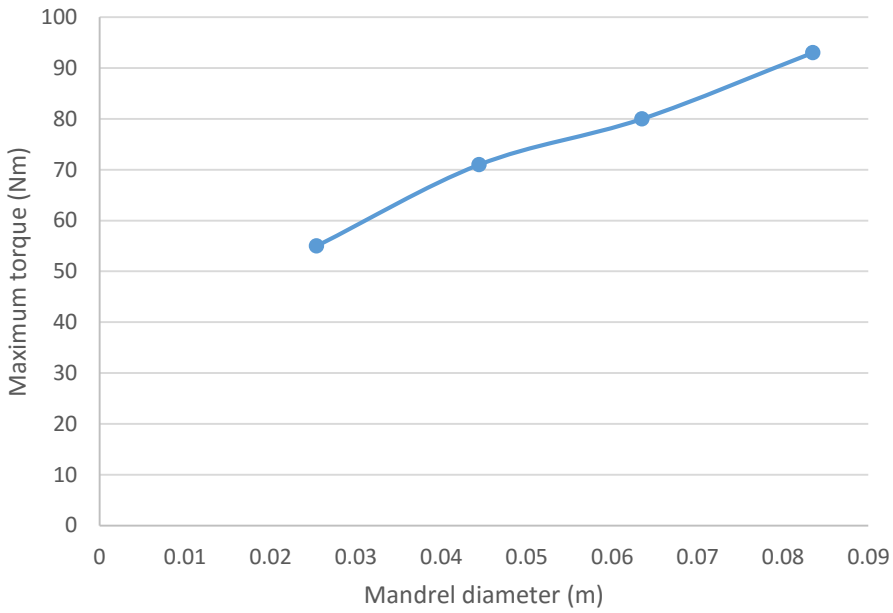

Figure 69 Maximum torque based on yarn failure vs. mandrel diameter under torsion

Joint De-bonding under Torsion

The data obtained from FEA are given in Table 38 for joint de-bonding under tension. In the analysis, the joint de-bonding failure is only observed in the O-ACS model with 22.5 degree braiding angle. This can fortify the conclusion that the joint de-bonding mainly depends on the braiding angle. If the braiding angle is larger than 45 degree, the force transferred on the joint will not be high enough to break the joint.

Table 38 Maximum torque at joint de-bonding

Braiding angle (degree)	Maximum torque at joint de-bonding (Nm)
22.5	30
33.5	No
45	No
56.5	No
67.5	No

Mandrel diameter (m)	Maximum torque at joint de-bonding (Nm)
0.0254	No
0.0445	No
0.0635	No
0.0835	No

Overall Failure Mode under Torsion

The summary of failure mode of O-ACS under torsion is given in Table 39. The yarn failure mode accounts for all the O-ACS models except the model with 22.5 degree braiding angle.

Table 39 Summary of failure modes of O-ACS under pure bending

Braiding angle (degree)	Buckling	Yarn failure torque (Nm)	Joint de-bonding torque (Nm)

22.5	Happened after joint failure	No	30 Nm
33.5	No	58 Nm	No
45	No	71 Nm	No
56.5	No	92 Nm	No
67.5	No	99 Nm	No

Mandrel diameter (m)	Buckling	Yarn failure torque (Nm)	Joint de-bonding
0.0254	No	55 Nm	No
0.0445	No	71 Nm	No
0.0635	No	80 Nm	No
0.0835	No	93 Nm	No

Validation by Compression Tests of O-ACS

The compressive strength obtained by the model is validated by experiments. In the experiments, five different O-ACS with 22.5, 33.5, 45, 56.4, and 67.5 braiding angles are manufactured in 4x4x4 configuration. Each sample has 4 specimens for testing. The yarn consists of 60K carbon fiber as core and a 200D Vectran as 2x2x4 true triaxial jacket. The O-ACS samples are potted in pipe nipples using epoxy. The samples are shown in Figure 70. Experimental data of the compression tests for different braiding angles are given in Table 40. The corresponding compressive strength for each O-ACS is extracted from the analysis above and compared with the experimental data in Figure 71, which indicates a good agreement between compressive failure model data and

experimental data. The experimental data of compressive strength divided by linear density of O-ACS is also calculated in Figure 72. The failure mode of O-ACS with 22.5 and 33.5 degree braiding angles are observed to be buckling failure triggered by joint de-bonding, whereas O-ACS with 45, 56.5, and 67.5 degrees have the yarn failure mode (Figure 73). This also coincides well with the failure mode predicted by the finite element analysis introduced above.

Figure 70 O-ACS samples for compression tests

Table 40 Experimental data for compression tests

Braiding angle (degree)	specimen1	specimen2	specimen3	specimen4	Average (N)	SD

22.5	1648.1	1884.3	1534.2	1847.2	1728.4	165.9
33.5	1734.8	1622.7	1902.2	1890.2	1787.4	133.7
45	1889.5	2339.5	2356.6	2488.8	2268.6	261.3
56.5	1840.8	1976.6	1895.1	1999.3	1927.9	73.3
67.5	1806.4	1749.5	1766.3	1900.3	1805.6	67.4

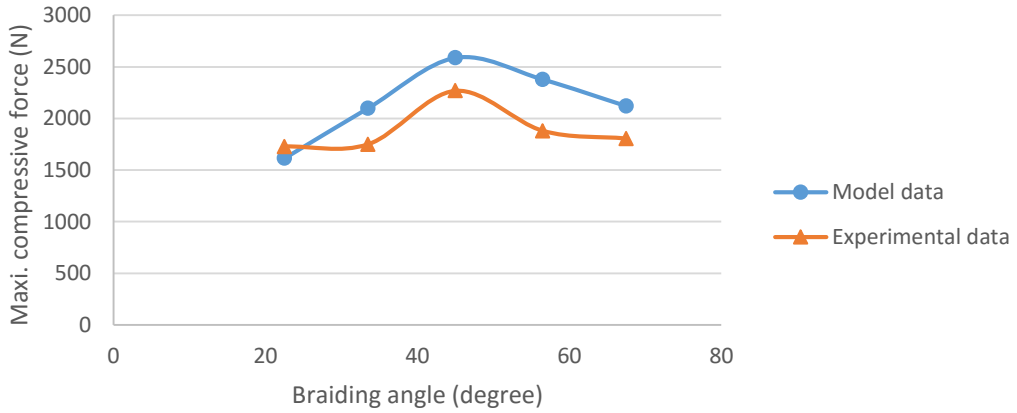

Figure 71 Comparison between experimental data and model data

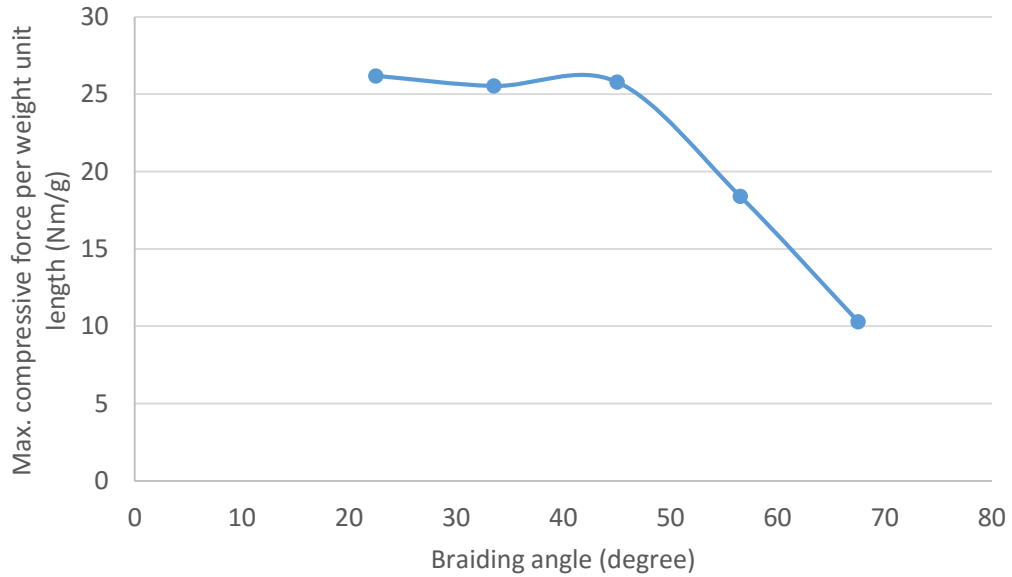

Figure 72 Compressive force per weight unit length vs. braiding angle

Figure 73 Buckling failure triggered by joint de-bonding (left) and yarn failure (right)

Global Buckling of O-ACS

Global buckling behavior has been studied using the finite element analysis procedure. 4x4x4 O-ACS models with different braiding angles are generated in Ansys. The cord-preg is 48K core with TT 200D nylon jacket. In this case, the relationship between the critical buckling load under compression with respect to the total length of O-ACS has been investigated to distinguish the local buckling failure and global buckling failure. The FEA results are given in Figure 74. The value right to the slash means span length and the value left to the slash means the length between joints. It is indicated that the structures with 22.5 and 33.75 braiding angles have a plateau if the length is less than about 2m. This reflects that the plateau area is actually governed by local buckling because local buckling does not depend on the total length of the sample. However, as the length is gradually increasing, global buckling starts to take place. For the structures with 45, 57, 67.5 degrees braiding angles, the plateau is not clearly shown in the graph. This means that the

critical buckling load required for local buckling is much higher than the critical buckling load for global buckling because the span lengths are very small. Therefore, it is the global buckling that dominates the structure with relatively small span length. Figure 75 illustrates the local buckling failure and global buckling failure of O-ACS.

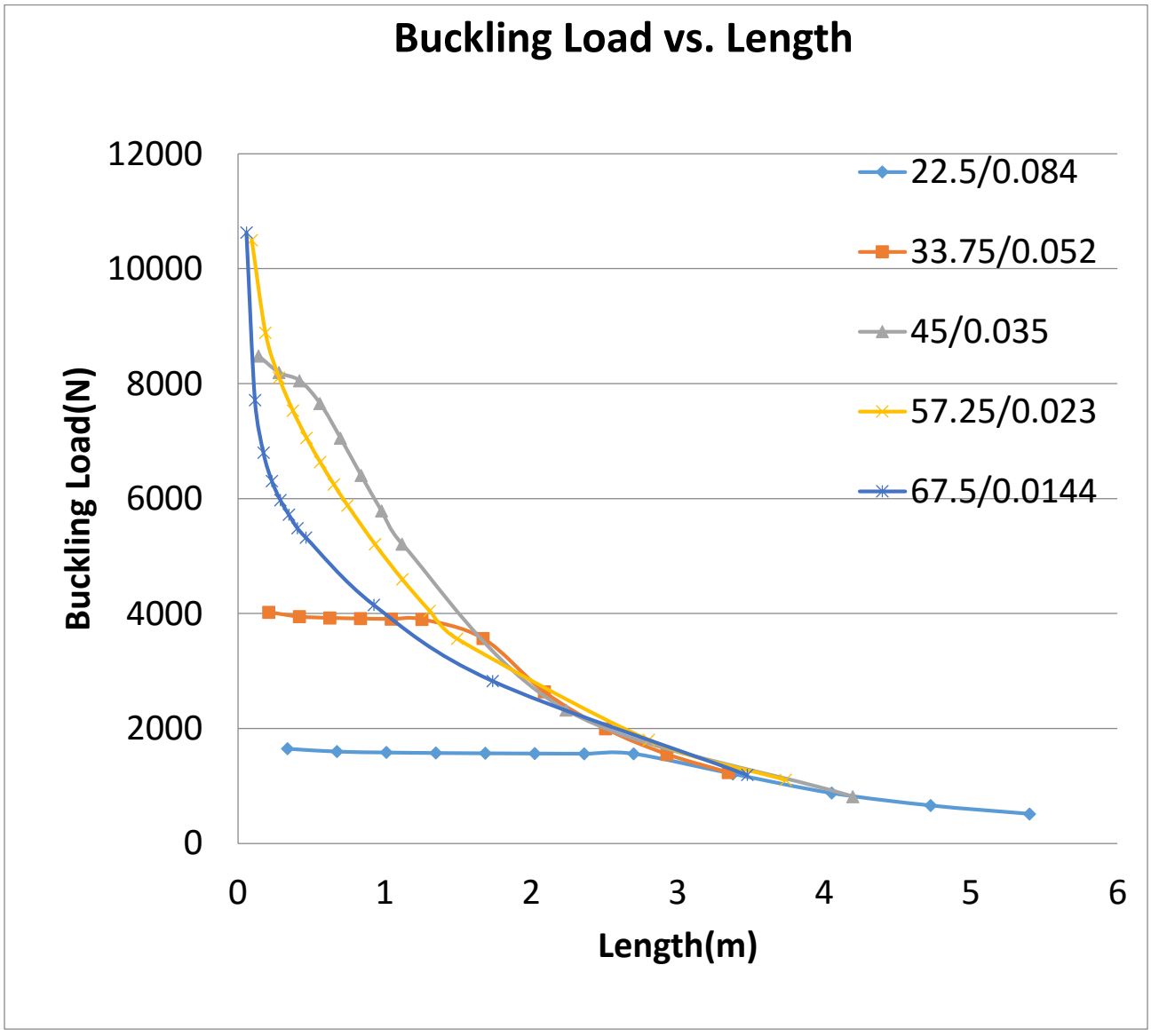

Figure 74 Critical buckling load vs. total length for O-ACS with various braiding angles

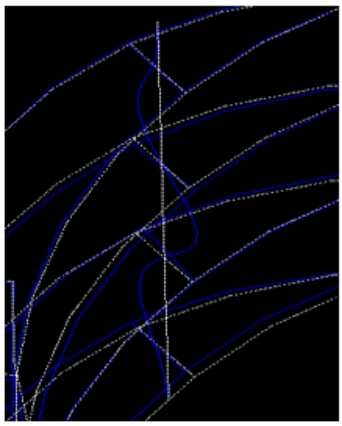

Local Buckling
Buckling of individual member
No significant lateral displacement

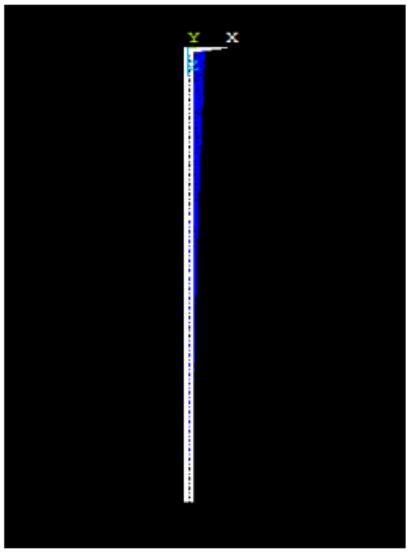

Global Buckling
Significant lateral displacement

Figure 75 Illustration of local buckling and global buckling

The finite element model can be used for generating the design chart on the strength of O-ACS as shown in Figure 76. Figure 76 shows the critical buckling load of the 4x4x4 O-ACS under compression in terms of various braiding angles and mandrel diameter. The design chart tells us the anticipated load to buckle the O-ACS with certain braiding angle and diameter.

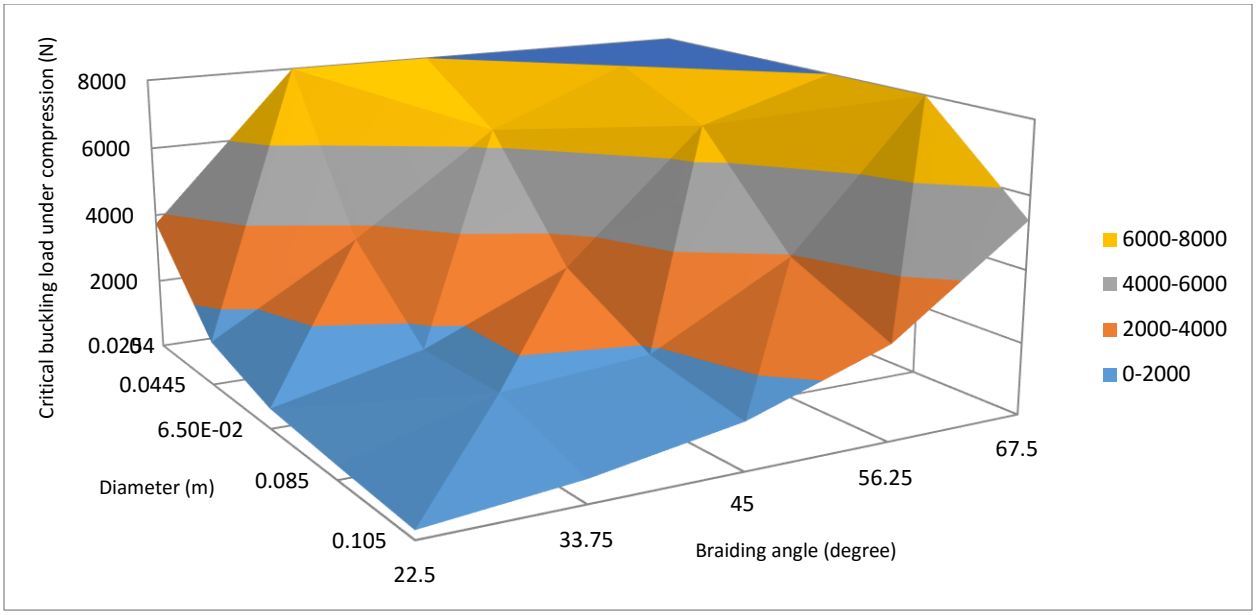

Figure 76 Design chart on critical buckling load of the O-ACS with different braiding angles and diameters

Conclusions

A method of examining the failure strength of O-ACS is proposed. The method is based on the failure modes including local buckling, yarn yielding and joint de-bonding. A finite element model generation program is written in Matlab to efficiently generate finite element models of O-ACS with different parameters. Based on the results, the joint de-bonding failure only occurs in the structure with relatively small braiding angle. The yarn failure mode is the dominating failure mode which can be regarded as the primary failure mode. The method has been partially validated by the experimental data of the compressive tests. This model can be applied to analyze the failure behavior of O-ACS under any loading conditions.

References

Agarwal, B. D. and Broutman, L. J. (1990). “Analysis and Performance of Fiber Composites”, 2nd ed. John Wiley & Sons, Inc., New York, NY.

Azzi, V. D. and Tsai, S. W. (1965). “Anisotropic strength of composites”, in Proceedings of the Society for Experimental Stress Analysis, XXII(2), 283–288.

Benveniste Y. (1987). “A new approach to the application of Mori-Tanaka’s theory in composite materials”, Mechanics of Materials, 6, 147-157.

Bogetti, T. A., Hoppel, C. P. R., Harik, V. M., Newill, J. F., and Burns, B. P. (2004). “Predicting the nonlinear response and progressive failure of composite laminates”, Composites Science and Technology, 64(3–4), 329–342.

Bogetti, T. A., Hoppel, C. P. R., Harik, V. M., Newill, J. F., and Burns, B. P. (2004). “Predicting the nonlinear response and progressive failure of composite laminates: Correlation with experimental results”, Composites Science and Technology, 64(3–4), 477–485.

Branscomb, D. (2007). “A Machine Vision and Sensing System for Braid Defect Detection, Diagnosis, and Prevention during Manufacturing”, Auburn: Auburn University.

Branscomb, D. (2012). “Minimal Weight Composites Utilizing Advanced Manufacturing Techniques. Dissertation”, Auburn: Auburn University.

Branscomb, D.J., Broughton, R.M., Beale, D.G. (2013). “Robust pre-impregnated yarn for manufacturing textile composites”, Pub. No.: US20130302604 A1.

Broughton, R.M., Branscomb, D.J., Beale, D.G. (2015). “Minimal weight composites using open structure”, Pub. No.: US20150056449 A1.

Chamis CC. (1989). “Mechanics of composite materials: past, present, and future”, J Compos Technol Res ASTM; 11:3–14.

Chen, H. J. and Tsai, S. W. (1996). “Analysis and optimum design of composite grid structures”, Journal of Composite Materials, 30(4), 503–534.

Gibson, Ronald F. (2011). “Principles of Composite Material Mechanics”, CRC Press, 3th edition, Boca Raton, FL

Greszczuk, L. B. (1974). “Microbuckling of lamina-reinforced composites”, in Berg, C. A., McGarry, F. J., and Elliott, S. Y. eds., Composite Materials: Testing and Design (Third Conference), ASTM STP 546, pp. 5–29. American Society for Testing and Materials, Philadelphia, PA.

Gurley, A. (2014). “Design and Analysis of Optimal Braided Composite Lattice Structures”, Auburn: Auburn University.

Gurley, A., Beale, D., Broughton, R., and Branscomb, D. (2015). “The Design of Optimal Lattice Structures Manufactured by Maypole Braiding”, J. Mech. Des. 137(10).

Halpin JC., Kardos JL. (1976). “The Halpin-Tsai equations: A review”, Polymer Engineering and Sicence, May, Vol.16, No.5.

Hashin Z., Rosen BW. (1964). "The elastic moduli of fiber reinforced materials", Journal of Applied Mechanics, Trans ASME, 31, 223-232.

Higdon, A., Ohlsen, E. H., Stiles, W. B., Weese, J. A., and Riley, W. F. (1976). "Mechanics of Materials", 3rd ed. John Wiley & Sons, New York, NY.

Hill R. (1965). "Theory of mechanical properties of fibre-strengthen materials-III. Self-consistent model", Journal of Mechanics and Physics of Solids; 13: 189-198

Hill, R. (1948). "A theory of the yielding and plastic flow of anisotropic metals", in Proceedings of the Royal Society of London, Series A, 193, 281–297.

Huang ZM. (2001). "Micromechanical prediction of ultimate strength of transversely isotropic fibrous composites", International Journal of Solids and Structures 38, 4147-4172.

Huang ZM. (2001). "Simulation of the mechanical properties of fibrous composites by the bridging micromechanics model", Composites: Part A 32,143–172.

Hull, D. (1981). "An Introduction to Composite Materials", Cambridge University Press, Cambridge, MA.

Huybrechts, S. and Tsai, S. W. (1996). "Analysis and behavior of grid structures", Composites Science and Technology, 56(9), 1001–1015.

Jenkins, C. F. (1920). "Report on materials of construction used in aircraft and aircraft engines", Great Britain Aeronautical Research Council, London, UK.

Keller, J.B. (1960). "The shape of the strongest column", Arch. Rational Mech. and Anal. 5, 275-285

Kelly, A. and Davies, G. J. (1965). "The principles of the fibre reinforcement of metals", Metallurgical Review, 10, 1–77.

Kies, J. A. (1962). "Maximum strains in the resin of fiber glass composites", U.S. Naval Research Laboratory Report No. 5752.

Kothari, N. (2014). "Mechanical Characterization of the Braided Composite Yarn and Bond Strength Evaluation of the Joints of the Open-Architecture Composite Structure (O-ACS)", Auburn: Auburn University.

Li S. (2008). "Boundary conditions for unit cells from periodic microstructures and their implications", Composites Science and Technology 68, 1962–1974.

Liu, K. S. and Tsai, S. W. (1998). "A progressive quadratic failure criterion for a laminate", Composites Science and Technology, 58(7), 1023–1032.

Mori T., Tanaka K. (1973). "Average stress in matrix and average elastic energy of materials with misfitting inclusions", Acta Mettall. 21, 571-574.

Ning Hu, (2012). "Composites and Their Properties", ISBN 978-953-51-0711-8, Published: August 22,

Pister, K. S. and Dong, S. B. (1959). "Elastic bending of layered plates", in Proceedings of the American Society of Civil Engineers, 85, EM4, 1–10.

Polya, G. and Szego, G. (1962). “Isoperimetric Inequalities in mathematical physics”, Princeton University Press, Moscow: Fizmatgiz

Rehfield, L. W. (1999). “A brief history of analysis methodology for grid-stiffened geodesic composite structures”, Proc. 44th International SAMPE Symposium, CD-ROM.

Reissner, E. and Stavsky, Y. (1961). “Bending and stretching of certain types of heterogeneous aeolotropic elastic plates”, Journal of Applied Mechanics, 28, 402–408.

Reuss, A. (1929). “Berechnung der Fließgrenze von Mischkristallen auf Grund der Plastizitätsbedingung für Einkristalle”, Zeitschrift für Angewandte Mathematik und Mechanik 9: 49–58.

Rosen, B. W. (1965). “Mechanics of composite strengthening. Fiber Composite Materials”, American Society for Metals, Metals Park, OH.

Rozvany, G. I. (2009). “A critical review of established methods of structural topology optimization”, Structural Multidisciplinary Optimization, 217-237.

Schuerch, H. (1966). “Prediction of compressive strength in uniaxial boron fiber metal matrix composites”, AIAA Journal, 4, 102–106.

Smith, C. B. (1953). “Some new types of orthotropic plates laminated of orthotropic material”, Journal of Applied Mechanics, 20, 286–288.

Stavsky, Y. (1964). “On the general theory of heterogeneous aeolotropic plates”, Aeronautical Quarterly, 15, 29–38.

Tsai, S.W. and Wu, E.M. (1971). “A general theory of strength for anisotropic materials”, Journal of Composite Materials, 5, 58–80.

Voigt, W. (1889). “Ueber die Beziehung zwischen den beiden Elasticitätsconstanten isotroper Körper”, Annalen der Physik 274: 573–587.

Waddoups, M. E. (1967). “Advanced composite material mechanics for the design and stress analyst. General Dynamics”, Fort Worth Division Report FZM-4763, Fort Worth, TX.

Zinoviev, P. A., Lebedeva, O. V., and Tairova, L. R. (2002). “Coupled analysis of experimental and theoretical results of the deformation and failure of laminated composites under a plane state of stress”, Composites Science and Technology, 62(12–13), 1711–1723.

Zinoviev, P., Grigoriev, S. V., Lebedeva, O. V., and Tairova, L. R. (1998). “Strength of multilayered composites under plane stress state”, Composites Science and Technology, 58(7), 1209–1224.

Appendices

Generation of the geometry of the cord-preg in Vpython

```
import matplotlib as mpl

from mpl_toolkits.mplot3d import Axes3D

import numpy as np

import matplotlib.pyplot as plt

from visual import *

from Tkinter import *

# main code

class Coordinates():

    def
__init__(self,theta,n,counterclockwise_location,clockwise_location,axial_location,R_axials,R_core,R_bra
iders):

        self.theta =np.radians(theta)

        self.n = n


        self.discrete = 8  # number of discretization per horn gear, has to be 2**i

        self.counterclockwise_location = np.array(counterclockwise_location)

        self.clockwise_location = np.array(clockwise_location)

        self.axial_location = np.array(axial_location)


        self.t = np.linspace(0, 2*np.pi, self.n*self.discrete+1)

        self.t_c = np.linspace(0, 2*np.pi+2*np.pi/self.n, self.n*self.discrete+1+self.discrete)

        self.t_cc = np.linspace(np.pi/self.n, 2*np.pi+np.pi/self.n, self.n*self.discrete+1)


        self.step = np.linspace(0, 2*np.pi, self.n*10+1, retstep=True)[1]

        self.R_axials = np.array(R_axials)

        self.R_axials_reverse = self.R_axials[::-1]

        self.R_core = R_core
```

```
self.R_braiders = R_braiders
self.Rt = 2*self.R_braiders+self.R_core
self.L = np.pi*2*self.Rt / np.tan(self.theta)

self.number_cc = len(self.counterclockwise_location)
self.number_c = len(self.clockwise_location)
self.number_a = len(self.axial_location)




self.x_cc = np.zeros(shape=(self.n,len(self.t_cc)))
self.y_cc = np.zeros(shape=(self.n,len(self.t_cc)))
self.z_cc = np.zeros(shape=(self.n,len(self.t_cc)))

self.x_c = np.zeros(shape=(self.n,len(self.t_c)))
self.y_c = np.zeros(shape=(self.n,len(self.t_c)))
self.z_c = np.zeros(shape=(self.n,len(self.t_c)))

self.x_a = np.zeros(shape=(self.n,len(self.t)))
self.y_a = np.zeros(shape=(self.n,len(self.t)))
self.z_a = np.zeros(shape=(self.n,len(self.t)))




# clockwise (0~(2pi))
for k in range(self.n): # number of braiders
   for i in range(self.number_a): # axial location
      for j in range(self.discrete):
         if self.clockwise_location[k] == 1:
```

```
                if np.cos(self.n*0.5*(-self.t_c[i*self.discrete+j]+2*k*np.pi/self.n)+np.pi/2) <= 0:

                    self.x_c[k][i*self.discrete+j] = (((-(2*self.R_braiders*(1-
inputs.axial_crimp)+2*permutation(self.R_axials,k)[i])*np.cos(self.n*0.5*(-
self.t_c[i*self.discrete+j]+2*k*np.pi/self.n)+np.pi/2)+self.R_braiders+self.R_core)*np.cos(-
self.t_c[i*self.discrete+j]+2*k*np.pi/self.n+np.pi/self.n)))

                    self.y_c[k][i*self.discrete+j] = ((-(-(2*self.R_braiders*(1-
inputs.axial_crimp)+2*permutation(self.R_axials,k)[i])*np.cos(self.n*0.5*(-
self.t_c[i*self.discrete+j]+2*k*np.pi/self.n)+np.pi/2)+self.R_braiders+self.R_core)*np.sin(-
self.t_c[i*self.discrete+j]+2*k*np.pi/self.n+np.pi/self.n)))

                    self.z_c[k][i*self.discrete+j] = ((self.L*self.t_c[i*self.discrete+j]/(2*np.pi)))

                else:

                    self.x_c[k][i*self.discrete+j] = (((self.R_braiders+self.R_core)*np.cos(-
self.t_c[i*self.discrete+j]+2*k*np.pi/self.n+np.pi/self.n)))

                    self.y_c[k][i*self.discrete+j] = ((-(self.R_braiders+self.R_core)*np.sin(-
self.t_c[i*self.discrete+j]+2*k*np.pi/self.n+np.pi/self.n)))

                    self.z_c[k][i*self.discrete+j] = ((self.L*self.t_c[i*self.discrete+j]/(2*np.pi)))

        # clockwise (1 more interval) (2pi~(2pi+2pi/n))

        for k in range(self.n): # number of braiders

            for j in range(self.discrete):

                if self.clockwise_location[k] == 1:

                    if np.cos(self.n*0.5*(-self.t_c[(self.number_a)*self.discrete+j]+2*k*np.pi/self.n)+np.pi/2) <=
0:

                        self.x_c[k][(self.number_a)*self.discrete+j] = (((-(2*self.R_braiders*(1-
inputs.axial_crimp)+2*permutation(self.R_axials,k)[0])*np.cos(self.n*0.5*(-
self.t_c[(self.number_a)*self.discrete+j]+2*k*np.pi/self.n)+np.pi/2)+self.R_braiders+self.R_core)*np.cos
(-self.t_c[(self.number_a)*self.discrete+j]+2*k*np.pi/self.n+np.pi/self.n)))

                        self.y_c[k][(self.number_a)*self.discrete+j] = ((-(-(2*self.R_braiders*(1-
inputs.axial_crimp)+2*permutation(self.R_axials,k)[0])*np.cos(self.n*0.5*(-
self.t_c[(self.number_a)*self.discrete+j]+2*k*np.pi/self.n)+np.pi/2)+self.R_braiders+self.R_core)*np.sin(
-self.t_c[(self.number_a)*self.discrete+j]+2*k*np.pi/self.n+np.pi/self.n)))

                        self.z_c[k][(self.number_a)*self.discrete+j] =
((self.L*self.t_c[(self.number_a)*self.discrete+j]/(2*np.pi)))

                    else:

                        self.x_c[k][(self.number_a)*self.discrete+j] = ((self.R_braiders+self.R_core)*np.cos(-
self.t_c[(self.number_a)*self.discrete+j]+2*k*np.pi/self.n+np.pi/self.n))
```

```
                self.y_c[k][(self.number_a)*self.discrete+j] = ((-(self.R_braiders+self.R_core)*np.sin(-
self.t_c[(self.number_a)*self.discrete+j]+2*k*np.pi/self.n+np.pi/self.n)))

                self.z_c[k][(self.number_a)*self.discrete+j] =
((self.L*self.t_c[(self.number_a)*self.discrete+j]/(2*np.pi)))

    # counterclockwise  (2pi/n~(2pi+2pi/n))

    for k in range(self.n):

      for i in range(self.number_a):

        for j in range(self.discrete):

          if self.counterclockwise_location[k] == 1:

            if np.cos(self.n*0.5*(-(self.t[i*self.discrete+j]+np.pi/self.n)+2*k*np.pi/self.n)) >= 0:

              self.x_cc[k][i*self.discrete+j] = ((((2*self.R_braiders*(1-
inputs.axial_crimp)+2*permutation(self.R_axials_reverse,k)[i])*np.cos(self.n*0.5*(-
(self.t[i*self.discrete+j]+np.pi/self.n)+2*k*np.pi/self.n))+self.R_braiders+self.R_core)*np.cos(-
(self.t[i*self.discrete+j]+np.pi/self.n)+2*k*np.pi/self.n)))

              self.y_cc[k][i*self.discrete+j] = ((((2*self.R_braiders*(1-
inputs.axial_crimp)+2*permutation(self.R_axials_reverse,k)[i])*np.cos(self.n*0.5*(-
(self.t[i*self.discrete+j]+np.pi/self.n)+2*k*np.pi/self.n))+self.R_braiders+self.R_core)*np.sin(-
(self.t[i*self.discrete+j]+np.pi/self.n)+2*k*np.pi/self.n)))

              self.z_cc[k][i*self.discrete+j] = ((self.L*(self.t[i*self.discrete+j]+np.pi/self.n)/(2*np.pi)))

            else:

              self.x_cc[k][i*self.discrete+j] = (((self.R_braiders+self.R_core)*np.cos(-
(self.t[i*self.discrete+j]+np.pi/self.n)+2*k*np.pi/self.n)))

              self.y_cc[k][i*self.discrete+j] = (((self.R_braiders+self.R_core)*np.sin(-
(self.t[i*self.discrete+j]+np.pi/self.n)+2*k*np.pi/self.n)))

              self.z_cc[k][i*self.discrete+j] = ((self.L*(self.t[i*self.discrete+j]+np.pi/self.n)/(2*np.pi)))

    # end node

    for k in range(self.n): # number of braiders

      if self.clockwise_location[k] == 1:

        self.x_c[k][-1] = self.x_c[k][0]

        self.y_c[k][-1] = self.y_c[k][0]

        self.z_c[k][-1] = ((self.L*self.t_c[-1]/(2*np.pi)))
```

```
        if self.counterclockwise_location[k] == 1:
            self.x_cc[k][-1] = self.x_cc[k][0]
            self.y_cc[k][-1] = self.y_cc[k][0]
            self.z_cc[k][-1] = ((self.L*(self.t[-1]+np.pi/self.n)/(2*np.pi)))

    # axials
    self.ones = np.array([1]*len(self.t_cc))
    for i in range(self.number_a):
        if self.axial_location[i] == 1:

            self.x_a[i] =
(self.ones*(self.R_core+2*self.R_braiders+self.R_axials[i])*np.cos(2*np.pi*i/self.number_a))
            self.y_a[i] =
(self.ones*(self.R_core+2*self.R_braiders+self.R_axials[i])*np.sin(2*np.pi*i/self.number_a))
            self.z_a[i] = (self.L*self.t_cc/(2*np.pi))

    # shifting
    self.x_c_new = np.zeros(shape=(self.n,len(self.t)))
    self.y_c_new = np.zeros(shape=(self.n,len(self.t)))
    self.z_c_new = np.zeros(shape=(self.n,len(self.t)))

    self.x_cc_new = self.x_cc
    self.y_cc_new = self.y_cc
    self.z_cc_new = self.z_cc



    for j in range(self.number_c):
        if self.clockwise_location[j] == 1:
```

```
        for i in range(int(self.discrete/2),int(self.n*self.discrete+1+self.discrete/2),1):
            self.x_c_new[j][i-int(self.discrete/2)] = self.x_c[j][i]
            self.y_c_new[j][i-int(self.discrete/2)] = self.y_c[j][i]
            self.z_c_new[j][i-int(self.discrete/2)] = self.z_c[j][i]

# joint search
self.joint_xc = np.zeros(shape=(self.n,len(self.t)))
self.joint_yc = np.zeros(shape=(self.n,len(self.t)))
self.joint_xcc = np.zeros(shape=(self.n,len(self.t)))
self.joint_ycc = np.zeros(shape=(self.n,len(self.t)))
self.joint_xa = np.zeros(shape=(self.n,len(self.t)))
self.joint_ya = np.zeros(shape=(self.n,len(self.t)))

self.x_axial_center = np.zeros(shape=(self.n,1))
self.y_axial_center = np.zeros(shape=(self.n,1))

self.joint_xc_loc_withCC = np.ones(shape=(self.n,len(self.t)))*-1
self.joint_xc_loc_withAxial = np.ones(shape=(self.n,len(self.t)))*-1


self.joint_xcc_loc_withC = np.ones(shape=(self.n,len(self.t)))*-1
self.joint_xcc_loc_withAxial = np.ones(shape=(self.n,len(self.t)))*-1

self.joint_xa_loc = np.ones(shape=(self.n,len(self.t)))*-1



# search joint location between ccw,cw and axials
for i in range(self.number_c):
```

```
        if self.clockwise_location[i] == 1:
            for z in range(len(self.t)):
                for j in range(self.number_a):
                    if self.axial_location[j] == 1:
                        if (round((self.x_c_new[i][z]*self.x_a[j][z] + self.y_c_new[i][z]*self.y_a[j][z]),15) ==
round(((self.x_c_new[i][z]**2+self.y_c_new[i][z]**2)**0.5)*((self.x_a[j][z]**2+self.y_a[j][z]**2)**0.5),1
5)):
                            self.joint_xc[i][z] = (self.x_c_new[i][z])
                            self.joint_yc[i][z] = (self.y_c_new[i][z])
                            self.joint_xc_loc_withAxial[i][z] = z
                            self.joint_xa_loc[j][z] = z # append axial yarn joint location with C


                            # create crimp in axials depending on the position of braiders
                            if round((self.x_c_new[i][z]**2+self.y_c_new[i][z]**2)**0.5,15) >
round((self.x_a[j][z]**2+self.y_a[j][z]**2)**0.5,15):
                                self.x_a[j][z] =(((self.R_core+self.R_axials[j])-
np.sqrt(self.x_a[j][z]**2+self.y_a[j][z]**2))*inputs.axial_crimp +
                                        np.sqrt(self.x_a[j][z]**2+self.y_a[j][z]**2))*self.x_a[j][z] /
np.sqrt(self.x_a[j][z]**2+self.y_a[j][z]**2)
                                self.y_a[j][z] =(((self.R_core+self.R_axials[j])-
np.sqrt(self.x_a[j][z]**2+self.y_a[j][z]**2))*inputs.axial_crimp +
                                        np.sqrt(self.x_a[j][z]**2+self.y_a[j][z]**2))*self.y_a[j][z] /
np.sqrt(self.x_a[j][z]**2+self.y_a[j][z]**2)
                                self.x_axial_center[j] = self.x_a[j][z]
                                self.y_axial_center[j] = self.y_a[j][z]
    for i in range(self.number_cc):
        if self.counterclockwise_location[i] == 1:
            for z in range(len(self.t)):
                for j in range(self.number_a):
                    if self.axial_location[j] == 1:
```

```
                    if (round((self.x_cc_new[i][z]*self.x_a[j][z] + self.y_cc_new[i][z]*self.y_a[j][z]),15) ==
round(((self.x_cc_new[i][z]**2+self.y_cc_new[i][z]**2)**0.5)*((self.x_a[j][z]**2+self.y_a[j][z]**2)**0.5),
15)):
                        self.joint_xcc[i][z] = (self.x_cc_new[i][z])
                        self.joint_ycc[i][z] = (self.y_cc_new[i][z])
                        self.joint_xcc_loc_withAxial[i][z] = z
                        self.joint_xa_loc[j][z] = z # append axial yarn joint location with CC



                        # create crimp in axials depending on the position of braiders
                        if round((self.x_cc_new[i][z]**2+self.y_cc_new[i][z]**2)**0.5,15) >
round((self.x_a[j][z]**2+self.y_a[j][z]**2)**0.5,15):
                            self.x_a[j][z] =(((self.R_core+self.R_axials[j])-
np.sqrt(self.x_a[j][z]**2+self.y_a[j][z]**2))*inputs.axial_crimp +
                                    np.sqrt(self.x_a[j][z]**2+self.y_a[j][z]**2))*self.x_a[j][z] /
np.sqrt(self.x_a[j][z]**2+self.y_a[j][z]**2)
                            self.y_a[j][z] =(((self.R_core+self.R_axials[j])-
np.sqrt(self.x_a[j][z]**2+self.y_a[j][z]**2))*inputs.axial_crimp +
                                    np.sqrt(self.x_a[j][z]**2+self.y_a[j][z]**2))*self.y_a[j][z] /
np.sqrt(self.x_a[j][z]**2+self.y_a[j][z]**2)
                            self.x_axial_center[j] = self.x_a[j][z]
                            self.y_axial_center[j] = self.y_a[j][z]


    # joint nodes expanded
    self.joint_xc_loc_withAxial_new = np.ones(shape=(self.n,len(self.t)))*-1
    self.joint_xcc_loc_withAxial_new = np.ones(shape=(self.n,len(self.t)))*-1
    # reserve nodes around axial and braider joint, reserve whole section for horn hear


    for i in range(len(self.joint_xc_loc_withAxial)):
        for j in range(len(self.t)-int(self.discrete/2)):
            if self.joint_xc_loc_withAxial[i][j] == -1:
```

```
            pass
        else:
            self.joint_xc_loc_withAxial_new[i][j] = j
            for r in range(1,int(self.discrete/2)+1):
                if j-r>=0:
                    self.joint_xc_loc_withAxial_new[i][j-r] = j-r
                    self.joint_xc_loc_withAxial_new[i][j+r] = j+r
                else:
                    self.joint_xc_loc_withAxial_new[i][j-r] = len(self.t)+(j-r)

for i in range(len(self.joint_xcc_loc_withAxial)):
    for j in range(len(self.t)-int(self.discrete/2)):
        if self.joint_xcc_loc_withAxial[i][j] == -1:
            pass
        else:
            self.joint_xcc_loc_withAxial_new[i][j] = j
            for r in range(1,int(self.discrete/2)+1):
                if j-r>=0:
                    self.joint_xcc_loc_withAxial_new[i][j-r] = j-r
                    self.joint_xcc_loc_withAxial_new[i][j+r] = j+r
                else:
                    self.joint_xcc_loc_withAxial_new[i][j-r] = len(self.t)+(j-r)


# search joint loaction on cw from ccw
for i in range(self.number_c):
    if self.clockwise_location[i] == 1:
        for z in range(len(self.t)):
            for j in range(self.number_cc):
```

```
                if self.counterclockwise_location[j] == 1:

                    if (round((self.x_c_new[i][z]*self.x_cc_new[j][z] +
self.y_c_new[i][z]*self.y_cc_new[j][z]),15) ==
round(((self.x_c_new[i][z]**2+self.y_c_new[i][z]**2)**0.5)*((self.x_cc_new[j][z]**2+self.y_cc_new[j][z]
**2)**0.5),15)):

                        self.joint_xc[i][z] = (self.x_c_new[i][z])

                        self.joint_yc[i][z] = (self.y_c_new[i][z])

                        self.joint_xc_loc_withCC[i][z] = z

                        if ((round((self.x_c_new[i][z]**2+self.y_c_new[i][z]**2)**0.5,15) >
round((self.x_cc_new[j][z]**2+self.y_cc_new[j][z]**2)**0.5,15)) and

                            (not (z in self.joint_xc_loc_withAxial_new[i]))):



                            self.x_c_new[i][z] = (3*self.R_braiders+R_core)*self.x_c_new[i][z] /
np.sqrt(self.x_c_new[i][z]**2+self.y_c_new[i][z]**2)

                            self.y_c_new[i][z] = (3*self.R_braiders+R_core)*self.y_c_new[i][z] /
np.sqrt(self.x_c_new[i][z]**2+self.y_c_new[i][z]**2)




    # search joint loaction on ccw from cw

    for i in range(self.number_cc):

        if self.counterclockwise_location[i] == 1:

            for z in range(len(self.t)):

                for j in range(self.number_c):

                    if self.clockwise_location[j] == 1:

                        if (round((self.x_cc_new[i][z]*self.x_c_new[j][z] +
self.y_cc_new[i][z]*self.y_c_new[j][z]),15) ==
round(((self.x_cc_new[i][z]**2+self.y_cc_new[i][z]**2)**0.5)*((self.x_c_new[j][z]**2+self.y_c_new[j][z]
**2)**0.5),15)):

                            self.joint_xcc[i][z] = (self.x_cc_new[i][z])

                            self.joint_ycc[i][z] = (self.y_cc_new[i][z])

                            self.joint_xcc_loc_withC[i][z] = z
```

```
                    if ((round((self.x_cc_new[i][z]**2+self.y_cc_new[i][z]**2)**0.5,15) >
round((self.x_c_new[j][z]**2+self.y_c_new[j][z]**2)**0.5,15)) and

                        (not (z in self.joint_xcc_loc_withAxial_new[i]))):

                        self.x_cc_new[i][z] = (3*self.R_braiders+R_core)*self.x_cc_new[i][z] /
np.sqrt(self.x_cc_new[i][z]**2+self.y_cc_new[i][z]**2)

                        self.y_cc_new[i][z] = (3*self.R_braiders+R_core)*self.y_cc_new[i][z] /
np.sqrt(self.x_cc_new[i][z]**2+self.y_cc_new[i][z]**2)



    # apply compression, reserve the location of joint node, compress the rest close as much as possible
to the mandrel

    for i in range(self.number_c):

        if self.clockwise_location[i] == 1:

            for j in range(len(self.t)):

                if (j in self.joint_xc_loc_withCC[i]) or (j in self.joint_xc_loc_withAxial_new [i]):

                    pass

                else:

                    self.x_c_new[i][j] = self.x_c_new[i][j]*(self.R_braiders+self.R_core) /
((self.x_c_new[i][j]**2+self.y_c_new[i][j]**2)**0.5)

                    self.y_c_new[i][j] = self.y_c_new[i][j]*(self.R_braiders+self.R_core) /
((self.x_c_new[i][j]**2+self.y_c_new[i][j]**2)**0.5)

    for i in range(self.number_cc):

        if self.counterclockwise_location[i] == 1:

            for j in range(len(self.t)):

                if (j in self.joint_xcc_loc_withC[i]) or (j in self.joint_xcc_loc_withAxial_new[i]):

                    pass

                else:

                    self.x_cc_new[i][j] = self.x_cc_new[i][j]*(self.R_braiders+self.R_core) /
((self.x_cc_new[i][j]**2+self.y_cc_new[i][j]**2)**0.5)

                    self.y_cc_new[i][j] = self.y_cc_new[i][j]*(self.R_braiders+self.R_core) /
((self.x_cc_new[i][j]**2+self.y_cc_new[i][j]**2)**0.5)
```

```
        self.iteration = 0

        while self.iteration <= 2:

        # apply tension,find geodesic distance(first and last node excluded)

            for i in range(self.number_c):

                if self.clockwise_location[i] == 1:

                    for j in range(1,len(self.t)-1):

                        if (j in self.joint_xc_loc_withCC[i]) or (j in self.joint_xc_loc_withAxial[i]):

                            pass

                        else:

                            self.x_c_new[i][j] = tension(self.x_c_new[i][j-1],self.y_c_new[i][j-1],self.z_c_new[i][j-
1],self.x_c_new[i][j+1],self.y_c_new[i][j+1],self.z_c_new[i][j+1],self.x_c_new[i][j],self.y_c_new[i][j],self.z
_c_new[i][j])[0]

                            self.y_c_new[i][j] = tension(self.x_c_new[i][j-1],self.y_c_new[i][j-1],self.z_c_new[i][j-
1],self.x_c_new[i][j+1],self.y_c_new[i][j+1],self.z_c_new[i][j+1],self.x_c_new[i][j],self.y_c_new[i][j],self.z
_c_new[i][j])[1]

            for i in range(self.number_cc):

                if self.counterclockwise_location[i] == 1:

                    for j in range(1,len(self.t)-1):

                        if (j in self.joint_xcc_loc_withC[i]) or (j in self.joint_xcc_loc_withAxial[i]):

                            pass

                        else:

                            self.x_cc_new[i][j] = tension(self.x_cc_new[i][j-1],self.y_cc_new[i][j-1],self.z_cc_new[i][j-
1],self.x_cc_new[i][j+1],self.y_cc_new[i][j+1],self.z_cc_new[i][j+1],self.x_cc_new[i][j],self.y_cc_new[i][j],
self.z_cc_new[i][j])[0]

                            self.y_cc_new[i][j] = tension(self.x_cc_new[i][j-1],self.y_cc_new[i][j-1],self.z_cc_new[i][j-
1],self.x_cc_new[i][j+1],self.y_cc_new[i][j+1],self.z_cc_new[i][j+1],self.x_cc_new[i][j],self.y_cc_new[i][j],
self.z_cc_new[i][j])[1]

            # relax braider on axials

            # relax on cw

            for k in range(len(self.x_axial_center)):

                for i in range(self.number_c):
```

```
            if self.clockwise_location[i] == 1:
                for j in range(len(self.t)):
                    self.x_c_new[i][j] =
braider_on_axials(self.x_axial_center[k],self.y_axial_center[k],self.x_c_new[i][j],self.y_c_new[i][j],self.R_
axials[k]+self.R_braiders,self.R_core)[0]
                    self.y_c_new[i][j] =
braider_on_axials(self.x_axial_center[k],self.y_axial_center[k],self.x_c_new[i][j],self.y_c_new[i][j],self.R_
axials[k]+self.R_braiders,self.R_core)[1]
        # relax on ccw
        for k in range(len(self.x_axial_center)):
            for i in range(self.number_cc):
                if self.counterclockwise_location[i] == 1:
                    for j in range(len(self.t)):
                        self.x_cc_new[i][j] =
braider_on_axials(self.x_axial_center[k],self.y_axial_center[k],self.x_cc_new[i][j],self.y_cc_new[i][j],self.
R_axials[k]+self.R_braiders,self.R_core)[0]
                        self.y_cc_new[i][j] =
braider_on_axials(self.x_axial_center[k],self.y_axial_center[k],self.x_cc_new[i][j],self.y_cc_new[i][j],self.
R_axials[k]+self.R_braiders,self.R_core)[1]


        self.iteration += 1
    self.iteration_axials = 0
    while self.iteration_axials <= 100:
        for i in range(self.number_a):
            if self.axial_location[i] == 1:
                for j in range(0,len(self.t)-1):
                    if j in self.joint_xa_loc[i]:
                        pass
                    else:
                        self.x_a[i][j] = tension_axials(self.x_a[i][j-1],self.y_a[i][j-1],self.z_a[i][j-
1],self.x_a[i][j+1],self.y_a[i][j+1],self.z_a[i][j+1],self.x_a[i][j],self.y_a[i][j],self.z_a[i][j])[0]
```

```
                    self.y_a[i][j] = tension_axials(self.x_a[i][j-1],self.y_a[i][j-1],self.z_a[i][j-
1],self.x_a[i][j+1],self.y_a[i][j+1],self.z_a[i][j+1],self.x_a[i][j],self.y_a[i][j],self.z_a[i][j])[1]


        for i in range(self.number_a):
            if self.axial_location[i] == 1:
                if (len(self.t)-1) in self.joint_xa_loc[i]:
                    pass
                else:
                    self.x_a[i][-1] = tension_axials(self.x_a[i][-2],self.y_a[i][-2],self.z_a[i][-
2],self.x_a[i][0],self.y_a[i][0],self.z_a[i][0],self.x_a[i][-1],self.y_a[i][-1],self.z_a[i][-1])[0]
                    self.y_a[i][-1] = tension_axials(self.x_a[i][-2],self.y_a[i][-2],self.z_a[i][-
2],self.x_a[i][0],self.y_a[i][0],self.z_a[i][0],self.x_a[i][-1],self.y_a[i][-1],self.z_a[i][-1])[1]


        self.iteration_axials += 1




class inputs():
    pass




def moment_inertia_composite(N,D,resin_thickness,El_fiber,E_matrix):
    n_layer = 0.5 + np.sqrt(9-12*(1-N)) / 6.0
    n_layer = int(n_layer)
    r = float(D/2)


    A = np.pi*r**2
```

```
    I = np.pi*r**4/4.0
    I_yy_fiber = (2*n_layer - 1)*I
    I_yy_fiber_x = 0.0

    # resin_thickness = np.sqrt(A*N/vf) / (np.pi*(2*n_layer-1)) - r
    for i in range(2,n_layer):
        I_yy_fiber_x += (2*n_layer -i)*(I + A*(3.0/4.0)*((i-1)*(D+2*resin_thickness))**2)
    I_yy_fiber_f = I_yy_fiber + 2*I_yy_fiber_x
    print (I_yy_fiber + 2*I_yy_fiber_x)
    radius_total = (2.0*(r+resin_thickness)*n_layer-1.0*(r+resin_thickness))
    I_yy_total = (np.pi/4.0)*radius_total**4
    I_yy_matrix = I_yy_total - (I_yy_fiber + 2.0*I_yy_fiber_x)



    A_total = radius_total**2*np.pi
    vf = A*N / A_total
    E_flexiral = (El_fiber*I_yy_fiber_f + E_matrix*I_yy_matrix) / I_yy_total
    return [E_flexiral,radius_total]

# number of horn gears
inputs.n = 8
# full loaded
inputs.cc = [1,0,1,0,1,0,1,0]
inputs.c =  [1,0,1,0,1,0,1,0]
inputs.a =  [1,0,1,0,1,0,1,0]
```

```
inputs.theta = 45


inputs.axial_crimp = 0.99 # axial yarn crimp added from 0 (no crimp) - 0.99 (100% crimp, cannot equal to 1)

R_a = moment_inertia_composite(3000,7.1e-6,0,220e9,2.89e9)[1]

R_axials =[0.05e-3,0,0.05e-3,0,0.05e-3,0,0.05e-3,0]

R_core =  0.4e-3

R_braiders = 0.05e-3


target = Coordinates(inputs.theta,inputs.n,inputs.cc,inputs.c,inputs.a,R_axials,R_core,R_braiders)


scene = display(autocenter=True)


for i in range(len(inputs.cc)):
   if inputs.cc[i] == 1:
      straight = [(0,0,target.z_cc_new[i][0]),(0,0,target.z_cc_new[i][-1])]
      break
# shape_core = shapes.circle(pos=(0,0),radius=R_core)
# extrusion(pos=straight, shape=shape_core,color=color.blue)


shape_core = shapes.circle(pos=(0,0.2e-3),radius=0.2e-3*np.cos(np.pi/6))

extrusion(pos=straight, shape=shape_core,color=color.yellow)


shape_core = shapes.circle(pos=(0.2e-3*np.cos(np.pi/6),-0.2e-3*np.sin(np.pi/6)),radius=0.2e-3*np.cos(np.pi/6))

extrusion(pos=straight, shape=shape_core,color=color.yellow)


shape_core = shapes.circle(pos=(-0.2e-3*np.cos(np.pi/6),-0.2e-3*np.sin(np.pi/6)),radius=0.2e-3*np.cos(np.pi/6))

extrusion(pos=straight, shape=shape_core,color=color.yellow)
```

```
for i in range(len(inputs.a)):
    if inputs.a[i] == 1:
        circ = shapes.circle(pos=(0,0),radius=R_axials[i])
        curve = []
        for j in range(len(target.t)):
            curve.append((target.x_a[i][j],target.y_a[i][j],target.z_a[i][j]))
        extrusion(pos=curve, shape=circ,color=color.yellow)

for i in range(len(inputs.cc)):
    if inputs.cc[i] == 1:
        circ = shapes.circle(pos=(0,0),radius=R_braiders)
        curve = []
        for j in range(len(target.t)):
            curve.append((target.x_cc_new[i][j],target.y_cc_new[i][j],target.z_cc_new[i][j]))
        extrusion(pos=curve, shape=circ,color=color.red)
for i in range(len(inputs.c)):
    if inputs.c[i] == 1:
        circ = shapes.circle(pos=(0,0),radius=R_braiders)
        curve = []
        for j in range(len(target.t)):
            curve.append((target.x_c_new[i][j],target.y_c_new[i][j],target.z_c_new[i][j]))
        extrusion(pos=curve, shape=circ,color=color.green)

# second moment of inertia
def inertia(x,y,r):
    Iyy = (np.pi/4)*r**4 + np.pi*r**2*y**2
    Izz = (np.pi/2)*r**4 + np.pi*r**2*(x**2+y**2)
    return [Iyy,Izz]
```

```
Iyy_ = inertia(0,0,R_core)[0]
Izz_ = inertia(0,0,R_core)[1]
for i in range(len(inputs.c)):
    if inputs.c[i] == 1:
        Iyy_ += inertia(target.x_c_new[i][0],target.y_c_new[i][0],R_braiders)[0]
        Izz_ += inertia(target.x_c_new[i][0],target.y_c_new[i][0],R_braiders)[1]
for i in range(len(inputs.cc)):
    if inputs.cc[i] == 1:
        Iyy_ += inertia(target.x_cc_new[i][0],target.y_cc_new[i][0],R_braiders)[0]
        Izz_ += inertia(target.x_cc_new[i][0],target.y_cc_new[i][0],R_braiders)[1]
for i in range(len(inputs.a)):
    if inputs.a[i] == 1:
        x_average = sum(target.x_a[i]) / len(target.x_a[i])
        y_average = sum(target.y_a[i]) / len(target.y_a[i])
        Iyy_ += inertia(x_average,y_average,R_axials[i])[0]
        Izz_ += inertia(x_average,y_average,R_axials[i])[1]
print ("Iyy",Iyy_) # global moment of inertia
print ("Izz",Izz_) # global moment of inertia
```

Diameter and flexural modulus of the core

```
import numpy as np
def moment_inertia_composite(N,D,resin_thickness):
    n_layer = 0.5 + np.sqrt(9-12*(1-N)) / 6.0
    n_layer = int(n_layer)
    r = float(D/2)

    A = np.pi*r**2
```

```
I = np.pi*r**4/4.0
I_yy_fiber = (2*n_layer - 1)*I
I_yy_fiber_x = 0.0

J = np.pi*r**4/2.0

# resin_thickness = np.sqrt(A*N/vf) / (np.pi*(2*n_layer-1)) - r
for i in range(2,n_layer):
    I_yy_fiber_x += (2*n_layer -i)*(I + A*(3.0/4.0)*((i-1)*(D+2*resin_thickness))**2)
J_fiber = J
for j in range(2,n_layer):
    J_fiber += (6*(j-1))*(J + A*(((j-1)*(2*r)+(np.sqrt(3)/2)*(i-1)*(2*r))/2)**2)
radius_total = (2.0*(r+resin_thickness)*n_layer-1.0*(r+resin_thickness))
J_total = (np.pi/2.0)*radius_total**4
J_matrix = J_total - J_fiber
GJ_core = J_fiber*14e9 + J_matrix*1.5e9
G_torque = GJ_core / J_total

print ('G_torque', G_torque)
print ('GJ_core', GJ_core)
I_yy_fiber_f = I_yy_fiber + 2*I_yy_fiber_x
print (I_yy_fiber + 2*I_yy_fiber_x)

I_yy_total = (np.pi/4.0)*radius_total**4
I_yy_matrix = I_yy_total - (I_yy_fiber + 2.0*I_yy_fiber_x)



A_total = radius_total**2*np.pi
```

```
   vf = A*N / A_total
   print ("total",I_yy_total)
   print ("fiber",I_yy_fiber + 2*I_yy_fiber_x )
   print ("area",A_total)
   print ("diameter",2*radius_total)
   print ("E_flexural", (245e9*I_yy_fiber_f + 2.83e9*I_yy_matrix) / I_yy_total)
   print ("Vf", (vf))
```

An example of the shell program in Matlab for generating the finite element code

```
n = length(INFO.warp.X);
fid = fopen('Integrated code with eigenbuckling', 'w');
fprintf(fid,'/prep7\n');

% output keypoints
for i = 1:1:16
   for j = 1:1:n
      if isnan(INFO.warp.X(j,i)) == 0
         fprintf(fid,'K,,%.4f,%.4f,%.4f\n',INFO.warp.X(j,i),INFO.warp.Y(j,i),INFO.warp.Z(j,i));
      end
   end
end
for i = 1:1:16
   for j = 1:1:n
      if isnan(INFO.weft.X(j,i)) == 0
         fprintf(fid,'K,,%.4f,%.4f,%.4f\n',INFO.weft.X(j,i),INFO.weft.Y(j,i),INFO.weft.Z(j,i));
      end
   end
end
```

```
for i = 1:1:16
   for j = 1:1:n
      if isnan(INFO.axial.X(j,i)) == 0
         fprintf(fid,'K,,%.4f,%.4f,%.4f\n',INFO.axial.X(j,i),INFO.axial.Y(j,i),INFO.axial.Z(j,i));
      end
   end
end



number_of_warp = 0;
number_of_weft = 0;
number_of_axial = 0;

for i = 1:1:16
   if isnan(INFO.warp.X(1,i)) == 0
      number_of_warp = number_of_warp+1;
   end

   if isnan(INFO.weft.X(1,i)) == 0
      number_of_weft = number_of_weft+1;
   end

   if isnan(INFO.axial.X(1,i)) == 0
      number_of_axial = number_of_axial+1;
   end
end

number_of_yarn = number_of_warp+number_of_weft+number_of_axial;
```

```
% define line element for yarn
fprintf(fid,'*do,j,1,%f,1\n', number_of_yarn);
fprintf(fid,'*do,i,1,%f,1\n', n-1);
fprintf(fid,'L,i+%f*(j-1),i+%f*(j-1)+1\n', n,n);
fprintf(fid,'*enddo\n');
fprintf(fid,'*enddo\n');

GenCoordinate();


% define line element for the joint
D1 = 2.1e-3^2;
D2 = 2.1e-3^2;


% joints betw helicals and axials
number_of_joint = 0;
for h = number_of_warp+number_of_weft+1:1:number_of_yarn
   for k = 1:1:n
      for i=1:1:(number_of_warp+number_of_weft)*n
         if (A(i,1)-A((h-1)*n+k,1))^2+(A(i,2)-A((h-1)*n+k,2))^2+(A(i,3)-A((h-1)*n+k,3))^2 <= D1
            fprintf(fid,'L, %f, %f\n', i, (h-1)*n+k);
            number_of_joint = number_of_joint+1;
         end
      end
   end
end
```

```
% joints betw helicals and helicals
for h = number_of_warp+1:1:number_of_warp+number_of_weft
   for k = 1:1:n
      for i = 1:1:number_of_warp
         for j = 1:1:n
            if (A(j+n*(i-1),1)-A(k+n*(h-1),1))^2+(A(j+n*(i-1),2)-A(k+n*(h-1),2))^2+(A(j+n*(i-1),3)-A(k+n*(h-
1),3))^2 <= D2
               fprintf(fid,'L, %f, %f\n', j+n*(i-1), (h-1)*n+k);
               number_of_joint = number_of_joint+1;
            end
         end
      end
   end
end




fprintf(fid,'et,1,beam188\n');
fprintf(fid,'MPTEMP,,,,,,,,\n');
fprintf(fid,'MPTEMP,1,0\n');
fprintf(fid,'mpdata,ex,1,,160e9\n');
fprintf(fid,'MPDATA,PRXY,1,,0.2\n');
fprintf(fid,'SECTYPE,   1, BEAM, CSOLID, yarn, 0\n');
fprintf(fid,'SECOFFSET, CENT\n');
fprintf(fid,'SECDATA,0.00095,5,5,0,0,0,0,0,0,0,0,0\n');

fprintf(fid,'et,2,beam188\n');
fprintf(fid,'MPTEMP,,,,,,,,\n');
fprintf(fid,'MPTEMP,1,0\n');
```

```
fprintf(fid,'mpdata,ex,2,,6e9\n');
fprintf(fid,'MPDATA,PRXY,2,,0.3\n');

fprintf(fid,'SECTYPE,   2, BEAM, CSOLID, joint, 0\n');
fprintf(fid,'SECOFFSET, CENT\n');
fprintf(fid,'SECDATA,0.00095,5,5,0,0,0,0,0,0,0,0,0\n');



fprintf(fid,'TYPE,   1\n');
fprintf(fid,'MAT,      1\n');
fprintf(fid,'REAL, \n');
fprintf(fid,'ESYS,      0\n');
fprintf(fid,'SECNUM,   1\n');

fprintf(fid,'lsel,s, , ,1,%f,1,0\n', (n-1)*number_of_yarn);
fprintf(fid,'lesize,all, , ,1, , , , ,0\n');
fprintf(fid,'lmesh,all\n');

fprintf(fid,'TYPE,   2\n');
fprintf(fid,'MAT,      2\n');
fprintf(fid,'REAL, \n');
fprintf(fid,'ESYS,      0\n');
fprintf(fid,'SECNUM,   2\n');

fprintf(fid,'lsel,s, , ,%f,%f,1,0\n', (n-1)*number_of_yarn+1,(n-1)*number_of_yarn+number_of_joint);
fprintf(fid,'lesize,all, , ,1, , , , ,0\n');
fprintf(fid,'lmesh,all\n');
```

```
fprintf(fid,'allsel\n');


fprintf(fid,'et,3,184\n');
fprintf(fid,'KEYOPT,3,1,1\n');
fprintf(fid,'KEYOPT,3,2,0\n');

fprintf(fid,'n,,0,0,0\n');
fprintf(fid,'TYPE,   3\n');
fprintf(fid,'*do,i,1,%f,1\n',number_of_yarn);
fprintf(fid,'e,%f,%f*(i-1)+1\n',n*number_of_yarn+1,n);
fprintf(fid,'*enddo\n');

fprintf(fid,'F,%f,MZ,1\n',n*number_of_yarn+1);


fprintf(fid,'*do,i,1,%f,1\n', number_of_yarn);
fprintf(fid,'D,%f*(i),ALL,0\n',n);

fprintf(fid,'*enddo\n');

fprintf(fid,'pstres,on\n');
fprintf(fid,'FINISH\n');
fprintf(fid,'/SOL\n');

fprintf(fid,'SOLVE\n');

fprintf(fid,'FINISH\n');
fprintf(fid,'/SOLUTION\n');
```

```
fprintf(fid,'ANTYPE,1\n');

fprintf(fid,'BUCOPT,SUBSP,1,0,0,CENTER\n');
fprintf(fid,'MXPAND,1,0,0,0,0.001\n');

fprintf(fid,'SOLVE\n');

fclose(fid);
```

An example of a finite element code in APDL for eigenvalue buckling analysis

```
/prep7
K,,0.0446,0.0000,0.0000
K,,0.0420,-0.0084,0.0082
K,,0.0394,-0.0163,0.0164
K,,0.0356,-0.0238,0.0246
K,,0.0315,-0.0315,0.0328
K,,0.0238,-0.0356,0.0410
K,,0.0163,-0.0394,0.0492
K,,0.0084,-0.0420,0.0574
K,,-0.0000,-0.0446,0.0656
K,,-0.0084,-0.0420,0.0738
K,,-0.0163,-0.0394,0.0820
K,,-0.0238,-0.0356,0.0902
K,,-0.0315,-0.0315,0.0984
K,,-0.0356,-0.0238,0.1066
K,,-0.0394,-0.0163,0.1148
K,,-0.0420,-0.0084,0.1230
```

K,,-0.0446,0.0000,0.1312

K,,-0.0420,0.0084,0.1394

K,,-0.0394,0.0163,0.1476

K,,-0.0356,0.0238,0.1558

K,,-0.0315,0.0315,0.1640

K,,-0.0238,0.0356,0.1721

K,,-0.0163,0.0394,0.1803

K,,-0.0084,0.0420,0.1885

K,,0.0000,0.0446,0.1967

K,,0.0084,0.0420,0.2049

K,,0.0163,0.0394,0.2131

K,,0.0238,0.0356,0.2213

K,,0.0315,0.0315,0.2295

K,,0.0356,0.0238,0.2377

K,,0.0394,0.0163,0.2459

K,,0.0419,0.0083,0.2541

K,,0.0427,0.0000,0.2623

K,,0.0000,0.0446,0.0000

K,,0.0084,0.0420,0.0082

K,,0.0163,0.0394,0.0164

K,,0.0238,0.0356,0.0246

K,,0.0315,0.0315,0.0328

K,,0.0356,0.0238,0.0410

K,,0.0394,0.0163,0.0492

K,,0.0420,0.0084,0.0574

K,,0.0446,0.0000,0.0656

K,,0.0420,-0.0084,0.0738

K,,0.0394,-0.0163,0.0820

K,,0.0356,-0.0238,0.0902

K,,0.0315,-0.0315,0.0984

K,,0.0238,-0.0356,0.1066

K,,0.0163,-0.0394,0.1148

K,,0.0084,-0.0420,0.1230

K,,-0.0000,-0.0446,0.1312

K,,-0.0084,-0.0420,0.1394

K,,-0.0163,-0.0394,0.1476

K,,-0.0238,-0.0356,0.1558

K,,-0.0315,-0.0315,0.1640

K,,-0.0356,-0.0238,0.1721

K,,-0.0394,-0.0163,0.1803

K,,-0.0420,-0.0084,0.1885

K,,-0.0446,0.0000,0.1967

K,,-0.0420,0.0084,0.2049

K,,-0.0394,0.0163,0.2131

K,,-0.0356,0.0238,0.2213

K,,-0.0315,0.0315,0.2295

K,,-0.0238,0.0356,0.2377

K,,-0.0163,0.0394,0.2459

K,,-0.0083,0.0419,0.2541

K,,-0.0000,0.0427,0.2623

K,,-0.0446,0.0000,0.0000

K,,-0.0420,0.0084,0.0082

K,,-0.0394,0.0163,0.0164

K,,-0.0356,0.0238,0.0246

K,,-0.0315,0.0315,0.0328

K,,-0.0238,0.0356,0.0410

K,,-0.0163,0.0394,0.0492

K,,-0.0084,0.0420,0.0574

K,,0.0000,0.0446,0.0656

K,,0.0084,0.0420,0.0738

K,,0.0163,0.0394,0.0820

K,,0.0238,0.0356,0.0902

K,,0.0315,0.0315,0.0984

K,,0.0356,0.0238,0.1066

K,,0.0394,0.0163,0.1148

K,,0.0420,0.0084,0.1230

K,,0.0446,0.0000,0.1312

K,,0.0420,-0.0084,0.1394

K,,0.0394,-0.0163,0.1476

K,,0.0356,-0.0238,0.1558

K,,0.0315,-0.0315,0.1640

K,,0.0238,-0.0356,0.1721

K,,0.0163,-0.0394,0.1803

K,,0.0084,-0.0420,0.1885

K,,-0.0000,-0.0446,0.1967

K,,-0.0084,-0.0420,0.2049

K,,-0.0163,-0.0394,0.2131

K,,-0.0238,-0.0356,0.2213

K,,-0.0315,-0.0315,0.2295

K,,-0.0356,-0.0238,0.2377

K,,-0.0394,-0.0163,0.2459

K,,-0.0419,-0.0083,0.2541

K,,-0.0427,-0.0000,0.2623

K,,-0.0000,-0.0446,0.0000

K,,-0.0084,-0.0420,0.0082

K,,-0.0163,-0.0394,0.0164

K,,-0.0238,-0.0356,0.0246

K,,-0.0315,-0.0315,0.0328

K,,-0.0356,-0.0238,0.0410

K,,-0.0394,-0.0163,0.0492

K,,-0.0420,-0.0084,0.0574

K,,-0.0446,0.0000,0.0656

K,,-0.0420,0.0084,0.0738

K,,-0.0394,0.0163,0.0820

K,,-0.0356,0.0238,0.0902

K,,-0.0315,0.0315,0.0984

K,,-0.0238,0.0356,0.1066

K,,-0.0163,0.0394,0.1148

K,,-0.0084,0.0420,0.1230

K,,0.0000,0.0446,0.1312

K,,0.0084,0.0420,0.1394

K,,0.0163,0.0394,0.1476

K,,0.0238,0.0356,0.1558

K,,0.0315,0.0315,0.1640

K,,0.0356,0.0238,0.1721

K,,0.0394,0.0163,0.1803

K,,0.0420,0.0084,0.1885

K,,0.0446,0.0000,0.1967

K,,0.0420,-0.0084,0.2049

K,,0.0394,-0.0163,0.2131

K,,0.0356,-0.0238,0.2213

K,,0.0315,-0.0315,0.2295

K,,0.0238,-0.0356,0.2377

K,,0.0163,-0.0394,0.2459

K,,0.0083,-0.0419,0.2541

K,,0.0000,-0.0427,0.2623

K,,0.0427,0.0000,0.0000

K,,0.0420,0.0084,0.0082

K,,0.0412,0.0171,0.0164

K,,0.0356,0.0238,0.0246

K,,0.0302,0.0302,0.0328

K,,0.0237,0.0355,0.0410

K,,0.0163,0.0394,0.0492

K,,0.0083,0.0419,0.0574

K,,0.0000,0.0427,0.0656

K,,-0.0084,0.0420,0.0738

K,,-0.0171,0.0412,0.0820

K,,-0.0238,0.0356,0.0902

K,,-0.0302,0.0302,0.0984

K,,-0.0355,0.0237,0.1066

K,,-0.0394,0.0163,0.1148

K,,-0.0419,0.0083,0.1230

K,,-0.0427,0.0000,0.1312

K,,-0.0420,-0.0084,0.1394

K,,-0.0412,-0.0171,0.1476

K,,-0.0356,-0.0238,0.1558

K,,-0.0302,-0.0302,0.1640

K,,-0.0237,-0.0355,0.1721

K,,-0.0163,-0.0394,0.1803

K,,-0.0083,-0.0419,0.1885

K,,-0.0000,-0.0427,0.1967

K,,0.0084,-0.0420,0.2049

K,,0.0171,-0.0412,0.2131

K,,0.0238,-0.0356,0.2213

K,,0.0302,-0.0302,0.2295

K,,0.0355,-0.0237,0.2377

K,,0.0394,-0.0163,0.2459

K,,0.0419,-0.0083,0.2541

K,,0.0427,-0.0000,0.2623

K,,-0.0000,-0.0427,0.0000

K,,0.0084,-0.0420,0.0082

K,,0.0171,-0.0412,0.0164

K,,0.0238,-0.0356,0.0246

K,,0.0302,-0.0302,0.0328

K,,0.0355,-0.0237,0.0410

K,,0.0394,-0.0163,0.0492

K,,0.0419,-0.0083,0.0574

K,,0.0427,0.0000,0.0656

K,,0.0420,0.0084,0.0738

K,,0.0412,0.0171,0.0820

K,,0.0356,0.0238,0.0902

K,,0.0302,0.0302,0.0984

K,,0.0237,0.0355,0.1066

K,,0.0163,0.0394,0.1148

K,,0.0083,0.0419,0.1230

K,,0.0000,0.0427,0.1312

K,,-0.0084,0.0420,0.1394

K,,-0.0171,0.0412,0.1476

K,,-0.0238,0.0356,0.1558

K,,-0.0302,0.0302,0.1640

K,,-0.0355,0.0237,0.1721

K,,-0.0394,0.0163,0.1803

K,,-0.0419,0.0083,0.1885

K,,-0.0427,0.0000,0.1967

K,,-0.0420,-0.0084,0.2049

K,,-0.0412,-0.0171,0.2131

K,,-0.0356,-0.0238,0.2213

K,,-0.0302,-0.0302,0.2295

K,,-0.0237,-0.0355,0.2377

K,,-0.0163,-0.0394,0.2459

K,,-0.0083,-0.0419,0.2541

K,,-0.0000,-0.0427,0.2623

K,,-0.0427,0.0000,0.0000

K,,-0.0420,-0.0084,0.0082

K,,-0.0412,-0.0171,0.0164

K,,-0.0356,-0.0238,0.0246

K,,-0.0302,-0.0302,0.0328

K,,-0.0237,-0.0355,0.0410

K,,-0.0163,-0.0394,0.0492

K,,-0.0083,-0.0419,0.0574

K,,-0.0000,-0.0427,0.0656

K,,0.0084,-0.0420,0.0738

K,,0.0171,-0.0412,0.0820

K,,0.0238,-0.0356,0.0902

K,,0.0302,-0.0302,0.0984

K,,0.0355,-0.0237,0.1066

K,,0.0394,-0.0163,0.1148

K,,0.0419,-0.0083,0.1230

K,,0.0427,0.0000,0.1312

K,,0.0420,0.0084,0.1394

K,,0.0412,0.0171,0.1476

K,,0.0356,0.0238,0.1558

K,,0.0302,0.0302,0.1640

K,,0.0237,0.0355,0.1721

K,,0.0163,0.0394,0.1803

K,,0.0083,0.0419,0.1885

K,,0.0000,0.0427,0.1967

K,,-0.0084,0.0420,0.2049

K,,-0.0171,0.0412,0.2131

K,,-0.0238,0.0356,0.2213

K,,-0.0302,0.0302,0.2295

K,,-0.0355,0.0237,0.2377

K,,-0.0394,0.0163,0.2459

K,,-0.0419,0.0083,0.2541

K,,-0.0427,0.0000,0.2623

K,,0.0000,0.0427,0.0000

K,,-0.0084,0.0420,0.0082

K,,-0.0171,0.0412,0.0164

K,,-0.0238,0.0356,0.0246

K,,-0.0302,0.0302,0.0328

K,,-0.0355,0.0237,0.0410

K,,-0.0394,0.0163,0.0492

K,,-0.0419,0.0083,0.0574

K,,-0.0427,0.0000,0.0656

K,,-0.0420,-0.0084,0.0738

K,,-0.0412,-0.0171,0.0820

K,,-0.0356,-0.0238,0.0902

K,,-0.0302,-0.0302,0.0984

K,,-0.0237,-0.0355,0.1066

K,,-0.0163,-0.0394,0.1148

K,,-0.0083,-0.0419,0.1230

K,,-0.0000,-0.0427,0.1312

K,,0.0084,-0.0420,0.1394

K,,0.0171,-0.0412,0.1476

K,,0.0238,-0.0356,0.1558

K,,0.0302,-0.0302,0.1640

K,,0.0355,-0.0237,0.1721

K,,0.0394,-0.0163,0.1803

K,,0.0419,-0.0083,0.1885

K,,0.0427,0.0000,0.1967

K,,0.0420,0.0084,0.2049

K,,0.0412,0.0171,0.2131

K,,0.0356,0.0238,0.2213

K,,0.0302,0.0302,0.2295

K,,0.0237,0.0355,0.2377

K,,0.0163,0.0394,0.2459

K,,0.0083,0.0419,0.2541

K,,0.0000,0.0427,0.2623

K,,0.0394,0.0163,0.0000

K,,0.0394,0.0163,0.0082

K,,0.0394,0.0163,0.0164

K,,0.0399,0.0165,0.0246

K,,0.0403,0.0167,0.0328

K,,0.0408,0.0169,0.0410

K,,0.0412,0.0171,0.0492

K,,0.0408,0.0169,0.0574

K,,0.0403,0.0167,0.0656

K,,0.0399,0.0165,0.0738

K,,0.0394,0.0163,0.0820

K,,0.0399,0.0165,0.0902

K,,0.0403,0.0167,0.0984

K,,0.0408,0.0169,0.1066

K,,0.0412,0.0171,0.1148

K,,0.0408,0.0169,0.1230

K,,0.0403,0.0167,0.1312

K,,0.0399,0.0165,0.1394

K,,0.0394,0.0163,0.1476

K,,0.0399,0.0165,0.1558

K,,0.0403,0.0167,0.1640

K,,0.0408,0.0169,0.1721

K,,0.0412,0.0171,0.1803

K,,0.0408,0.0169,0.1885

K,,0.0403,0.0167,0.1967

K,,0.0399,0.0165,0.2049

K,,0.0394,0.0163,0.2131

K,,0.0399,0.0165,0.2213

K,,0.0403,0.0167,0.2295

K,,0.0408,0.0169,0.2377

K,,0.0412,0.0171,0.2459

K,,0.0403,0.0167,0.2541

K,,0.0403,0.0167,0.2623

K,,-0.0163,0.0394,0.0000

K,,-0.0163,0.0394,0.0082

K,,-0.0163,0.0394,0.0164

K,,-0.0165,0.0399,0.0246

K,,-0.0167,0.0403,0.0328

K,,-0.0169,0.0408,0.0410

K,,-0.0171,0.0412,0.0492

K,,-0.0169,0.0408,0.0574

K,,-0.0167,0.0403,0.0656

K,,-0.0165,0.0399,0.0738

K,,-0.0163,0.0394,0.0820

K,,-0.0165,0.0399,0.0902

K,,-0.0167,0.0403,0.0984

K,,-0.0169,0.0408,0.1066

K,,-0.0171,0.0412,0.1148

K,,-0.0169,0.0408,0.1230

K,,-0.0167,0.0403,0.1312

K,,-0.0165,0.0399,0.1394

K,,-0.0163,0.0394,0.1476

K,,-0.0165,0.0399,0.1558

K,,-0.0167,0.0403,0.1640

K,,-0.0169,0.0408,0.1721

K,,-0.0171,0.0412,0.1803

K,,-0.0169,0.0408,0.1885

K,,-0.0167,0.0403,0.1967

K,,-0.0165,0.0399,0.2049

K,,-0.0163,0.0394,0.2131

K,,-0.0165,0.0399,0.2213

K,,-0.0167,0.0403,0.2295

K,,-0.0169,0.0408,0.2377

K,,-0.0171,0.0412,0.2459

K,,-0.0167,0.0403,0.2541

K,,-0.0167,0.0403,0.2623

K,,-0.0394,-0.0163,0.0000

K,,-0.0394,-0.0163,0.0082

K,,-0.0394,-0.0163,0.0164

K,,-0.0399,-0.0165,0.0246

K,,-0.0403,-0.0167,0.0328

K,,-0.0408,-0.0169,0.0410

K,,-0.0412,-0.0171,0.0492

K,,-0.0408,-0.0169,0.0574

K,,-0.0403,-0.0167,0.0656

K,,-0.0399,-0.0165,0.0738

K,,-0.0394,-0.0163,0.0820

K,,-0.0399,-0.0165,0.0902

K,,-0.0403,-0.0167,0.0984

K,,-0.0408,-0.0169,0.1066

K,,-0.0412,-0.0171,0.1148

K,,-0.0408,-0.0169,0.1230

K,,-0.0403,-0.0167,0.1312

K,,-0.0399,-0.0165,0.1394

K,,-0.0394,-0.0163,0.1476

K,,-0.0399,-0.0165,0.1558

K,,-0.0403,-0.0167,0.1640

K,,-0.0408,-0.0169,0.1721

K,,-0.0412,-0.0171,0.1803

K,,-0.0408,-0.0169,0.1885

K,,-0.0403,-0.0167,0.1967

K,,-0.0399,-0.0165,0.2049

K,,-0.0394,-0.0163,0.2131

K,,-0.0399,-0.0165,0.2213

K,,-0.0403,-0.0167,0.2295

K,,-0.0408,-0.0169,0.2377

K,,-0.0412,-0.0171,0.2459

K,,-0.0403,-0.0167,0.2541

K,,-0.0403,-0.0167,0.2623

K,,0.0163,-0.0394,0.0000

K,,0.0163,-0.0394,0.0082

K,,0.0163,-0.0394,0.0164

K,,0.0165,-0.0399,0.0246

K,,0.0167,-0.0403,0.0328

K,,0.0169,-0.0408,0.0410

K,,0.0171,-0.0412,0.0492

K,,0.0169,-0.0408,0.0574

K,,0.0167,-0.0403,0.0656

K,,0.0165,-0.0399,0.0738

K,,0.0163,-0.0394,0.0820

K,,0.0165,-0.0399,0.0902

K,,0.0167,-0.0403,0.0984

K,,0.0169,-0.0408,0.1066

K,,0.0171,-0.0412,0.1148

K,,0.0169,-0.0408,0.1230

K,,0.0167,-0.0403,0.1312

K,,0.0165,-0.0399,0.1394

K,,0.0163,-0.0394,0.1476

K,,0.0165,-0.0399,0.1558

K,,0.0167,-0.0403,0.1640

K,,0.0169,-0.0408,0.1721

K,,0.0171,-0.0412,0.1803

K,,0.0169,-0.0408,0.1885

K,,0.0167,-0.0403,0.1967

K,,0.0165,-0.0399,0.2049

K,,0.0163,-0.0394,0.2131

K,,0.0165,-0.0399,0.2213

K,,0.0167,-0.0403,0.2295

K,,0.0169,-0.0408,0.2377

K,,0.0171,-0.0412,0.2459

K,,0.0167,-0.0403,0.2541

K,,0.0167,-0.0403,0.2623

*do,j,1,12.000000,1

*do,i,1,32.000000,1

L,i+33.000000*(j-1),i+33.000000*(j-1)+1

*enddo

*enddo

L, 135.000000, 267.000000

L, 40.000000, 271.000000

L, 176.000000, 275.000000

L, 81.000000, 279.000000

L, 217.000000, 283.000000

L, 122.000000, 287.000000

L, 258.000000, 291.000000

L, 31.000000, 295.000000

L, 234.000000, 300.000000

L, 73.000000, 304.000000

L, 143.000000, 308.000000

L, 114.000000, 312.000000

L, 184.000000, 316.000000

L, 23.000000, 320.000000

L, 225.000000, 324.000000

L, 64.000000, 328.000000

L, 201.000000, 333.000000

L, 106.000000, 337.000000

L, 242.000000, 341.000000

L, 15.000000, 345.000000

L, 151.000000, 349.000000

L, 56.000000, 353.000000

L, 192.000000, 357.000000

L, 97.000000, 361.000000

L, 168.000000, 366.000000

L, 7.000000, 370.000000

L, 209.000000, 374.000000

L, 48.000000, 378.000000

L, 250.000000, 382.000000

L, 89.000000, 386.000000

L, 159.000000, 390.000000

L, 130.000000, 394.000000

L, 1.000000, 133.000000

L, 38.000000, 137.000000

L, 75.000000, 141.000000

L, 112.000000, 145.000000

L, 17.000000, 149.000000

L, 54.000000, 153.000000

L, 91.000000, 157.000000

L, 128.000000, 161.000000

L, 33.000000, 165.000000

L, 100.000000, 166.000000

L, 5.000000, 170.000000

L, 42.000000, 174.000000

L, 79.000000, 178.000000

L, 116.000000, 182.000000

L, 21.000000, 186.000000

L, 58.000000, 190.000000

L, 95.000000, 194.000000

L, 132.000000, 198.000000

L, 67.000000, 199.000000

L, 104.000000, 203.000000

L, 9.000000, 207.000000

L, 46.000000, 211.000000

L, 83.000000, 215.000000

L, 120.000000, 219.000000

L, 25.000000, 223.000000

L, 62.000000, 227.000000

L, 99.000000, 231.000000

L, 34.000000, 232.000000

L, 71.000000, 236.000000

L, 108.000000, 240.000000

L, 13.000000, 244.000000

L, 50.000000, 248.000000

L, 87.000000, 252.000000

L, 124.000000, 256.000000

L, 29.000000, 260.000000

L, 66.000000, 264.000000

et,1,beam188

MPTEMP,,,,,,,,

MPTEMP,1,0

mpdata,ex,1,,160e9

MPDATA,PRXY,1,,0.2

SECTYPE, 1, BEAM, CSOLID, yarn, 0

SECOFFSET, CENT

SECDATA,0.00095,5,5,0,0,0,0,0,0,0,0,0

et,2,beam188

MPTEMP,,,,,,,,

MPTEMP,1,0

```
mpdata,ex,2,,6e9
MPDATA,PRXY,2,,0.3
SECTYPE,   2, BEAM, CSOLID, joint, 0
SECOFFSET, CENT
SECDATA,0.00095,5,5,0,0,0,0,0,0,0,0,0
TYPE,   1
MAT,      1
REAL,
ESYS,      0
SECNUM,   1
lsel,s, , ,1,384.000000,1,0
lesize,all, , ,1, , , , ,0
lmesh,all
TYPE,   2
MAT,      2
REAL,
ESYS,      0
SECNUM,   2
lsel,s, , ,385.000000,452.000000,1,0
lesize,all, , ,1, , , , ,0
lmesh,all
allsel
et,3,184
KEYOPT,3,1,1
KEYOPT,3,2,0
n,,0,0,0
TYPE,   3
*do,i,1,12.000000,1
e,397.000000,33.000000*(i-1)+1
```

```
*enddo
F,397.000000,MZ,1
*do,i,1,12.000000,1
D,33.000000*(i),ALL,0
*enddo
pstres,on
FINISH
/SOL
SOLVE
FINISH
/SOLUTION
ANTYPE,1
BUCOPT,SUBSP,1,0,0,CENTER
MXPAND,1,0,0,0,0.001
SOLVE
```